UNIVERSITÀ DEGLI STUDI DI TRIESTE

Dipartimento di Ingegneria e Architettura

Dottorato di Ricerca in Ingegneria Industriale e dell’Informazione

Stefano Cleva

MACHINE COMPONENTS IMPEDANCE CALCULATION AND BUTTON TYPE BEAM POSITION MONITOR DESIGN FOR THE ELETTRA 2.0 SYNCHROTRON LIGHT SOURCE

Supervisor: Prof. M. Comisso
Dott. A.Passarelli

December 2025

Abstract

The Elettra 2.0 project represents a significant leap forward in synchrotron light sources, aiming to establish a fourth-generation machine characterized by ultra-low emittance and considerably higher brilliance compared to its predecessor Elettra. This upgrade is driven by the growing demand for photon beams with enhanced coherence, stability, and brightness, which are essential for state-of-the-art experiments in materials science, biology, chemistry, and nanotechnology. While Elettra 2.0 promises enhanced experimental capabilities, it also introduces inherent challenges, primarily stemming from more intense beam characteristics and significantly reduced vacuum chamber dimensions. These features, which are typical of fourth-generation light sources, impose stringent constraints on both accelerator components and beam diagnostics.

In particular, the reduction of the transverse beam emittance and the corresponding increase in beam density enhance collective electromagnetic effects, making the interaction between the beam and its surrounding environment a central aspect of the machine design. Components installed along the vacuum chamber, including diagnostic devices and mechanical junctions, can significantly influence beam dynamics through the generation of wakefields and the associated beam coupling impedance. If not properly controlled, these effects may lead to beam instabilities, increased energy spread, and degradation of beam quality. Consequently, a careful and quantitative evaluation of impedance contributions, together with the development of low-impedance diagnostic systems, is a fundamental requirement for the successful operation of Elettra 2.0.

Within this framework, this thesis addresses these challenges through two principal objectives: the design and prototypical realization of beam position monitors (BPMs) specifically optimized for Elettra 2.0, and a comprehensive evaluation of the beam coupling impedance of other critical machine components, such as two types of vacuum flanges. The methodology heavily relies on wakefield theory and impedance concepts, which provide the theoretical tools to describe the electromagnetic interaction between a relativistic charged particle beam and its environment. These analytical considerations are complemented by extensive use of 3D numerical simulations conducted using CST Particle Studio, allowing a detailed investigation of complex geometries and material properties.

For the Beam Position Monitors, the primary challenge addressed in this work is the reduced size of the rhomboidal vacuum chambers at the BPM installation site, resulting in an approximate 3:1 scale reduction factor compared to the original Elettra machine. This geometrical constraint leads to a beam induced surface current density approximately three times greater than in the existing storage ring. As a consequence, electromagnetic and thermal effects that were previously negligible become critically important and must be carefully taken into account during the design phase. The BPMs design optimization therefore focuses on a delicate balance: maximizing signal extraction from the beam via the four pick-ups, while simultaneously minimizing the parasitic effects introduced by the BPMs themselves, and ensuring a sufficiently strong output signal across all operating conditions.

Additional complexity arises from the wide range of operational scenarios foreseen for Elettra 2.0, including different filling patterns and bunch lengths. Variations in bunch length have a direct impact on both the spectral content of the BPM signals and the intensity of the wakefields generated by the diagnostic structure. Numerical analyses were performed to explore various pick-up designs based on different geometries and materials, investigating their influence on signal transfer impedance, wake potential, and energy loss. The simulations confirms the basic trend that shorter bunch lengths lead to higher wake potential, increased time duration of the wakefield, and greater energy loss within the BPM structure, while at the same time producing stronger output signals. Within this trade-off, the study identified conical pick-up shapes and low permittivity dielectric materials as promising solutions for optimizing the balance between transfer impedance and coupling impedance.

The prototyping phase further validated the feasibility and performance of four families of pick-ups manufactured andassembled on dedicated BPM bodies. These prototypes were subjected to an extensive test campaign, including radio-frequency measurements in laboratory and tests under real operational environments with circulating beam, confirming their performance and signal quality, and validating their suitability for integration into the Elettra 2.0 storage ring.

In parallel with the BPM activity, this thesis presents the beam coupling impedance evaluation of vacuum chamber connection flanges, which, due to their large number along the storage ring, can provide a non-negligible cumulative contribution to the total machine impedance. A detailed comparative numerical analysis was performed on two types of vacuum-sealing flanges, the SFL and SFP types, which were identified as potential critical components. The simulations, carried out using a relativistic Gaussian beam with a bunch length of 4 mm, quantitatively demonstrated that the SFP flange type exhibits a normalized longitudinal impedance approximately one hundred times lower than the SFL type. This stark difference led to the conclusion that SFL flanges are unsuitable for Elettra 2.0. The study further highlighted the critical importance of adhering to strict geometric tolerance limits for key parameters like the flange gap and gasket radius, , as even small deviations were shown to significantly affect the impedance. To address these issues, a custom radio-frequency gasket was developed and implemented. Thanks to this solution, beam-induced energy losses associated with both flange types were effectively suppressed, rendering their impedance contribution virtually negligible and fully compatible with the requirements of Elettra 2.0.

In conclusion, this thesis provides crucial design tools, methodologies, and validated solutions to effectively manage the complex electromagnetic challenges inherent in modern, high-performance particle accelerators such as Elettra 2.0. The results obtained contribute significantly to ensuring beam stability, minimizing impedance-related effects, and guaranteeing the reliable operation of essential diagnostic and mechanical components. More broadly, the work demonstrates the importance of an integrated approach combining theoretical analysis, advanced numerical simulations, and experimental validation for the successful development of fourth-generation synchrotron light sources.

Table of contents

List of figures

List of tables

In memory of my parents Zonta Norma and Cleva Virgilio.

Acknowledgements

I would like to express my deepest gratitude to all my colleagues at Elettra and at the other institutes (INFN, PSI, SOLEIL, DESY, ALBA) who, through their work and valuable suggestions, made it possible to develop the topics presented in this thesis.

Chapter 1

Introduction

1.1 The Elettra 2.0 project

The Elettra 2.0 project, funded by the Italian Government in 2019, represents a significant evolution for the Elettra Sincrotrone Trieste research center. The project aims to replace the current Elettra synchrotron, which has served users since 1994 as Europe's first third-generation soft X-ray light source. After 28 years of operation, Elettra will be dismantled and succeeded by Elettra 2.0, a fourth-generation storage ring designed as an ultra-low emittance light source. The new machine is based on a specific lattice called S6BA-E (enhanced symmetric six-bend achromat) , which maintains the same circumference of 259.2 meters as the current Elettra. This lattice features a 12-fold symmetry and is composed of 24 symmetric arcs, 12 long straight sections, and 12 short straight sections. Each arc consists of 3-unit cells of the TME (Theoretical Minimum Emittance) type. Thanks to this configuration, Elettra 2.0 will be able to generate electron beams with much lower emittance: the bare emittance will be 212 pm-rad (149 pm-rad at 2 GeV) with 1% coupling, representing a 50-fold reduction from the current machine. This significant improvement will enable the production of synchrotron light with considerably higher brilliance and coherence compared to the current third-generation source, thereby enhancing experimental capabilities. The brilliance is expected to increase by 2-3 orders of magnitude at 10 keV and about 36 times at 1 keV. The coherence level will also be drastically increased by a factor of 60 at 1 keV, with the goal of making Elettra 2.0 a fully transversely coherent source up to 0.5 keV-photon energy. The facility will also provide a very broad range of photon energies, from infrared to hard x-rays, and maximize the number of beamlines, exceeding two times the machine periodicity. The adoption of vertically deflecting cavities (crab cavities) will add further capabilities for generating extremely short pulses, which are crucial for time-resolved experiments. Elettra 2.0 will be able to produce picosecond-long light pulses at MHz repetition rates without interfering with standard multi-bunch operation. Specifically, for many beamlines, the pulse durations will be less than or equal to 3.5 ps FWHM at 10 keV. The low momentum compaction of the lattice (1.3e-4) allows for a naturally stable and short electron bunch, below 10 ps (FWHM) for a total current of 100 mA. The machine will primarily operate at 2.4 GeV, but it is designed to operate even at 2.0 GeV for a limited percentage of user time. The requested operating intensity will be increased to 400 mA. The current Elettra, in contrast, operates for about 75% of user-dedicated time at 2 GeV and 25% at 2.4 GeV, being the only facility to operate at two energies (both in top-up). The Elettra facility was shut down on July, 2^{nd}, 2025.

1.2 Elettra 2.0 main parameters

The main Elettra 2.0 storage ring parameters are reported in Table 1.1. The value marked with * corresponds to operation with all insertion devices included, while the value marked with ** reflects the bunch-lengthening effect induced by the insertion of the third-harmonic cavity.

Table 1.1

Parameter	**Value**	**Unit**
Energy	2.4	GeV
Circumference	259.2	m
Emittance	212	pm rad
Coupling	3	%
Harmonic number	432	–
Average current	400	mA
Energy loss per turn	450 (620*)	keV
RF peak voltage	2	MV
Main radiofrequency	499.654	MHz
Bunch length rms	6 (15**)	ps
Energy spread rms	0.09	%

Table 1.2 Main parameters of Elettra 2.0 storage ring.

1.3 Elettra 2.0 short component list

In order to better understand the complexity of the new machine, a list of components, new and existing, divided by type and expected features is reported below. The new components have, of course, been designed from scratch, whereas the existing ones will be reused in the new machine, as they are still suitable for operation in the upgraded system.

- Beam lines and insertion devices:
    - All long straight sections will be used for the installation of insertion devices, with the exception of the injection straight section;
    - Three new micro-spot beamlines are planned (µXRD, µXRF, and HB-SAXS) that the current machine cannot support. These will require the use of in-vacuum undulators (IVU) with a maximum aperture of 5 mm;
    - Some existing insertion devices, including the superconducting 3.5 T wiggler, will be reused;
    - Five short straight sections will be equipped with two short wigglers and three short undulators;
    - For hard X-ray imaging and absorption X-ray fluorescence applications, three super-bends (SB) with a peak field of 6 T will be installed;

  With all insertion devices and SBs included, the emittance at 2.4 GeV will be 214 pm-rad. The energy loss due to radiation will be 620 keV, which corresponds to 248 kW of power lost to radiation at 400 mA. The accelerating cavities are in charge to refill the energy lost by the beam.

- Magnetic lattice (can vary depending on the specific achromat)
    - 3 dipoles (one at 0.8 T with vertical field gradient, and two with combined transverse and longitudinal gradients);
    - 8 quadrupoles (four of which are shifted to provide a reverse-bend angle of -0.4 degrees);
    - 10 combined sextupoles (some with correctors and skew quadrupole coils), along with 2 combined multipoles (octupoles with correctors);
- Diagnostics
    - 168 rhomboidal Beam Position Monitor(BPM);
    - New Parametric Current Transformer;
- Passive super conducting harmonic cavity (Super 3HC)

  - Super 3HC is in charge of increasing the natural bunch length to cope longitudinal beam instability and lifetime deterioration;
  - The bunch lengthen will reduce the emittance increase induced by intra-beam scattering from 30% to 11% and increase the Touschek lifetime from 6 hours to 18 hours;

- Vacuum pipe:
  - The vacuum chamber is primarily rhomboidal with 27 x 17 mm internal dimensions, made mainly of copper, with some parts in aluminum and stainless steel. Relative to the Elettra vacuum chamber size of 81 × 56 mm, the Elettra 2.0 dimensions are scaled down by a factor of 3. Most parts will be covered with a 500 nm NEG coating;
  - Several ancillary components will be used, such as flanges, tapers, bellows, ...

- Radio Frequency (RF) system
  - The four Elettra 500 MHz RF cavities currently in operation will be reused;
  - Each cavity will be powered by a 130 kW solid-state amplifier (SSA);
  - The full RF system foreseen foe Elettra 2.0 has been already tested in Elettra;

- Injection system
  - The injection system will utilize two kickers, two septa, and one anti-septum, employing the emittance swap technique
  - some of the necessary modification to inject in Elettra 2.0 has been already tested with Elettra.
  - the booster remains the same;

- Bunch by Bunch kickers
  - Due to the new vacuum pipe size the old multi bunch kickers, transverse and longitudinal, can not be reused;
  - The new kickers, developed in collaboration with PSI, have been already validated in SLS 2.

1.4 Motivations and goals of this thesis

This work is conceived with the aim of contributing to the development of advanced components for Elettra 2.0, focusing on two complementary yet closely related aspects: the study and minimization of the impedance generated by selected components installed in the vacuum chamber, and the design of a button-type Beam Position Monitor optimized for the new machine. These efforts are intended to ensure beam stability, mitigate undesirable collective effects [10], and enable precise control of the beam trajectory along the ring, factors that are essential for the scientific success of the entire facility. More specifically, the objectives of this work are:

- Primary Objective: design and prototypical realisation of beam position monitors (BPMs) for the new Elettra 2.0 light source, which are essential devices for measuring the position of the accumulated beam in the accelerator.
  The principal challenge in developing these devices lies in the significantly reduced dimensions of the vacuum chambers in fourth-generation machines such as Elettra 2.0, especially when compared with previous-generation facilities like the original Elettra. In the specific case examined, the ratio between the corresponding axes of the rhomboidal chamber at the BPM site is 3:1. While this scale factor might appear to be a purely geometric issue, it has important physical implications. For a given stored current in the machine, the image currents induced by the beam on the inner surface of the vacuum chamber scale inversely with the chamber size. Consequently, in Elettra 2.0 the surface current density will be approximately three times greater than those in Elettra (assuming identical chamber materials). A direct consequence of this increased current density is that electromagnetic and thermal effects, previously negligible in the original Elettra, can no longer be ignored in Elettra 2.0. Another critical factor is the variation in electron bunch length under different machine operating modes (e.g. Single Bunch, Multi Bunch, Hybrid, CRAB (deflecting cavity)), which influences the shape of the induced image currents. In the context of BPMs, it is essential to optimise the extraction of a portion of the beam's energy via the four pick-ups. This process must balance two key objectives: minimising the parasitic effects introduced by the BPMs themselves, and ensuring that the output signal remains sufficiently strong to be reliably detected under all operating conditions.

- Secondary objective: to assess the coupling impedance of several machine components beyond the BPMs, such as transitions, flanges, and vacuum valves. In particular, the thesis presents a detailed analysis of two types of vacuum-sealing flanges. Due to their specific structural characteristics, these flanges could potentially generate adverse effects that may compromise the optimal performance of Elettra 2.0.

1.5 Thesis overview

The thesis is divided into six chapters, each addressing one of the topics related to the development of the work.

- Chapter 1 introduces the project, outlining its technical and scientific motivations and presenting the main objectives of the thesis.

- Chapter 2 provides a brief summary of wakefield theory and the corresponding impedance concepts.

- Chapter 3 discusses the study conducted on impedance contributions of two types of vacuum sealing flanges. Given the large number of such components to be installed in the machine, it is essential to minimise their impedance contribution as much as possible. A solution is proposed to minimize their impact on the overall machine impedance to negligible levels.

- Chapter 4 presents the general theory underlying the operation of button-type BPMs and the study of their contribution to the machine coupling impedance. The theory discussed in this chapter formed the foundation for developing the BPM design for Elettra 2.0.

- Chapter 5 describes three families of BPMs that were entirely designed, built, and tested in-house. Thanks to these devices, the complete data acquisition process planned for Elettra 2.0 has already been validated on the current Elettra machine. This chapter presents also the development of the dedicated metallic adapter, indicated as test fixture, used for some BPM measurements.

- Chapter 6 describes the electromagnetic site test performed on the first sixteenth Elettra 2.0 pick up prototypes constructed by a company on the base of designs presented in chapter 5

Chapter 2

Wakefields and impedances

2.1 Introduction

Three fundamental elements characterize any particle accelerator:

- charged particles;
- electromagnetic fields;
- defined paths in vacuum along which the particles propagate

Depending on the specific task to which each real particle accelerator is devoted to (ion source, light source, collider, ...), the contributions of each element have to be carefully evaluated, designed and integrated in order to get a machine working as expected. A detailed knowledge about the wanted and unwanted (parasitic) interactions between electromagnetic fields and charged particles propagating in a vacuum pipe is a prerequisite to the design of particle accelerators.

In this chapter a specific type of electromagnetic effect induced by a charged particle beam propagating in and interacting with a conductive enclosure is briefly sum up [35, 36]. Such effect, indicated as wakefield in time domain, is usually considered parasitic because it can alter the nominal propagation dynamics of the beam. In particular cases, such as wakefield accelerators, it is the primary focus of the accelerator design. The time domain counterpart of the wakefield is called beam coupling impedance.

2.2 Charged particles propagating in vacuum (empty space)

It is well known from electrodynamics that a charged particle q moving at constant velocity (straight line) $\vec{v}$ in vacuum, described by the current density vector $q \cdot \vec{v}$, is surrounded by its own electromagnetic fields ($\vec{E}$,$\vec{B}$), whose distribution in space can be calculated applying the Lorentz transformation to the electrostatic field of q [28]. In ultra-relativistic regime, when the propagation speed module $|\vec{v}|$ is very close to the speed of light, as is the case of Elettra 2.0, the field sustained by q propagate according to the transverse electromagnetic mode (TEM):

- the electric field irradiates from the charge q, and is orthogonal to $\vec{v}$;
- the magnetic field encircles the charge q, and is orthogonal to $\vec{v}$;
- the magnetic field is orthogonal to the electric field;
- the Poynting vector $\vec{S}$, $\vec{S} = \vec{E} \times \vec{H}$, defines the power flow of the electromagnetic field produced by q;
- electric and magnetic field lines are not confined; in principle, they extend to infinity.

2.3 Charged particles propagating in conducting vacuum pipes

A charge q (primary source) running inside a particle accelerator will terminate its electric field lines on image charges located in the conducting bulk of the accelerator's vacuum pipe (skin effect). The magnetic filed lines due to the motion of the charge will be shielded by the induced surface currents. The distribution of such induced charge and current depends on:

- the vacuum pipe inner surface shape (geometric boundary conditions);
- the vacuum pipe material (material boundary conditions);
- the trajectory of the primary source with respect to the vacuum pipe inner surface.

Once the distribution of the induced charge and current is known, it is possible to calculate its effects on the propagation of the primary source due to the electromagnetic energy radiated back into the vacuum pipe (secondary source effect).

2.4 Electromagnetic forces on moving charged particles

In order to track the propagation of a point like charged particle T inside an accelerator, i.e. calculate the equation of motion of T over time, the initial time t_0, the initial position ($\vec{r}_{TO}$) and velocity ($\vec{v}_{TO}$) of the particle, and the force acting on it along the propagation path must be known. If q is the electric charge carried by the particle T that propagates with velocity $\vec{v}$ through a vacuum region (ε_0,μ_0) that hosts an electromagnetic field ($\vec{E}$,$\vec{H}$), on the particle acts the Lorentz force given by (in vacuum $\vec{B} = \mu_0 \cdot \vec{H}$):

$$\vec{F}(t) = q(\vec{E}(t) + \vec{v_q}(t) \times \vec{B}(t)) \tag{2.1}$$

The particle's momentum $\vec{p}$ ($\vec{p} = m \cdot \vec{v}$) variation over time is given by:

$$\vec{F}(t) = \frac{\mathrm{d}\vec{p}(t)}{\mathrm{d}t} \tag{2.2}$$

In particle accelerators, the total electromagnetic field experienced by a particle is the sum of two contributions:

- the field ($\vec{E}_{imp}$, $\vec{B}_{imp}$) impressed by external sources that is in charge of generating longitudinal and transverse forces that drive the particle T along a defined trajectory;
- the field ($\vec{E}_{sec}$, $\vec{B}_{sec}$) due to the secondary source effect induced by T.

The total force acting on T along its propagation trajectory can therefore be calculated once ($\vec{E}_{imp}$, $\vec{B}_{imp}$) and ($\vec{E}_{sec}$, $\vec{B}_{sec}$) are known in each point inside the machine at any time. The impressed field is known by definition because it is defined by the design of the accelerator. The secondary source field, on the other side, can be calculated only when the charge and current induced by T are known. If by any means is known that ($\vec{E}_{sec}$, $\vec{B}_{sec}$) is negligible compared to ($\vec{E}_{imp}$, $\vec{B}_{imp}$), the design of the accelerator is greatly simplified because T's self induced effects don't affect the propagation. If T propagates at the speed of light (ultra-relativistic regime), the electromagnetic field ($\vec{E}_{sec}$, $\vec{B}_{sec}$) generated by the secondary source, due to the causality principle, exist only behind T. For this reason it is named wakefield.

2.5 Wakefield effect on propagating charges

Consider two charges, a source charge S_{RC} of q_S Coulomb that induces surface charges and currents passing through the accelerator vacuum pipe, and a test charge T_{ST} that probes the electromagnetic effects due to ($\vec{E}_{sec}$, $\vec{B}_{sec}$). The test particle charge is small enough to be considered negligible in terms of induced fields and space charge interactions with S_{RC}.

In the most general case, both the relative distance between S_{RC} and T_{ST} and their relative velocities could be totally free. Try to perform any calculation on a similar model would mean evaluate any possible combination of relative positions and velocities over time. If, instead, it is allowed to take for granted the following two assumptions, the wakefield effects can be split in longitudinal and transverse contributions:

- rigid beam approximation: S_{RC} and T_{ST} propagates along straight and parallel trajectories with equal and constant velocities (constant distance);
- kick approximation: the integrated mechanical effects of the applied Lorentz force along the propagation trajectory are considered as if they were obtained by an impulsive force in an undefined point along the propagation;

Under these hypothesis, the two charges move parallel along the longitudinal axis (Zaxis) of the accelerator structure at the same velocity ($v = \beta \cdot c$). Assuming the particle T_{ST} position described by (x_T, y_T, z_T), and the particle S_{RC} position described by (x_S, y_S, z_S)), the equation of motion for S_{RC} and T_{ST} are:

$$z_S(t) = z_{S0} + v \cdot t = z_{S0} + \beta \cdot c \cdot t \tag{2.3}$$

and

$$z_T(t) = z_{T0} - s = z_{T0} - s + v \cdot t = z_{T0} - s + \beta \cdot c \cdot t \tag{2.4}$$

where z_{S0} and z_{T0} are the positions of S_{RC} and T_{ST} at the time $t = 0$.

The test charge follows the source charge at a longitudinal distance s ($s \geq 0$ by definition) that is kept constant.

$$s = z_S(t) - z_T(t) = z_{T0} - z_{S0} \tag{2.5}$$

Expressed in term of time, the distance between T_{ST} and S_{RC} is: $\tau = \frac{s}{\beta \cdot c}$

The Lorentz force acting on T_{ST} due to S_{RC} can be be split in longitudinal (parallel to the propagation direction) and transverse (orthogonal to the propagation direction) components:

$$\vec{F}(x_S, y_S, x_T, y_T, s, z_T) = (\vec{F}_{x,y}, F_z \cdot \hat{z}) \tag{2.6}$$

where $\hat{z}$ is the unit vector along the z-axis.

2.6 Longitudinal wake function

The longitudinal wake function is defined as the integral of the longitudinal component F_z of the Lorentz force over the trajectory of the test particle normalized with respect to the product of the particle's charges:

$$w_z^f(x_S, y_S, x_T, y_T, s) = -\frac{1}{q_T q_S}\int_{-\infty}^{\infty} F_z(x_S, y_S, x_T, y_T, s, z)dz[V/C] \tag{2.7}$$

To simplify the notation, the variable of integration is denoted by z instead of z_T. The longitudinal electric field E_z acting on the test particle is determined by dividing F_z by the test charge q_S:

$$E_z = \frac{F_z}{q_T}[V/m] \tag{2.8}$$

The total voltage acting on the test particle is determined by integrating the electric field E_z along the test particle's trajectory:

$$V(s) = \int_{-\infty}^{\infty} E_z(x_S, y_S, x_T, y_T, s, z)dz[V] \tag{2.9}$$

The variation of the energy of the test charge, $\Delta Energy_{TST}$, is obtained by multiplying this voltage by q_T:

$$\Delta Energy_{TST}(s) = q_T \cdot V(s)[eV] \tag{2.10}$$

The wake function can then be expressed through E_z:

$$w_z^f(x_S, y_S, x_T, y_T, s) = -\frac{1}{q_S}\int_{-\infty}^{\infty} E_z(x_S, y_S, x_T, y_T, s, z)dz = -\frac{\Delta Energy_{TST}(s)}{(q_T q_S)} \tag{2.11}$$

This equation, through the wake function, summarizes the relationship between the wake field excited by the source particle and the energy variation of a test particle following at a distance s.

2.7 Transverse wake functions

The transverse wake functions are defined, respectively, as the integral of the transverse component F_x and F_y of the Lorentz force over the trajectory of the TST particle normalized with respect to the product of the particle's charges:

$$w_x^f(x_S, y_S, x_T, y_T, s) = \frac{1}{q_T q_S} \int_{-\infty}^{\infty} F_x(x_S, y_S, x_T, y_T, s, z) dz [V/C] \tag{2.12}$$

$$w_y^f(x_S, y_S, x_T, y_T, s) = \frac{1}{q_T q_S} \int_{-\infty}^{\infty} F_y(x_S, y_S, x_T, y_T, s, z) dz [V/C] \tag{2.13}$$

Since the integration path is orthogonal to the force, the transverse wake functions are related to the particle's transverse momentum kicks (expressed in $N \cdot m$):

$$w_x^f(x_S, y_S, x_T, y_T, s) = \frac{1}{q_T q_S} \int_{-\infty}^{\infty} F_x(x_S, y_S, x_T, y_T, s, z) dz = \frac{\Delta p_x(s)}{q_T q_S} \tag{2.14}$$

$$w_y^f(x_S, y_S, x_T, y_T, s) = \frac{1}{q_T q_S} \int_{-\infty}^{\infty} F_y(x_S, y_S, x_T, y_T, s, z) dz = \frac{\Delta p_y(s)}{q_T q_S} \tag{2.15}$$

When both the source and test particles travel along the axis of a vacuum pipe with quadrant symmetry, the transverse components of the Lorentz force, Fx and Fy, are identically zero. Consequently, the particles experience no transverse momentum variation.

The transverse wake functions can be expanded into a power series in the offset of source (x_S,y_S) and test (x_T,y_T) particle. The initial terms of the expansion, under the assumption that the coupling between the x and y transverse planes can be neglected (i.e. the mixed partial derivatives are zero), are given by:

$$\begin{aligned} w_x^f &= w_x^{dip} \Delta x_s + w_x^{quad} \Delta x_t \\ w_y^f &= w_y^{dip} \Delta y_s + w_y^{quad} \Delta y_t \end{aligned} \tag{2.16}$$

where, w_x^{dip} ([V/Cm]) denotes the horizontal dipolar wake function, which expresses the dependence on the source particle's offset Δx_s with respect to the vacuum pipe axis, while w_x^{quad} ([V/Cm]) denotes the horizontal quadrupolar wake function, which expresses the dependence on the test particle's offset Δx_t. w_x^{dip} represents dipole-like transverse deflecting effects. w_x^{quad} represents quadrupole-like transverse effects, related to detuning and focusing/defocusing. The same considerations apply to w_y, w_y^{dip} and w_y^{quad}.

2.8 Effective length of accelerator components

In the previous calculation, the wakefield integration was carried out from -∞ to +∞. This is useful from a theoretical standpoint and does not affect the practical consideration that real accelerator components always have finite dimensions. In the case of resonant cavities, the confinement of the electromagnetic fields provides a clear definition of the device's boundaries. In the case of uniform vacuum pipes, the structure is appropriately studied by considering its properties per unit length. In ultra-relativistic beams, causality ensures that fields exist only behind the source particle, allowing a further reduction of the integration path.

2.9 Longitudinal beam coupling impedance

Considering that the source particle propagating in the accelerator behaves as an impulsive impressed current, and that the longitudinal wake function expresses the energy loss of the test charge due to the voltage induced by the source charge along its trajectory, the relationship between voltage and current can be represented by an impedance. For this reason, passing in time domain, the longitudinal beam coupling impedance is the Fourier transform of the longitudinal wake function:

$$Z_{\|}(\omega) = \int_{-\infty}^{\infty} w_z^f(s) e^{-\dfrac{j\omega s}{v}} \frac{ds}{v} [\Omega] \tag{2.17}$$

were j is the imaginary unit, $\omega = 2\pi f$ is the angular frequency and v is the speed of the charged particle. Following this definition of the Fourier transform, the 2 π scaling factor is applied to the anti trasformation.

2.10 Transverse beam coupling impedances

The transverse beam coupling impedances are calculated in analogy with the longitudinal case, but with the introduction of a 90 degree phase shift:

$$\begin{aligned} Z_{\perp}^{dip}(\omega) &= j \int_{-\infty}^{\infty} w_{\perp}^{dip}(s) e^{-\frac{j\omega s}{v}} \frac{ds}{v} [\Omega/m] \\ Z_{\perp}^{quad}(\omega) &= j \int_{-\infty}^{\infty} w_{\perp}^{quad}(s) e^{-\frac{j\omega s}{v}} \frac{ds}{v} [\Omega/m] \end{aligned} \tag{2.18}$$

The symbol $\perp$ indicates the transverse plane component, so that:

$$\begin{aligned} Z_x(\omega) &= Z_x^{dip}(\omega)\Delta x_s + Z_x^{quad}(\omega)\Delta x_t \\ Z_y(\omega) &= Z_y^{dip}(\omega)\Delta y_s + Z_y^{quad}(\omega)\Delta y_t \end{aligned} \tag{2.19}$$

2.11 Wake potentials

The single-particle model adopted thus far treats the simplest theoretical case, in which the interaction is restricted to point like charges. To extend it to source and test charge configurations with a spatial distribution, it is sufficient, owing to the linearity of Maxwell's equations in vacuum, to apply the convolution integral in time domain. This is the common approach in signal theory: once the time domain impulse response of a linear time-invariant system is known, the response to any other signal can be obtained by convolution. If the source has a spatial charge distribution $\lambda_l(z)$ normalized with respect to the total source charge Q_s, described by its linear charge density along the propagation direction (the z axis), the total effect of this distribution on a test charge is obtained by the convolution of the wake function with the charge density.
The longitudinal wake potential is then calculated by:

$$W_z^P(x_S, y_S, x_T, y_T, s) = \frac{1}{q_T Q_S}\int_{-\infty}^{\infty} w_z^f(x_S, y_S, x_T, y_T, s-z)\lambda_l(z)dz \tag{2.20}$$

Applying the convolution property of the Fourier transform, the Fourier transform of the wake potential is equal to the product of the Fourier transforms of the charge distribution and the longitudinal beam coupling impedance.
The transverse momentum kicks due to a source charge distribution can be calculated in the same manner:

$$W_x^K(x_S, y_S, x_T, y_T, s) = \frac{1}{q_T Q_S}\int_{-\infty}^{\infty} w_x^f(x_S, y_S, x_T, y_T, s-z)\lambda_l(z)dz \tag{2.21}$$

$$W_y^K(x_S, y_S, x_T, y_T, s) = \frac{1}{q_T Q_S}\int_{-\infty}^{\infty} w_y^f(x_S, y_S, x_T, y_T, s-z)\lambda_l(z)dz \tag{2.22}$$

2.12 Impedance model of an accelerator

An accelerator may be represented as a cascade of impedances traversed by the beam. In circular machines, the periodic recirculation of the beam can lead to beam-coupled instabilities, which are a central concern in collective beam dynamics. This aspect may be tackled once all accelerator components have been modelled in terms of their individual impedances.

Chapter 3

Beam coupling impedance contribution of flange aperture gaps

3.1 Introduction

This chapter focuses on estimating the contribution of the joints located between different sections of the vacuum chamber to the total beam coupling impedance of Elettra 2.0. This problem has also been addressed in other contexts such as CERN-SPS, where RF contacts have been used [11, 25], or PSI-SLS2, where zero gap flanges have been chosen [50]. This chapter describes a comparative numerical analysis of the beam coupling impedance of two types of vacuum flanges, taking into account different gap thicknesses between them. The obtained results are exploited to discuss the impact of the different impedance contributions in the forthcoming development of Elettra 2.0

3.2 Flanges

Flanges are commonly used to connect with ultrahigh-vacuum leak tight performance different sections of the vacuum pipe of any kind of particle accelerator. They are usually considered pure vacuum components, but this is totally wrong when they operate "illuminated" by the beam. In such a case, because of the beam induced currents, the flanges must be considered as waveguide elements. In terms of beam coupling impedance, we can state that the electromagnetic behavior of the flanges should be pure resistive wall type, that scales linearly with the joint length. Practical constructive and assembly constraints, that are strictly related to economical aspects, suggested to calculate the effects of single joint on wake fields, which could be not negligible but still acceptable. At same time, due to the high number of such junctions planned for Elettra 2.0, around 250, their contribution to the whole machine impedance budget could be not negligible exceeding the impedance budget stability limit accepted for the machine.

3.2.1 Flange types

The classical zero gap flanges (VATSEAL®) [44, 47] have not been investigated because, by design, they behave very close to a continue vacuum pipe without any joint, satisfying at the same time both the vacuum leak and coupling impedance requirements. Accordingly, their contribution to the overall impedance budget can be regarded as negligible. The drawback of these flanges is their high cost, which motivates the search for a more economical alternative, even if it is less effective from the impedance point of view. Two non zero gap flanges were considered, both based on the same type of vacuum seal gasket (no microwave), the first one is a Spigot Flange Lip (SFL) type, while the second one is a Spigot Flange Planar (SFP) type.

3.2.2 Mechanical Model

The mechanical drawings of the flanges under evaluation are detailed in Figure 3.1. The main difference between SFL and SFP types resides in the geometry of the resulting gap that separates the opposite sides of the vacuum joint: in the SFP case, the gap volume is reduced with respect to the SFP's one. This is the result of the different geometry of the transition between the gasket housing and the rhomboidal vacuum chamber.

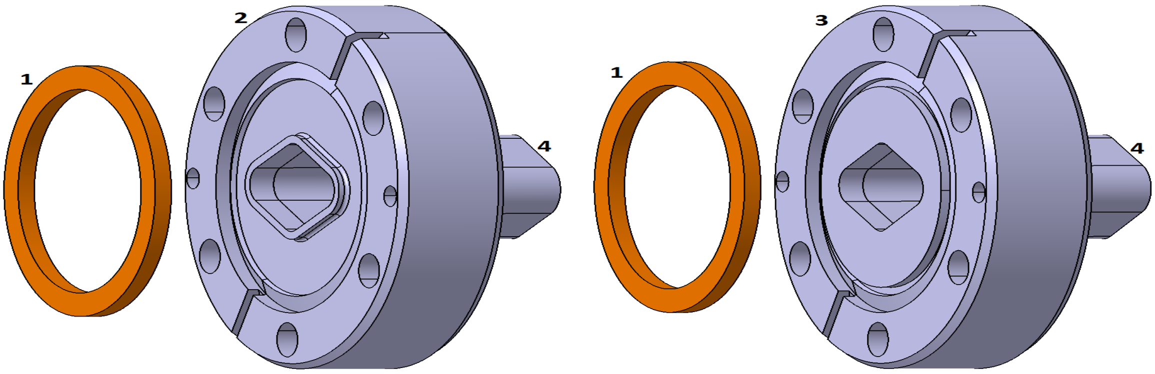

Fig. 3.1 Flanges mechanical drawings. On the left, the SFL type (2) and, on the right, the SFP type (3). Also the gasket (1) and the rhomboidal vacuum pipe (4) are shown.

3.2.3 Electromagnetic Model

A simplified electromagnetic (EM) model has been derived from the mechanical one to simulate the interaction between the charged particle beam and its surrounding environment by considering the short vacuum pipes, opposite-facing flanges and the gasket. To simplify the structure, only the surfaces, volumes and materials interacting with the EM field of the charged particles beam have been taken into account. The basic EM models of the SFP and SFL are shown in Figure 3.2, where the gasket and the flanges are assumed of the same material being considered as the background material in the model. The gap G and the cavity depth C of the parasitic cavities formed by the opposite sides of the flanges are also illustrated. A direct comparison between the two shapes shows that the passive cavity volume of SFL is larger than that of SFP.

The correspondence between the mechanical and EM models is summarized in Table 3.1.

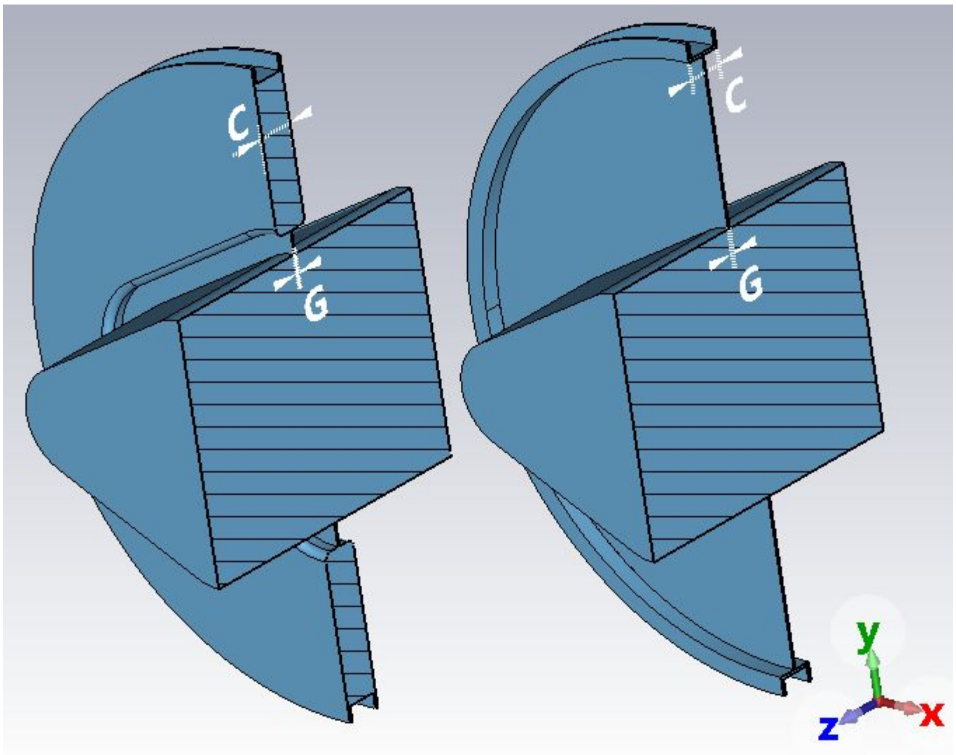

Fig. 3.2 Electromagnetic model of the two flanges: 3D longitudinal cut views. The SFL type (left) and the SFP type (right).

Table 3.1 Correspondence between mechanical and electromagnetic model.

Mechanical	**Electromagnetic**
inner vacuum volume	inner vacuum volume
materials wall thickness*	background lossy metal
input and output apertures	open boundaries

* The minimum thickness of the conductive materials is 1.5 mm, large enough to guarantee the full electromagnetic field penetration in the conductors due to the skin effect at the considered frequencies.

3.3 Electromagnetic simulations

3.3.1 WakeField Simulations - Longitudinal axis

Two sets of EM simulations are carried out resorting to CST Particle Studio by Dassault Systèmes Simulia [14]. The first set aims to evaluate and compare the longitudinal beam coupling impedance of the two types of flanges assuming the nominal geometries, while the second set focuses on the evaluation of the effects determined by the constructive tolerances and the parameter variations.

The transverse symmetry of both types of flanges allows one to exploit the symmetry with respect to the $Y-Z$ and $X-Z$ planes for the boundary conditions, thus enabling to simulate just one-fourth of the actual EM structure. Moreover, in order to find a reasonable trade-off between the number of mesh cells, the convergence results, and the computational time, a suitable number of preliminary simulations is carried out by varying the mesh density. In the analysis, the large aspect ratio of the flanges is implicitly taken into account by maintaining an oversized mesh density, which guarantees that the gap is resolved with sufficient geometric detail.

3.3.2 Flanges Nominal Dimensions

The nominal dimensions of the flanges are:

- gap: G = 0.1 mm,
- cavity depth: C = 2.4 mm,
- total longitudinal length: 20 mm,
- cavity main radius (gasket inner radius): 19.6 mm,

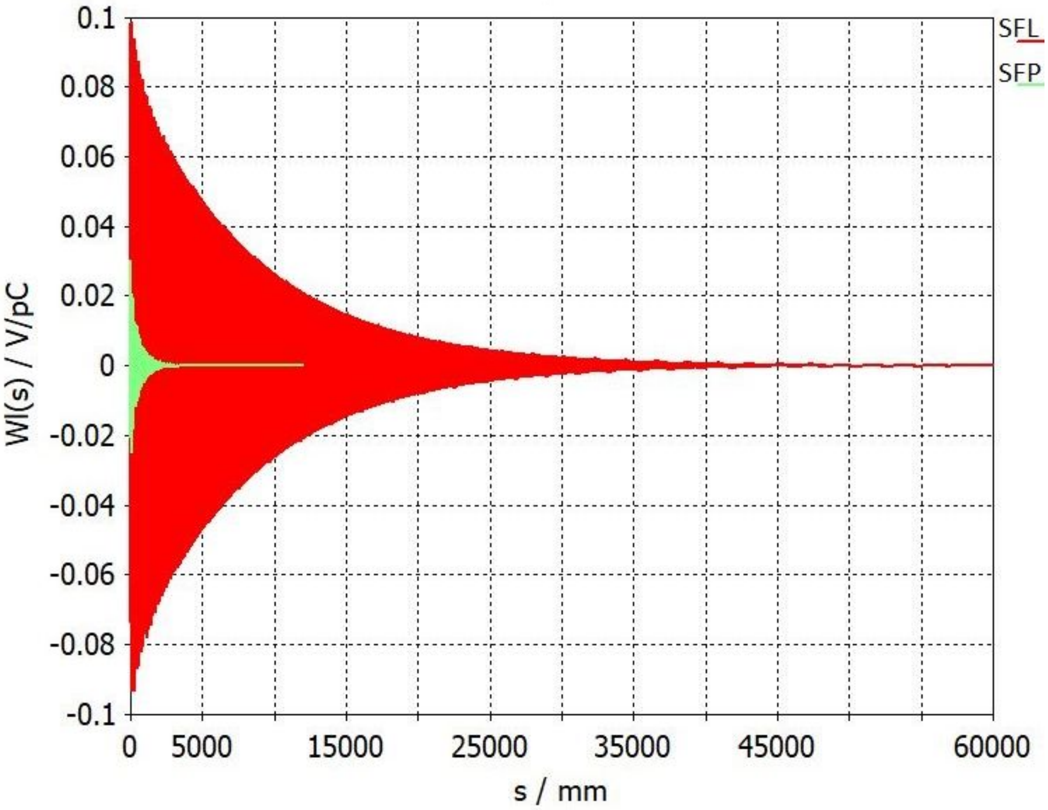

Fig. 3.3 SFL (red) and SFP (green) wake potential comparison.

- input and output apertures: the same as the rhomboidal vacuum pipe's inner dimensions (27 × 17 mm).

The bunch length of the relativistic exciting Gaussian beam has been set at $\sigma_{\text{beam}} = 4$ mm in order to have an impedance estimation up to 25 GHz. The lossy metal considered as background is the AISI 316L stainless steel, with an electric conductivity $\sigma_{316\text{L}} = 1.35 \times 10^6$ S/m at room temperature. In order to evaluate the longitudinal impedance of both SFL and SFP, the exciting beam and the wakefield integration path are set on the longitudinal z-axis of the simulated structures, and the wake potentials are calculated by the Wakefield solver. In Figure 3.3 the SFL (red trace) and SFP (green trace) wake potentials appear overlapped.

A first qualitative comparison between the wake potential lengths and initial amplitudes, considered together with the shapes of the parasitic cavities (as depicted in Figure 3.2), suggests that the SFL cavity has a higher energy storage capability with respect to the SFP one. Performing some numerical analyses, both the broadband and narrowband (resonant) impedance contributions can be estimated, thus enabling a quantitative comparison between the SFL and SFP flange behavior in the frequency domain, as depicted in Figure 3.4. Each

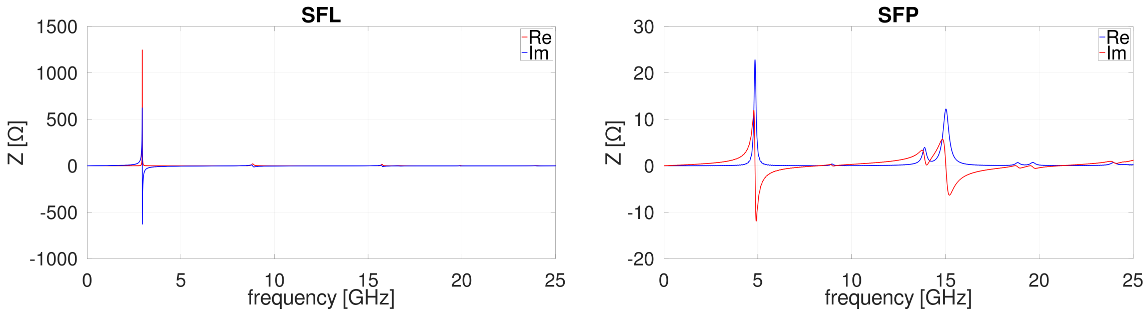

(a) (b)

Fig. 3.4 Longitudinal impedance: SFL (left) and SFP (right).

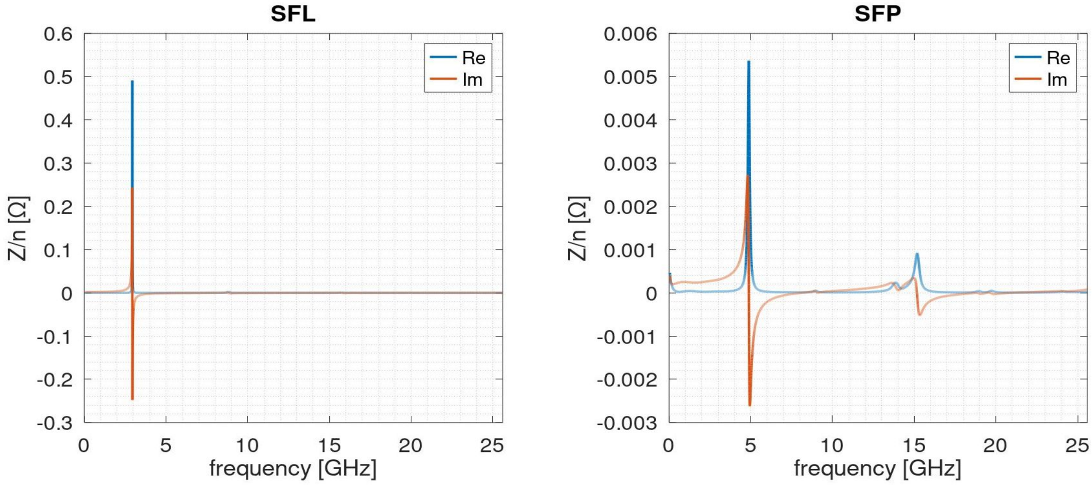

Fig. 3.5 Normalized longitudinal impedance: SFL (left) and SFP (right).

narrowband impedance contribution is characterized by its resonant frequency f_r, its shunt resistance R_s (i.e. the amplitude of the real part of the complex impedance at the resonance frequency), and the quality factor Q. These values are summarized in Table 3.2 for the main longitudinal resonant mode of the investigated flanges.

The longitudinal analysis is then completed by calculating the normalized longitudinal impedances Z/n [49] (see Figure 3.5), where $n = f/f_{rev}$ is the mode number, with f_{rev} (1.157 MHz) denoting the revolution frequency of the accelerator. The wake loss factors

Table 3.2 f_r, R_s, Q and Re(Z/n) comparison between the SFL and SFP dominant resonance.

	f_r [GHz]	R_s [Ω]	Q	Re(Z/n) [Ω]
SFL	2.9388	1247.7	287	0.4914
SFP	4.8793	22.64	36	5.4×10^{-3}

(WLFs) for SFL and SFP are 4.83×10^{-2} V/pC and 1.31×10^{-2} V/pC, respectively. A comparison between the real parts of Z/n shows that the SFL type is almost 100 times higher than the SFP one, while the ratio of WLFs is about 3.69.

3.3.3 Mechanical Tolerances and Parametric Simulations

The previously presented EM analysis on the SFP nominal model has allowed the evaluation of the variations of the longitudinal impedance for different geometric tolerances. Assuming that only one parameter varies at a time, we can now estimate the effects introduced by the manufacturing and assembly tolerances. The considered parameter variations and the corresponding effects can be listed and discussed as follows.

- The expansion of the gap G from 0.1 mm to 0.4 mm in steps of 0.1 mm determines the increase of both the main and secondary peak amplitude of the real part of the longitudinal impedance, with a frequency shift toward higher values (Figure 3.6). The WLF increases too (Table 3.3).
- The increase of the gasket inner radius from 19.6 mm to 20.0 mm determines the growth of both the main and secondary peak amplitude of the real part of the longitudinal impedance, with a frequency shift toward lower values. The WLF remains constant.
- The increase of the longitudinal length from 10 mm to 70 mm does not provide appreciable modifications on the real and imaginary part of the longitudinal impedance. This is because of the long range nature of the resonant field trapped in the gap, whose frequency (4.8793 GHz) is below the cutoff frequency of the vacuum pipe (7 GHz).

Table 3.3 Wake loss factor varying the gap G.

G[mm]	0.1	0.2	0.3	0.4
WLF [10^{-2} V/pC]	1.31	2.48	3.63	4.77

3.3.4 Beam power loss

The power lost by the beam when passing through the flange depends on the flange's loss factor, $k_{\parallel}$, according to the following relationship:

$$P = \frac{k_{\parallel}(I_{stored})^2}{N_{bunches} f_{rev}} \tag{3.1}$$

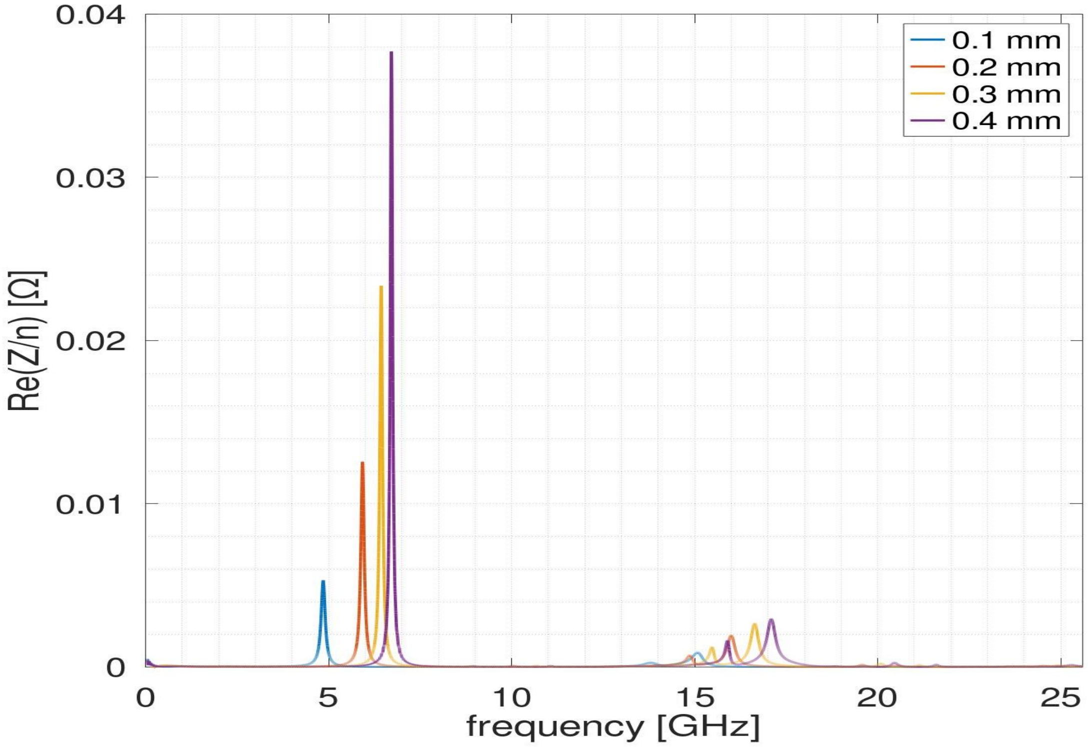

Fig. 3.6 Parametric dependence of Re(Z/n) on the gap G.

Assuming 400 mA the stored beam current foreseen for Elettra 2.0, $N_{bunches}$ = 432 and f_{rev} = 1.1574 MHz:

- P = 4.2 W for the nominal SFP;
- P = 15.46 W for the nominal SFL;
- the worst case of SFL, for the gap $G = 0.4mm$, dissipates almost the same power as the nominal SFL.

The total power dissipated by the beam is then calculated multiplying the above values by the total number of flanges (250):

- P = 1050 W for the nominal SFP;
- P = 3865 W for the nominal SFL;

3.3.5 WakeField Simulations - Transverse plane

Because of its high wake loss factor, the SFL type flange was excluded from other types of electromagnetic investigations as unsuitable for use in the Elettra 2.0 accelerator. The results

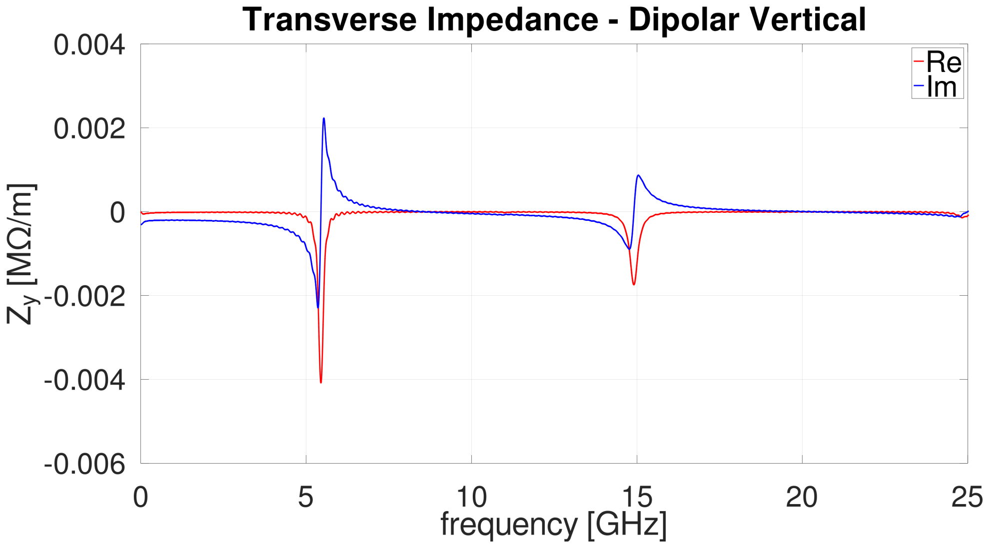

Fig. 3.7 Transverse Dipolar vertical beam coupling impedance - 1 mm vertical offset.

of the numerical simulations performed to get the values of the five fundamental components of the transverse beam coupling impedance of the SFP type flange (nominal dimensions) are reported below. Due to the long calculation time, the truncation errors due to a not fully vanished wake potential have been accepted. The exciting beam and the background material are the same used in the longitudinal simulations.

Monopolar contribution

The axis symmetric geometry of the SFP flange assures that the net transverse wake field effects on a beam propagating on axis is zero, therefore no further simulations are required in order to calculate this contribution. The wake field integration line is centered in $(x_{wf}, y_{wf}) = (0,0)$.

Dipolar contribution - vertical plane

To calculate the dipolar vertical contribution the exciting beam is shifted +1 mm off axis in the vertical direction, that is $(x_{beam}, y_{beam}) = (0,1)$. The wake field integration line is centered in $(x_{wf}, y_{wf}) = (0,0)$. The impedance is shown in Figure 3.7. Kick-Factor y : -2.60-03 V/pC/mm

Dipolar contribution - horizontal plane

To calculate the dipolar horizontal contribution the exciting beam is shifted +3 mm off axis in the horizontal direction, that is (xbeam, ybeam) = (3, 0). The wake field integration line

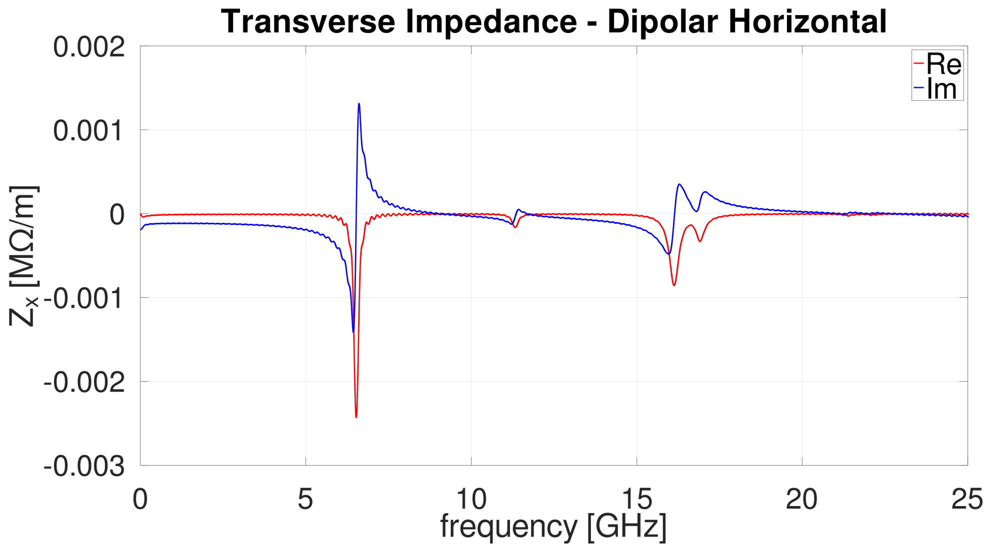

Fig. 3.8 Transverse Dipolar horizontal beam coupling impedance - 3 mm horizontal offset.

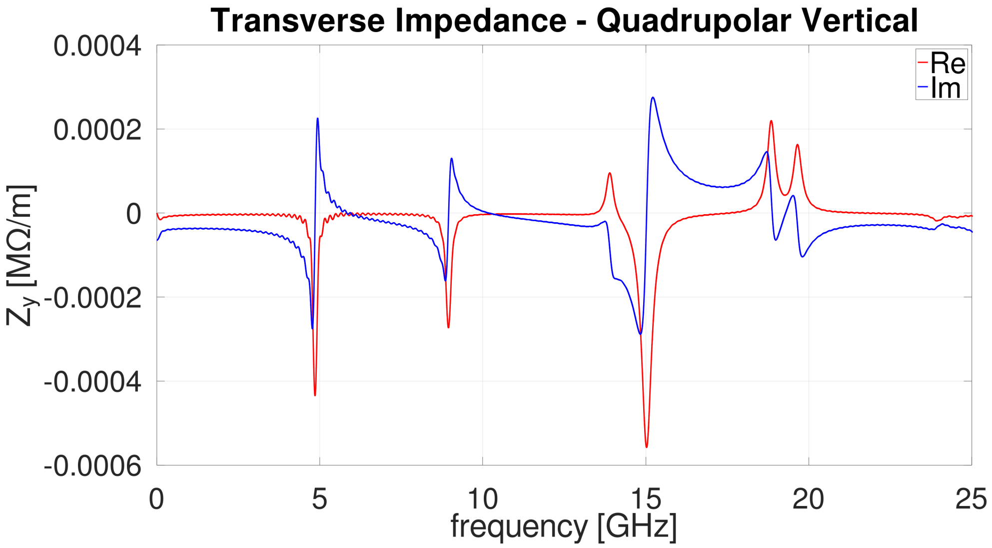

Fig. 3.9 Transverse Quadrupolar vertical beam coupling impedance - 1 mm vertical offset.

is centered in $(x_{wf}, y_{wf}) = (0,0)$. The impedance is shown in Figure 3.8. Kick-Factor x : -1.82e-03 V/pC/mm

Quadrupolar contribution - vertical plane

To calculate the quadrupolar vertical contribution the exciting beam is on axis, that is $(x_{beam}, y_{beam}) = (0,0)$, while the wake field integration line is centered in $(x_{wf}, y_{wf}) = (0,1)$. The impedance is shown in Figure 3.9. Kick-Factor y : 5.53e-04 V/pC/mm

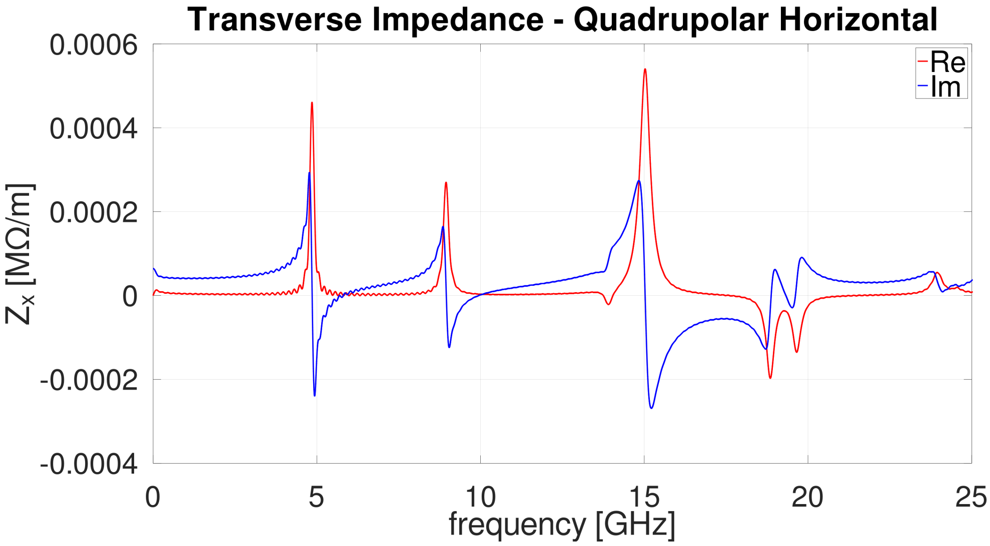

Fig. 3.10 Transverse Quadrupolar horizontal beam coupling impedance - 3 mm offset.

Quadrupolar contribution - horizontal plane

To calculate the quadrupolar vertical contribution the exciting beam is on axis, that is $(x_{beam}, y_{beam}) = (0,0)$, while the wake field integration line is centered in $(x_{wf}, y_{wf}) = (0,3)$. The impedance is shown in Figure 3.10. Kick-Factor x : -6.46e-04 V/pC/mm

3.3.6 Eigenmode Simulations

In order to cross-check the results obtained by the wakefield solver, both flanges have also been investigated by the eigenmode solver (CST). In the SFL only the longitudinal impedance has been calculated. This approach is meaningful due to the resonant nature of SFP and SFL flanges. Because the eigenmode and wakefield solvers rely on different calculation strategies, meshing procedures, and excitation models, great caution is needed when comparing their results. Such methodological differences can introduce numerical discrepancies even when the underlying geometry is the same.

SFL longitudinal

The high quality factor Q of the fundamental resonant mode of the SFL flange imposes a long simulation time in order to assure the wake potential oscillation has decayed to a negligible amplitude compared to its initial one. This is the first critical point when comparing with the corresponding results obtained with the eigenmode solver. The different mesh type between the two solvers is the second critical point. For these two reasons the shunt impedance

Table 3.4 f_r, R_s and Q comparison between wakefield (WF) and eigenmode (EIG) solvers of the fundamental mode of the SFL.

	f_r [GHz]	R_s [Ω]	Q
WF	2.9388	1247.7	287
EIG	2.9145	818.3	163.7

Table 3.5 comparison between the first two high order mode frequencies of the SFL calculated by the wakefield (WF) and eigenmode (EIG) solvers.

	f_{rHOM1} [GHz]	f_{rHOM2} [GHz]
WF	8.8405	15.741
EIG	8.8457	15.725

and the quality factor are quite different between the two solvers. The resonant frequency, that is less sensitive to numerical dispersion, is practically the same in the two cases. The results are reported in Table 3.4. The other two resonant frequencies able to couple with the on axis beam found by wakefield solver are reported in Table 3.5, where are indicated the corresponding frequencies found by the eigenmode solver. An intermediate mode located at 15.1141 GHz has been found by the eigenmode solver, but it is not excited by the wakefield solver.

SFP longitudinal

The low quality factor Q of the fundamental resonant mode of the SFP flange makes it possible to perform accurate electromagnetic investigations at a reasonable calculation time, long enough to assure that the wake potential is completely vanished. The comparison of the results obtained through the wakefield and the eigenmode solver is reported in Table 3.6.

The three high order mode peaks found by the wakefield solver and the corresponding ones of the eigenmode solver are reported in Table 3.7. A comparison between the shapes of the fields obtained by electric and magnetic field monitors in the wakefield simulation with the corresponding fields calculated by the eigenmode solver confirm the correspondence between the two simulations.

Table 3.6 f_r, R_s and Q comparison between wakefield (WF) and eigenmode (EIG) solvers of the fundamental mode of the SFP.

	f_r [GHz]	R_s [Ω]	Q
WF	4.8793	22.64	36
EIG	4.8918	21.65	24.83

Table 3.7 comparison between the first three high order mode frequencies of the SFP calculated by the wakefield (WF) and eigenmode (EIG) solvers.

	f_{rHOM1} [GHz]	f_{rHOM2} [GHz]	f_{rHOM3} [GHz]
WF	8.9538	13.89	15.023
EIG	9.0295	14.04	15.178

3.4 Beam coupling impedance mitigation

In order to further reduce the longitudinal impedance, and consequently the RF heating due to the power lost by the beam, the cavity behind the gap has to be shielded as much as possible against the currents induced by the propagating beam. A straightforward yet effective in-house development is the RF contact gasket, with its mechanical model and mounting details depicted in Figure 3.11.

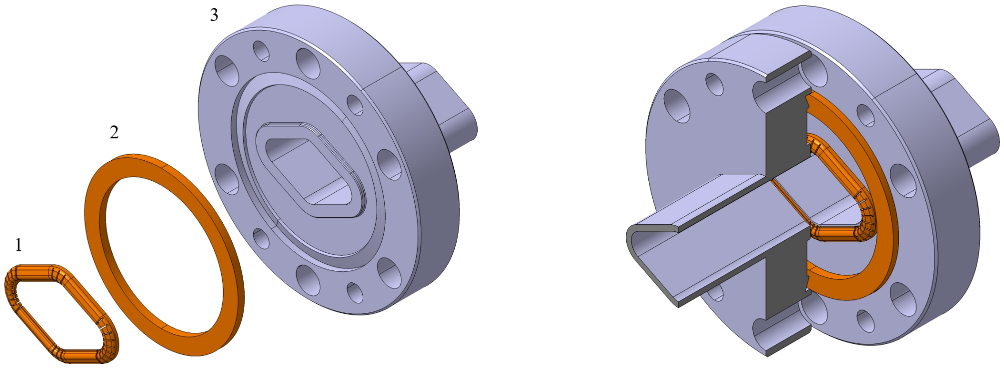

(a) (b)

Fig. 3.11 Rhomboidal RF gasket application: (**a**) the assembly before mounting, the RF contact gasket (1), the CF vacuum gasket (2), the SFL CF40 flange (3)(**b**) full assembly. (courtesy I. Mrak)

The rhomboidal RF gasket (1) is in charge to electrically connect the two opposite sides of the flange, closing the gap along almost all its perimeter. The outer edge of the lip is used for the gasket positioning and keeps the gasket in place during assembly. The RF gasket mounted on a vacuum tightness test flange is shown in Figure 3.12.

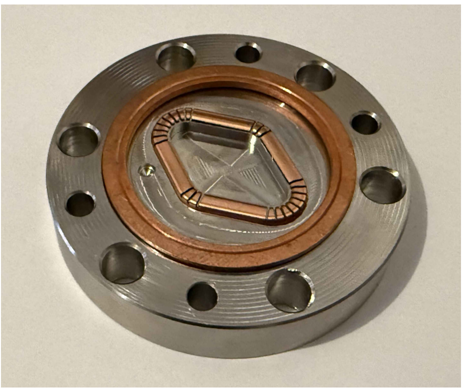

Fig. 3.12 RF gasket mounted on a flange for vacuum tests.

Residual apertures along the RF gasket are the ports for the electromagnetic energy of the beam to enter the cavity. Due to the reduced dimension of such apertures, the coupling between the cavity and the beam is almost negligible, as confirmed by the wakefield simulation performed on the electromagnetic model depicted in Figure 3.13. Figure 3.14 shows the results of the wakefield simulation: in (a) the wake potential, in (b) the wake impedance, in (c) monitor current in the cavity behind the gap (calculated over a circular closed loop), in (d) voltage monitor behind the gap (calculated along a straight line). The monitors detect a few energy filtering through the RF gasket apertures, that indicates that the mesh cell number is high enough not to short circuit the gap because of meshing.

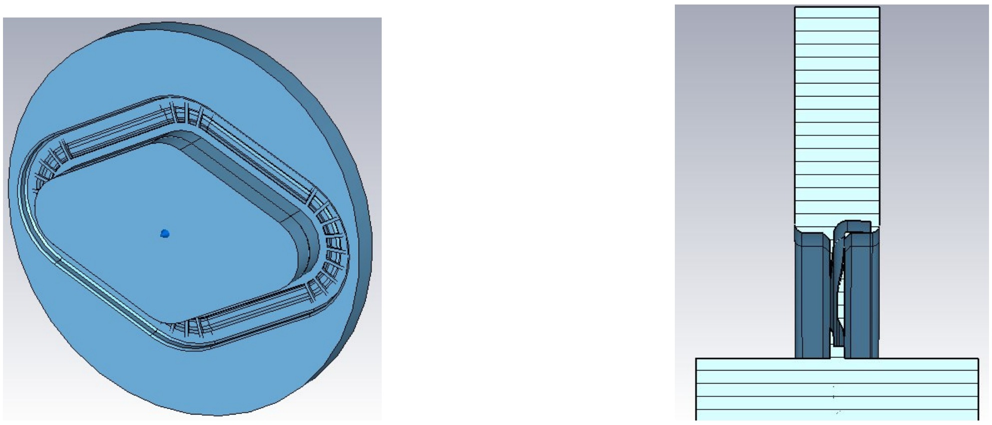

(a) RF gasket electromagnetic model

(b) RF gasket electromagnetic model cross view

Fig. 3.13 RF gasket electromagnetic model

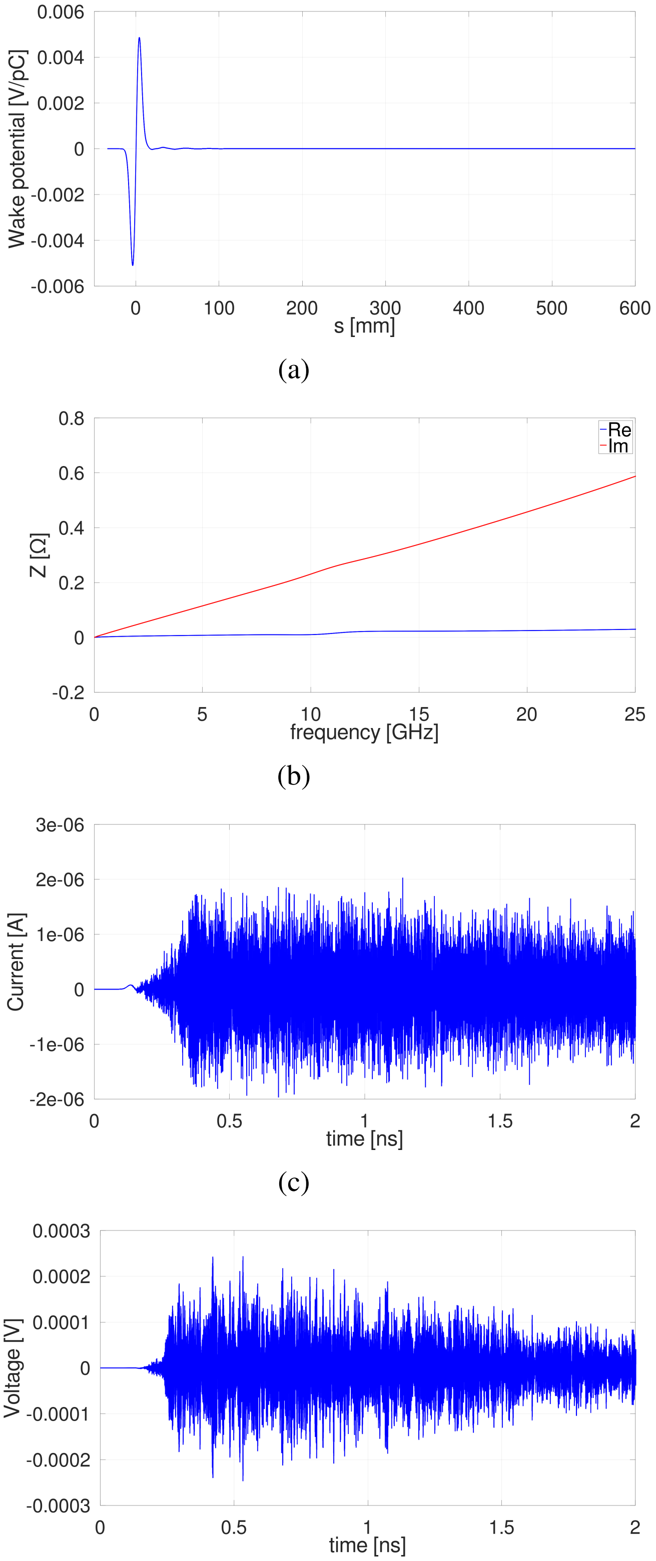

(a)

(b)

(c)

(d)

Fig. 3.14 Wake potential (**a**), wake impedance (**b**), voltage monitor signal (**c**), and current monitor signal(**d**) for $\sigma_{\rm rms} = 4$ mm.

As can be seen by comparing Figure 3.1 and Figure 3.11, the introduction of the RF gasket allows the vacuum seal (round gasket) to be decoupled from the RF shielding (rhomboidal RF gasket).

3.5 Conclusions

The longitudinal normalized impedance and the wake loss factor are useful to provide an effective description of the EM interaction between the charged particle beam and its surroundings. The simulations performed showed that the normalized longitudinal impedance of the SFP flange type is one hundred times lower than the SFL one, thus suggesting the opportunity of avoiding the installation of this type of flange. Furthermore, thanks to the results of the parametric analysis on the SFP type, it has been shown the importance of matching the geometric tolerance limit values for both the gap and the gasket radius. It is worth mentioning that the real part of the impedance is also related to the RF heating, which could represent a serious issue, both in terms of cooling and extra RF power that the accelerating cavities have to deliver to the beam. Thanks to the in-house design of the rhomboidal RF gasket, the SFL flange can accommodate the gasket, which guarantees highly effective shielding of the inner cavity.

Chapter 4

Button type Beam Position Monitor

4.1 Introduction

To detect the longitudinal and transverse positions of electron bunches circulating inside a storage ring or, in general, in a particle accelerator, a number of beam position monitors (BPM) must be placed along the orbit (trajectory) of the beam [31, 39, 23]. The BPMs capture a portion of the beam electromagnetic energy, converting it in electric signals that are transmitted to radio frequency receivers, which process them to compute the beam position information, see Figure 4.1 [8].

Once calculated, the position information is delivered to the machine's control system. Comparing the measured beam position to the "ideal" one defined by the theoretical machine optics, the orbit control system is then able to apply real time correction actions aimed to assure the quality of the photon beams delivered to the users. The quality of each emitted photon beam is defined by parameters such as brilliance, intensity, collimation and the stability of the source point position. The BPMs are the fundamental sensors of the beam position control chain, directly affecting with their performance the whole accelerator one. As a rule of thumb, the design complexity of BPMs increases over time, moving from one generation of light sources to the next [40, 51, 38], in order to meet the increasingly

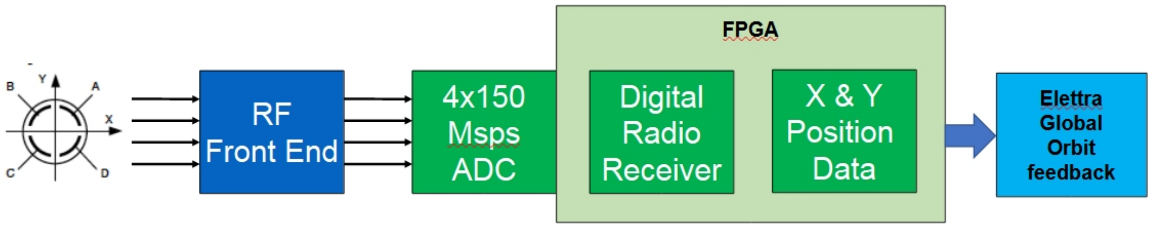

Fig. 4.1 Beam induced signals acquisition chain.

stringent design constraints required to satisfy the user expectations expressed in terms of higher photon beam quality (higher brilliance, higher intensity, higher collimation). The fourth-generation synchrotron light sources are optimized for X-ray production [26, 33], and have non-uniform filling patterns, higher stored current, shorter bunch lengths and smaller vacuum pipe cross-section dimensions compared to third-generation machines. Moreover, for particular applications, transverse deflecting cavities could be introduced to further extend machine's capabilities [17]. All these considerations make computer-aided engineering tools essential for BPM design. Numerical simulations allow to evaluate electromagnetic and thermal effects that simplified analytical models either neglected or approximated too roughly in the past, but which have now become non-negligible.

By design, the BPM is an integral part of the accelerator vacuum chamber and operates very close to the stored beam. Its electromagnetic coupling with the beam must therefore be minimized as much as possible. Ideally, only resistive wall type contribution should be present, to ensure a low impact on the global machine impedance. A low beam coupling impedance contribution is also beneficial in terms of dissipated power (wake losses) and local heating effects. To detect the longitudinal and transverse positions of the charged particle bunches, part of the beam EM energy has to be extracted by the BPM device, thus introducing an additional loading effect that increases the BPM beam coupling impedance. All possible machine operating conditions drive towards extremely wide range conditions for the signals that have to be picked up by the BPMs. Low loading effects on the beam and high enough signals for the front-end electronics impose conflicting requirements on the BPMs design task. The extremely wide beam spectrum compared to the narrow portion used by the front-end, finally introduces further EM issues that have to be carefully considered in the BPM design.

To address these issues, this chapter describes the BPM development for a fourth-generation X-ray light source by accurately investigating its EM behavior [43, 41, 21, 6, 48, 20]. A theoretical model of the classical round shape structure is firstly illustrated and then a detailed numerical EM characterization of the more sophisticated rhomboidal geometry (the shape chosen for Elettra 2.0 BPMs) is carried out. An intermediate square geometry is also introduced as a compromise between calculation time and ability to characterize the general behavior of different kind of pick-ups. Different materials and operation conditions are explored in terms of wake potential and beam coupling impedance, transfer impedance, spectrum of the induced signals, trapped and propagating modes, to finally identify a suitable BPM design capable to combine a satisfactory performance with a manageable realizability [27, 32].

The considerations reported in this chapter about the extraction of the signals induced by the electron beam in the pick-ups assume that the corresponding EM energy propagates through 50 Ohm coaxial lines terminated on matched waveguide ports that simulates the behavior of ideal RF connectors. Adding to the EM model even the structure and materials used in real RF connectors would have introduced extra complexity without adding more reliable data from wakefield simulations, but at same time drastically increasing the calculation time. Practical considerations about insertion and return losses support the assumption that, if the quality of the used connectors is "good enough" in the operating frequency bandwidth, the effects introduced by them can be neglected (some considerations on connectors are reported in the next chapter).

4.2 Basic Theoretical Analysis

The structure of a typical button-type BPM with a vacuum pipe of circular-cross-section commonly used in particle accelerators is reported in Figure 4.2a. Four identical round electrodes, also known as electrostatic or capacitive coupled pick-ups (PUs), are located at azimuthally symmetric positions around the longitudinal z-axis of the device, corresponding to the symmetry axis of the cylindrical vacuum pipe.

When an ultra-relativistic axis-symmetric charged particle beam propagates along this axis (centered beam condition), the EM coupling between the beam field and the four PUs results the same for each electrode (Figure 4.2b). In this situation, four identical voltage signals are available at the end of each coaxial line that is feeded by its own PU. Sometimes, instead of the voltage, the power extracted from each coaxial port, usually designed to have a characteristic impedance of 50 Ω, is used as the beam induced quantity to be checked. In both cases, the signals delivered to the BPM ports A, B, C, and D constitute a balanced bridge. Otherwise, when the centered beam condition is not satisfied, the transverse beam position with respect to the z-axis may be evaluated by calculating the differences between the output voltages (or powers) by considering the (A,C) electrode pair for the y displacement and the (B,D) one for the x displacement.

The characteristics of the signals delivered at the four ports can be inferred once the three-dimensional (3D) distribution of the EM field excited in the BPM volume is known. The usually adopted EM BPM model relies on some simplifying hypotheses. Firstly, the BPM body is assumed to be a cylindrically symmetric perfectly conducting structure of virtually infinite length. Secondly, the transverse distribution of the beam charge is assumed azimuthally symmetric with respect to the beam propagation direction, without imposing constraints on the longitudinal beam charge density. Thirdly, the on-axis beam condition is matched (in this work only such kind of excitation is considered). When these three

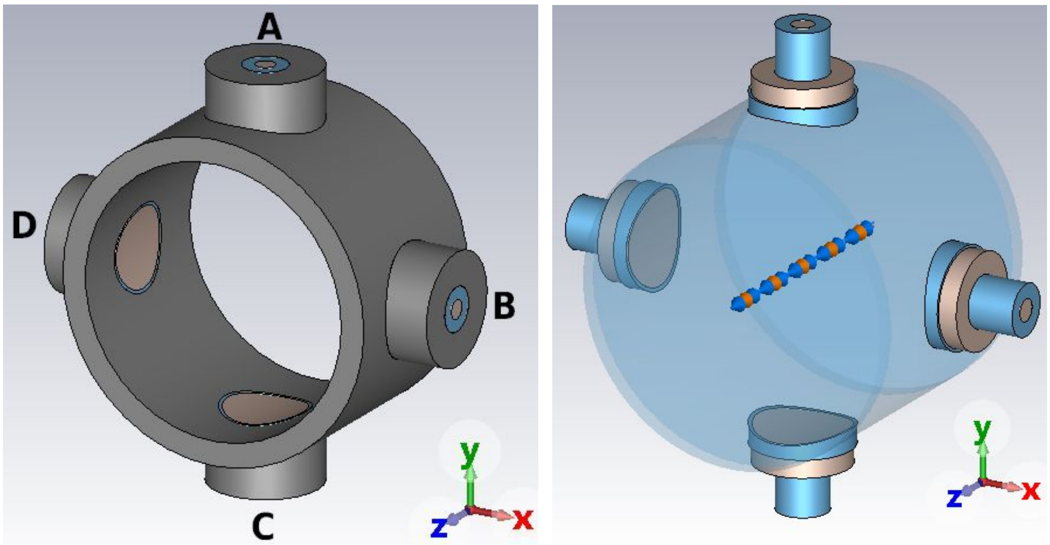

(a) (b)

Fig. 4.2 Round shape BPM structure: (**a**) body assembly, (**b**) EM coupling.

assumptions hold, a pure transverse EM (TEM) field propagates along the BPM, whose electric **E** and magnetic **H** field lines are, respectively, orthogonal (Figure 4.3a) and tangent to the inner surface of the vacuum pipe. This determines the induction, on the inner surface of the vacuum pipe, of an image charge and of a surface current both azimuthally symmetric but having polarity opposite to, respectively, the beam charge and the beam current. During the BPM manufacturing process, the real material is selected to have a relative magnetic permittivity of unity, while its finite electric conductivity is high enough that both the longitudinal electric field component introduced by the ohmic losses on the conducting surfaces and the skin depth penetration of the surface currents do not introduce significant deviations from the ideal TEM mode.

4.2.1 Transfer Impedance and Signal Extraction

Since an opposite-polarity image charge is induced on the surface of each electrode illuminated by the beam (Figure 4.3a), the longitudinal surface charge density profile results proportional to the longitudinal charge profile of the particle beam by a coverage factor. The total induced charge $q_{\text{image}}(t)$ as a function of the time t can then be calculated by integrating the surface charge density distribution over the electrode surface S (Figure 4.3b). This integration may be a very complex task that, if the bunch length is longer than the button radius (narrow band beam), can be approximately estimated assuming as uniform the

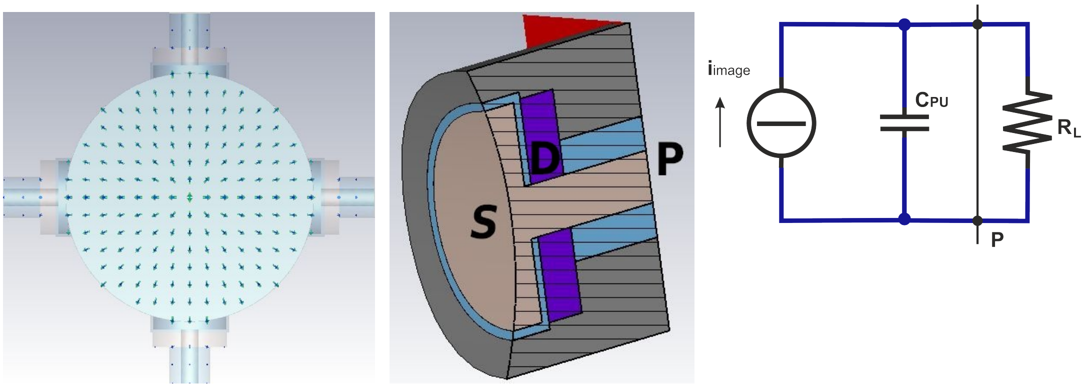

(a) (b) (c)

Fig. 4.3 Round BPM model: (**a**) electric field, (**b**) PU cross-section (S: surface exposed to the beam, D: dielectric, P: signal extraction port), (**c**) equivalent circuit.

longitudinal charge density of the beam over the button length. Under this condition, one obtains:

$$q_{\text{image}}(t) = \rho_L(z-ct)\,\frac{r_{\text{PU}}^2}{2r_{\text{pipe}}} = i_{\text{beam}}(t)\,\frac{r_{\text{PU}}^2}{2c\,r_{\text{pipe}}}, \tag{4.1}$$

where $\rho_L(z-ct)$ is the linear charge density of the particle beam, r_{PU} is the button radius, r_{pipe} is the vacuum pipe radius, $i_{\text{beam}}(t)$ is the beam current, and c is the speed of light in the vacuum. By taking the derivative of Equation 4.1, the current driven by the induced charge can be determined as:

$$i_{\text{image}}(t) = \frac{\mathrm{d}q_{\text{image}}(t)}{\mathrm{d}t} = \frac{r_{\text{PU}}^2}{2c\,r_{\text{pipe}}}\,\frac{\mathrm{d}i_{\text{beam}}(t)}{\mathrm{d}t}. \tag{4.2}$$

If the signal extraction port P (Figure 4.3b) is left open, this current firstly charges and then discharges the button capacitance C_{PU}, and thus the voltage can be calculated as:

$$v_{\text{port}}(t) = \frac{q_{\text{image}}(t)}{C_{\text{PU}}} = \frac{r_{\text{PU}}^2}{2c\,r_{\text{pipe}}C_{\text{PU}}}\,i_{\text{beam}}(t). \tag{4.3}$$

If P is instead terminated on an external load R_L, the equivalent current generator feeds the parallel connection of C_{PU} and R_L, hence producing a voltage drop across R_L (Figure 4.3c). The evaluation of the impulse response corresponding to the $R_L - C_{\text{PU}}$ parallel circuit completes the time domain analysis, since $v_{\text{port}}(t)$ can be calculated by convolution once $i_{\text{beam}}(t)$

is known. This enables to evaluate the PU transfer impedance as:

$$Z_{T_{\mathrm{PU}}}(f) = \frac{V_{\mathrm{port}}(f)}{I_{\mathrm{beam}}(f)} = \frac{r_{\mathrm{PU}}^2}{2c\, r_{\mathrm{pipe}} C_{\mathrm{PU}}} \frac{j2\pi f R_L C_{\mathrm{PU}}}{1 + j2\pi f R_L C_{\mathrm{PU}}}, \tag{4.4}$$

where f is the frequency, $V_{\mathrm{port}}(f)$ and $I_{\mathrm{beam}}(f)$ are the Fourier transforms of the voltage drop and of the beam current, respectively, while $j = \sqrt{-1}$ is the imaginary unit. It is important to note that Equation 4.4 approaches a real constant in the high-frequency range ($f \gg f_{\mathrm{cut}}$) and an imaginary frequency-dependent function in the low-frequency one ($f \ll f_{\mathrm{cut}}$), with:

$$f_{\mathrm{cut}} = \frac{1}{2\pi R_L C_{\mathrm{PU}}}, \tag{4.5}$$

identifying the cutoff frequency. In the direct current (DC) case, that is, when $f = 0$, the PU transfer impedance becomes equal to zero. This result matches the capacitive nature of the coupling between the beam and the electrode surface. Only bunch shapes that have a longitudinal profile that varies over time can be detected, as indicated by Equation 4.4. In practical applications, the analog front-end electronics connected to the four ports of each BPM are designed to operate at a specific centered frequency f_{detect} over a bandwidth Δf. To improve the resulting signal-to-noise ratio, the module of $Z_{T_{\mathrm{PU}}}(f_{\mathrm{detect}})$ should be as high as possible. In this regard, by more deeply examining Equation 4.4, one may note that the parameters influencing this value are, on one hand, r_{pipe} and R_L, which are, however, determined by the design of other accelerator components, and, on the other hand, r_{PU} and C_{PU}, which can instead be used to optimize the PU transfer impedance module.

If the maximum bunch spectrum frequency is low enough, as in the case of long beams, the total PU capacitance can be theoretically calculated by adding all the partial DC contributions due to the different sections that compose the PU itself. Accordingly, one can write:

$$C_{\mathrm{PU}} = C_{\mathrm{gap}} + C_{\mathrm{transition}} + C_{\mathrm{coaxial}} + C_{\mathrm{fringe}}, \tag{4.6}$$

where the four added capacitances C_{gap}, $C_{\mathrm{transition}}$, C_{coaxial}, and C_{fringe} refer, respectively, to the gap between the PU electrode and the housing, to the transition region between the same electrode and the coaxial line feeding port P, to the coaxial line itself, and to the fringe electric field. For simple electrode geometries, such as the cylindrical one used in Figure 4.3b, C_{gap} can be calculated by applying the formula for cylindrical capacitors when the button and gap sizes as well as the characteristics of the dielectric material in which the electric field is stored are all known. The same approach may be adopted to derive C_{coaxial}, while $C_{\mathrm{transition}}$, and even more C_{fringe}, are difficult to estimate because of, respectively, non-uniform and dispersed electric field distributions inside the respective regions. As the bunch length decreases, the bunch spectrum width unavoidably increases and the lumped model that describes the transfer impedance becomes more and more inaccurate, to the point where the estimation of the PU capacitance becomes unfeasible. Due to the complex shape and the material characteristics of the PU, the field theory of guided waves has to be used for the computation of the signals available at the BPM ports. This approach is so complex that, apart from very simple coaxial geometries, the PU high-frequency behavior must be studied by numerical methods [42, 22].

4.2.2 Longitudinal Coupling Impedance and Wake Losses

During the propagation along the BPM axis, the beam is affected by energy losses due to different EM coupling phenomena between the beam itself and its surroundings. Apart from the specific nature of the coupling mechanism, each type of loss can always be modeled by an impedance, that is, by a voltage drop along the beam path scaled to the beam current [46, 35].

Due to the finite conductivity of real conductors, the surface currents induced by the beam give rise to ohmic losses that, in turn, introduce a longitudinal component of the electric field along the inner BPM surface. This effect, known in general as resistive wall, extends over the full beam frequency spectrum (wideband effect), with the corresponding energy loss that can be calculated by the flow of the Poynting vector through the inner BPM surface. The higher the conductivity of the BPM body, the lower the losses due to the resistive wall. As observed in the previous subsection, another factor contributing to the beam energy loss arises from the capacitive coupling. Here, the loading effect on the beam, caused by the extraction of a portion of its energy through each PU, serves as the necessary loss to generate the beam position signal. Assuming a narrow-band beam, the longitudinal beam coupling impedance of each PU is related to its respective transfer impedance by [30]:

$$Z_{\mathrm{L_{PU}}}(f) = \frac{r_{\mathrm{PU}}^2}{2c\, r_{\mathrm{pipe}} R_L C_{\mathrm{PU}}} Z_{\mathrm{T_{PU}}}(f), \tag{4.7}$$

which hence shows the same frequency behavior of the PU transfer impedance. Further beam energy loss contributions arise from the high order modes (HOM) trapped in the gap that isolates the electrode surface from the vacuum pipe. Such HOMs act as narrowband resonators, whose quality factor should be kept as low as possible to reduce localized heating effects. In a real BPM, all the three mentioned losses and their respective impedances simultaneously coexist, with their relative impact varying according to the bunch spectrum. Ideally, a real BPM should limit the losses to only resistive wall and signal extraction contributions. The cumulative effect of all losses may be synthetically summarized by the loss factor:

$$k_{\parallel} = \frac{\Delta U}{(Q_{\mathrm{tot}})^2}, \tag{4.8}$$

in which ΔU denotes the total energy lost by the beam passing through the BPM and Q_{tot} represents the total bunch charge. During the BPM design, $k_{\parallel}$ should be kept as low as possible, but this constraint could severely impair $Z_{\mathrm{T_{PU}}}$ which, to assure enough signal to the RF receivers in any operating condition, should instead be as high as possible. To define an acceptable compromise between such two opposite requirements is a key factor of any beam position monitor design.

4.3 Numerical Analysis

As outlined in the previous section, the lumped nature of the analytical PU model limits its ability to describe the beam-PU coupling mechanism and the PU transfer function in a wideband context. To overcome this limitation, CST Particle Studio Suite [15] is adopted as a fully 3D numerical tool for modeling the EM field propagation inside the vacuum pipe and the PU.

The CST wakefield solver, in particular, is used to simulate the time domain (TD) EM behavior of a BPM device when excited by a relativistic beam. The simulation settings are selected as follows.

- The bunch shape is represented by a Gaussian distribution characterized by a standard deviation σ_{rms}, expressed in length unit (mm), and by a total charge Q_{tot}, identified by the area under the Gaussian distribution curve. In the presented simulations, this latter parameter is fixed to 1 nC, while different σ_{rms} values ranging from 3 to 10 mm are considered. With reference to the shapes reported in Figure 4.4a, the vertical axis unit represents the linear charge density in C/m. Taking into account the propagation characteristics of the charged bunch at the speed of light, the horizontal axis can be rescaled in time unit (ns), and the vertical axis in electric current unit (C/s). The TD representation of the Gaussian distributions is shown in Figure 4.4b, while the corresponding spectra, obtained by the Fourier transformation, are reported in Figure 4.4c. Concerning the adopted materials, all of them are realistically characterized by a lossy behavior and a relative magnetic permeability $\mu_{\mathrm{r}} = 1$. In particular, stainless steel AISI316L with electric conductivity $\sigma_{\mathrm{body}} = 1.35$ MS/m is chosen for the BPM body, while molybdenum with electric conductivity $\sigma_{\mathrm{button}} = 18.2$ MS/m is selected for the central pin and the PU button. The vacuum sealing D (Figure 4.3b) is modeled by a

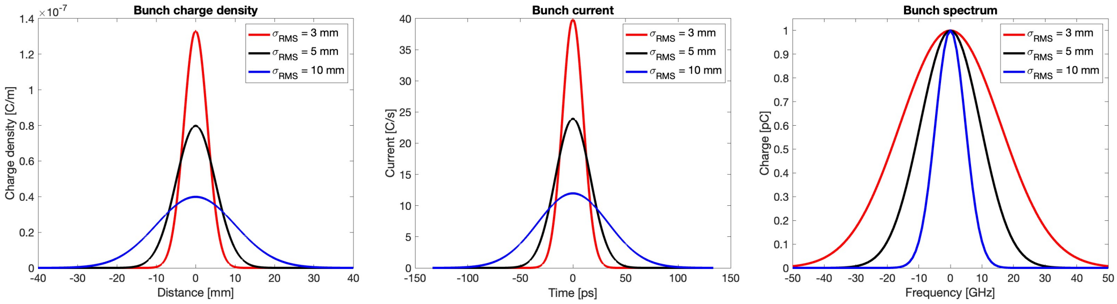

(a) (b) (c)

Fig. 4.4 Gaussian bunches used in CST: (**a**) longitudinal charge density, (**b**) bunch current, (**c**) bunch spectrum.

dielectric material with relative electric permittivity ε_r, whose value ranges from 1 to 10.

- Regarding the simulator configuration, the beam input and output cross-sections of the vacuum pipe are set as open boundaries to emulate an infinitely long vacuum pipe, in order to avoid perturbations of the incoming and outgoing quantities. The signal propagating along the coaxial feedthrough of the PU is terminated on a 50 Ω matched waveguide port. Additionally, only one fourth of the BPM structure is required to be actually simulated by the CST wake solver, thanks to the on-axis beam excitation and the symmetry of the component. The mesh density is always set fine enough to properly cover the gap between the button and its housing.

According to these settings, the following subsections numerically investigate progressively more complex geometries by moving from the typical round BPM structure theoretically characterized in the previous section. In particular, the limitations of the basic analytical model are firstly addressed, while rhomboidal vacuum pipes are subsequently studied in comparison to the round chamber.

4.3.1 Round Pipe with Cylindrical PUs

The wake potential, transfer impedance, output signal voltage, and spectrum for the round BPM are shown in Figure 4.5, which is obtained by considering three different bunch lengths ($\sigma_{\rm rms} = 3, 5, 10$ mm). In particular, these curves are derived by adopting alumina 99.5% for the vacuum sealing material ($\varepsilon_r = 9.9$) and limiting the wake length to one meter in order to keep as short as possible but still meaningful for the numerical evaluation. The reliability of this latter choice is confirmed by the 80 dB decrease in the field energy over time achieved at the end of the simulation.

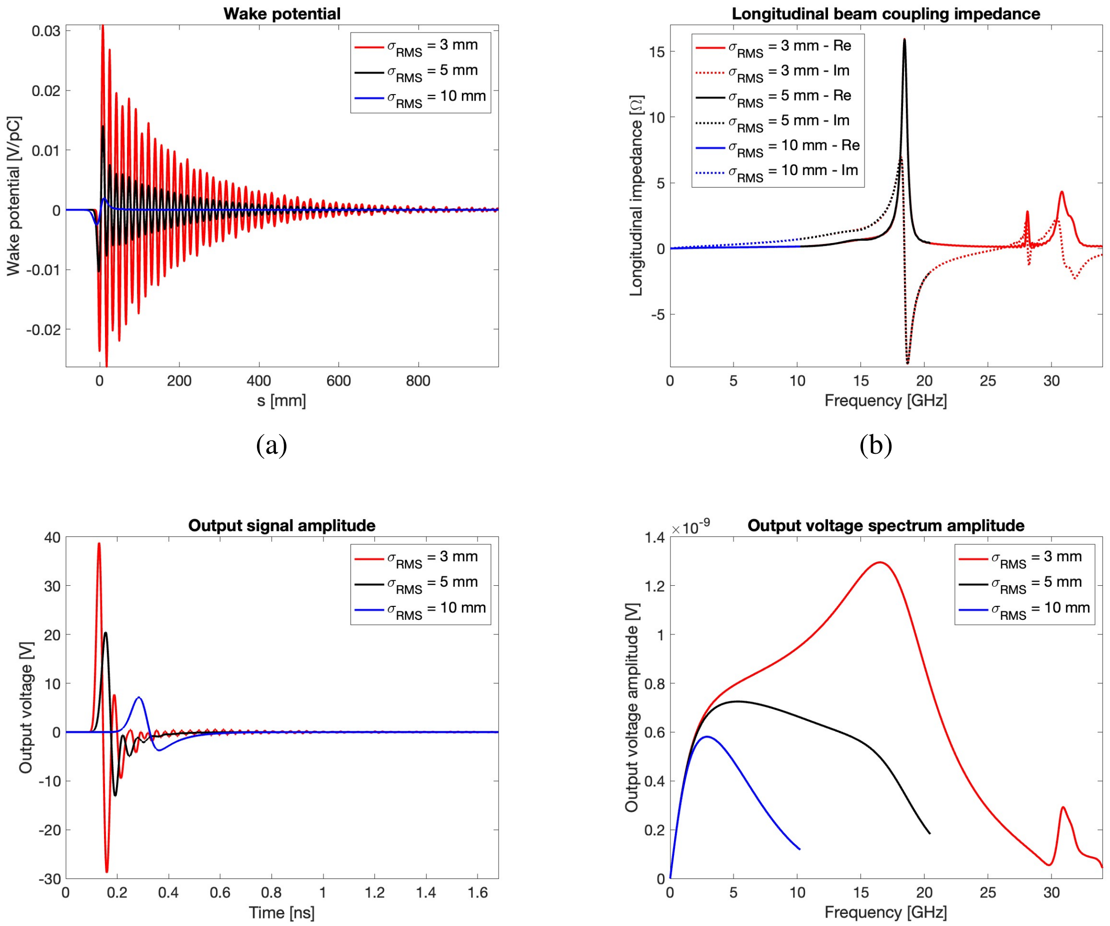

(a) (b)

(c) (d)

Fig. 4.5 Round BPM case: wake potential (**a**), longitudinal beam coupling impedance (**b**), output signal voltage (**c**), and spectrum (**d**) for $\varepsilon_r = 9.9$ and different σ_{rms} values.

This first set of results shows that the shorter the bunch length, the higher the wake potential, its time duration, and the energy lost by the beam in the BPM structure. Note that, as the bunch length decreases, the corresponding beam coupling impedance plot covers, as expected, the calculated curves for longer bunches, while trapped modes not excited by long bunches appear as resonance peaks when the bunch spectrum increases. Additionally, the figure reveals that the output signal strength increases as the bunch length decreases, a behavior that could lead to very high electric fields inside the button gap in the case of short bunches.

A second set of simulations is carried out by fixing the bunch length to $\sigma_{\mathrm{rms}} = 3$ mm and considering, for the vacuum sealing material D, three different values of the relative dielectric permittivity $\varepsilon_r = 1, 6.7, 9.9$. The derived curves are shown in Figure 4.6, which still reports the wake potentials, the transfer impedances, the output signal voltages, and their spectra. These results show how the beam coupling impedance resonant peak due to the first trapped mode shifts toward lower frequencies when ε_r increases, as expected in terms of dielectric spectroscopy. Furthermore, the output signal shows a growing ringing due to reflections induced by the impedance mismatch along the PU extraction signal path.

In order to compare the transfer impedance calculated by the theoretical model with the one obtained by the numerical solver, the C_PU value must be estimated. To overcome the difficulties discussed at the end of section 4.2.1 concerning the analytical derivation of this latter parameter, a set of electrostatic simulations has been carried out by adopting the CST electrostatic solver and varying the permittivity of the sealing material used in the PU. The obtained C_PU values are 1.11 pF, 1.61 pF, and 1.80 pF for $\varepsilon_\mathrm{r} = 1, 6.7$, and 9.9, respectively. The corresponding f_cut are 2.87 GHz, 1.97 GHz, and 1.77 GHz. Figure 4.7 shows the comparison between the analytical (dotted lines) and numerical (solid lines) curves of the transfer impedance modulus for $\sigma_\mathrm{rms} = 3$ mm. For $f \ll f_\mathrm{cut}$, the two models match very well. Due to the totally different approach between the two methods, the computational cost of the theoretical calculation is negligible compared to that of the numerical solver.

4.3.2 Square/Rhomboidal Pipes with Conical PUs

While the round pipe is often employed in many of the operating particle accelerators, alternative geometries relying on a rhomboidal structure have been adopted in other machines, such as Elettra and Elettra 2.0 storage rings [26]. Ther are two main reasons for this choice.

The first reason is related to the manufacturing process, since a BPM body consisting of flat surfaces allows a simpler hosting of the buttons, without the need of leaving non-uniform gaps between the inner surface of the vacuum chamber and the buttons, a geometric configuration that might trigger undesired EM effects.

The second, and more relevant reason, concerns the constraints imposed by other critical devices, such as magnetic element fitting, or other design considerations, such as X-ray-induced thermal loading effects. Regardless of the specific reason that imposes a non-circular vacuum pipe, the farther the BPM from a circular shape, the lower the reliability of the analytical model because of the lack of uniformity in the distribution of the induced surface charge and current. In this case, despite its higher computation cost, the numerical calculation method should always be used even if a raw estimation of the BPM transfer impedance is required. If the effective geometry of the BPM device can be, at a first evaluation, substituted by a purely square cross-section aligned with the coordinate planes, a more effective mesh coverage can be obtained by the CST wake field solver. This choice allows shorter calculation times for the preliminary investigation of the transfer impedances for different types of PU. To deepen this aspect, let us compare the round BPM with $r_\mathrm{pipe} = 8.5$ mm (Figure 4.2b) and

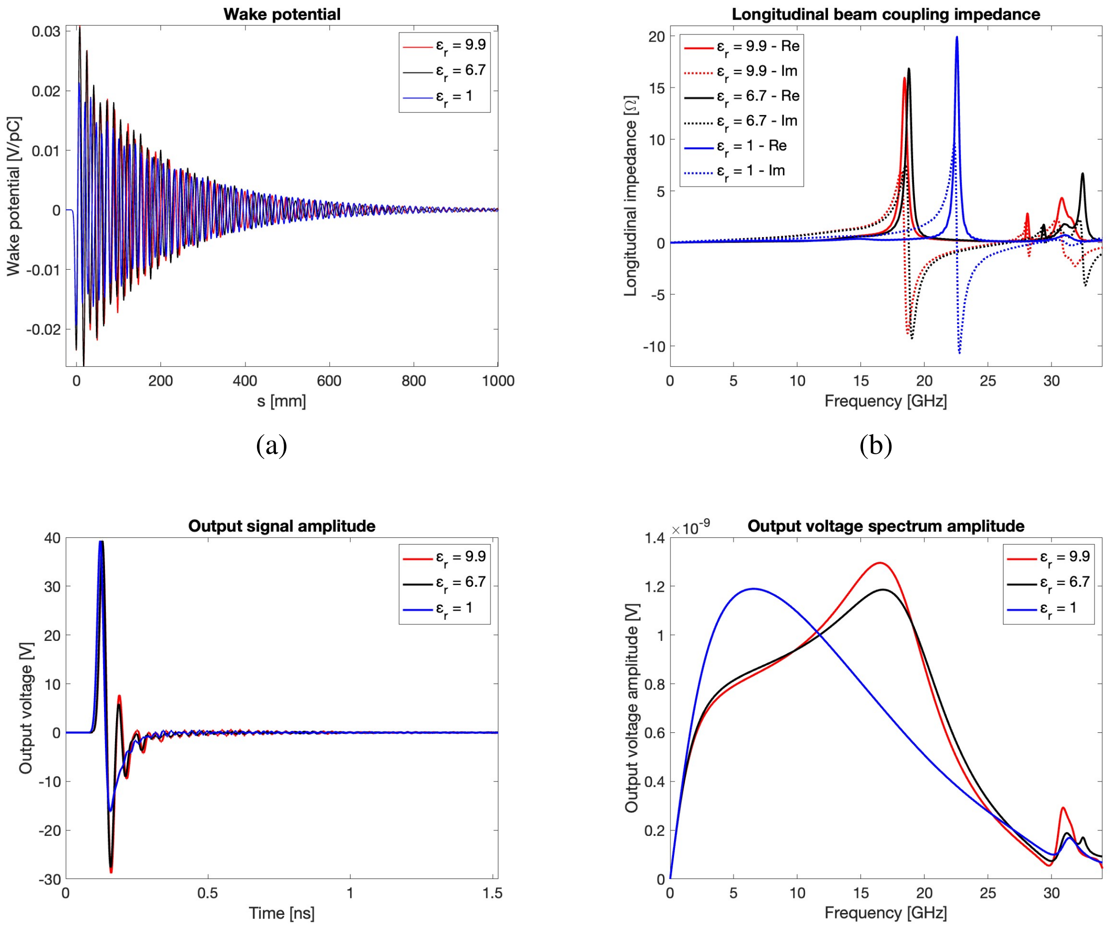

(a) (b)

(c) (d)

Fig. 4.6 Round BPM case: wake potential (**a**), longitudinal beam coupling impedance (**b**), output signal voltage (**c**), and spectrum (**d**) for $\sigma_{\mathrm{rms}} = 3$ mm and different ε_r values.

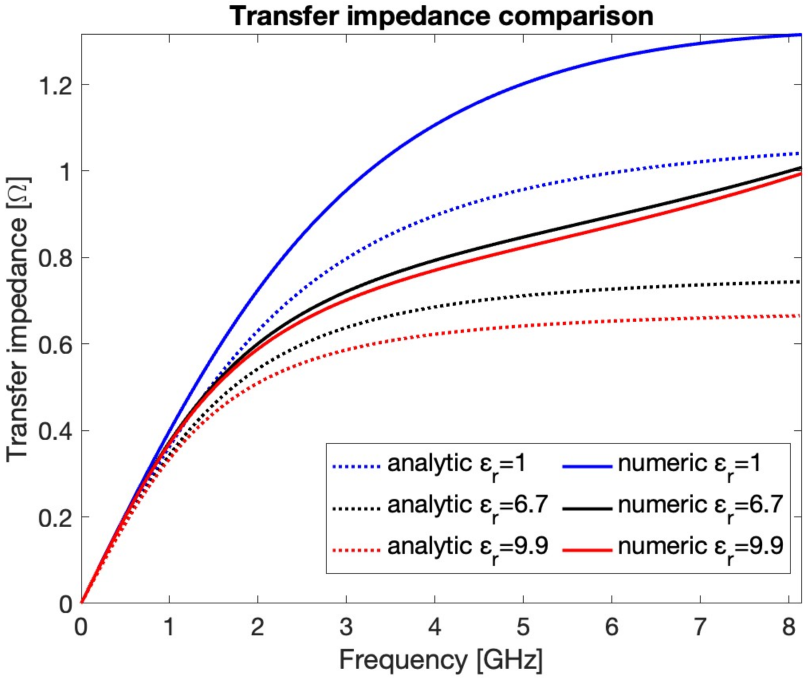

Fig. 4.7 Analytical and numerical transfer impedance modulus for $\sigma_{\mathrm{rms}} = 3$ mm and different ε_{r} values.

the square one with edge equal to 16 mm (Figure 4.8a), assuming $\sigma_{\mathrm{rms}} = 3$ mm. The PU geometry is maintained cylindrical with sealing material having $\varepsilon_{\mathrm{r}} = 9.9$. The outcome of this comparison is presented in Figure 4.8c for the output voltages, in Figure 4.8d for the corresponding voltage spectrum, and in Figure 4.8b for the beam-coupling impedance.

These figures reveal a good agreement between the respective performance figures corresponding to the two structures, further showing that the highest contribution to the wake impedance is due to the non-propagating modes inside each of the four PUs. This implies that, between the two compared geometries, it might be preferable to select the one that guarantees a minor confinement of the higher order modes within the BPM body.

Beside alternative shapes for the vacuum chamber, accelerator physicists and engineers are also exploring non-cylindrical geometries for the electrode of the PU [7, 18, 3, 4, 13], with the purpose of matching the recent trend aimed to shift towards ever higher frequencies the peak of the real part of the wake impedance. The results reported in the literature suggest that the conical shape is a good compromise between practical manufacturability and high frequency performance. However, similarly to the cylindrical shape, the impedance matching between the conical, transition, and coaxial PU sections strongly affects the PU energy reflection back into the vacuum pipe. Figure 4.9 shows, for $\sigma_{\mathrm{rms}} = 3$ mm and still considering a wake length limited to one meter, some of the PU geometries that have been

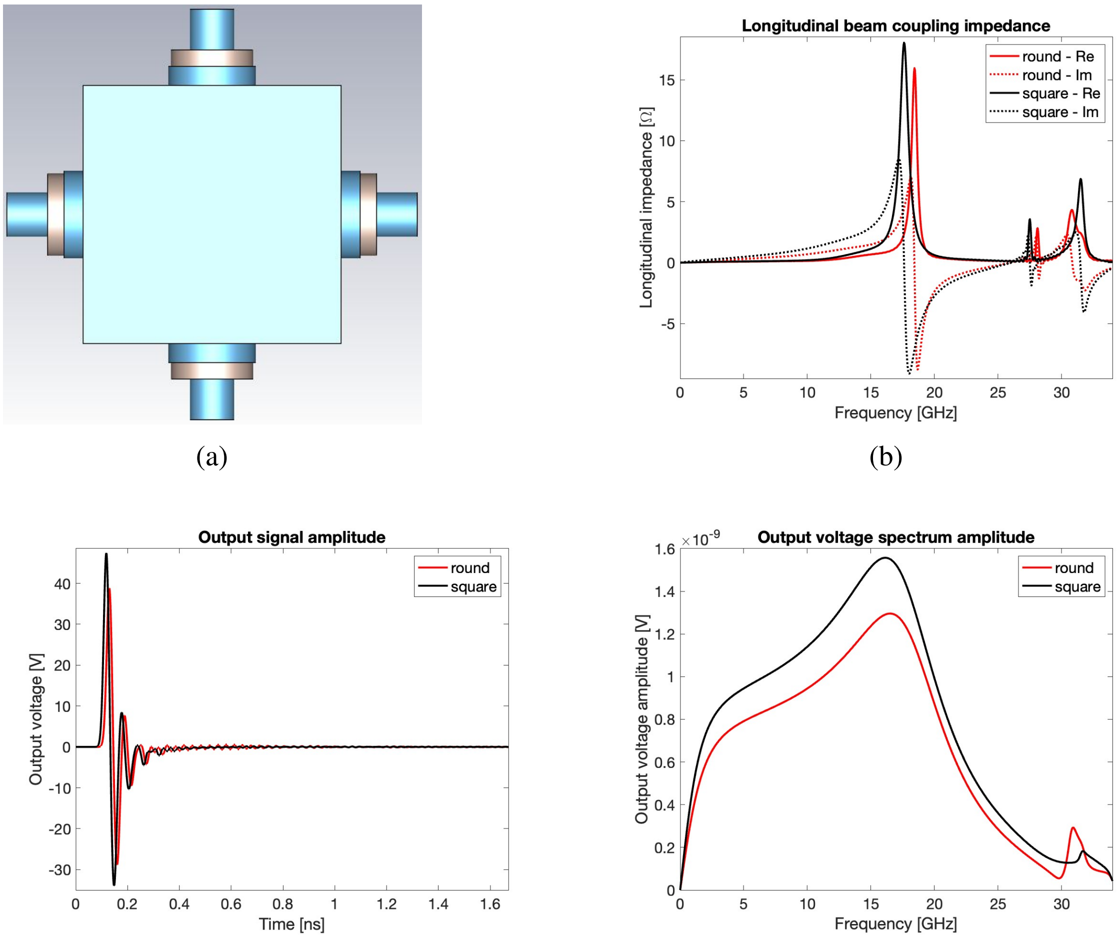

(a) (b)

(c) (d)

Fig. 4.8 Comparison between round and square geometries for $\sigma_{\mathrm{rms}} = 3$ mm: (**a**) square BPM model, (**b**) longitudinal beam coupling impedance , (**c**) output signal voltage, and (**d**) spectrum.

Table 4.1 Loss factor for the PUs in Figure 4.9

	PU1	**PU2**	**PU3**	**PU4**
ε_r	6.7	4.1	6.7	6.7
$k_{\parallel}$ [mV/pC]	4.40	3.90	5.06	4.67

investigated to find the best candidate to be used in Elettra 2.0. Each geometry is chosen based on the dielectric material employed, as illustrated by the different colours in the figure. According to the classical formula for the characteristic impedance of the coaxial transmission lines, the coaxial section of the PUs have the ratio between the radii of the facing conductors equal to 2.3 to match the 50 Ω in air. The parameters used to compare the PUs are the loss factor $k_{\parallel}$, the ringing over time of the PU output signal, its spectrum, the time duration of the wake potential, and the beam coupling impedance. Due to the effect of the energy stored in the dielectric material used for the vacuum sealing, none of the PUs simulated has been able to fade the wake potential within 2 ns, that is, the RF period of most synchrotrons. The losses are indicated in Table 4.1. All the PUs having a loss factor greater than 5 mV/pC have been excluded from further investigations. The remaining PUs were compared to find the best compromise between transfer impedance and beam coupling impedance. PU2 and PU4, have been finally selected as possible candidates for real applications based on different types of vacuum sealing insulators.

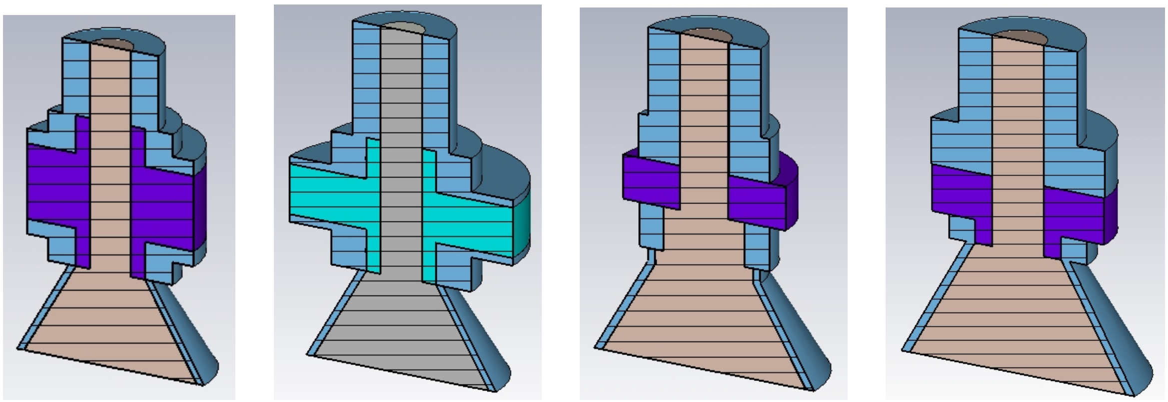
(a) (b) (c) (d)

Fig. 4.9 Compared PU shapes: (**a**) PU1, (**b**) PU2, (**c**) PU3, (**d**) PU4.

Once the suitable PU shapes are selected, the final part of the numerical analysis has been done using the actual geometry of the vacuum chamber. As outlined at the beginning of this subsection and according to the decision taken for Elettra, even the fourth-generation Elettra 2.0 machine will have a rhomboidal BPM pipe, with a geometric scaling factor about three

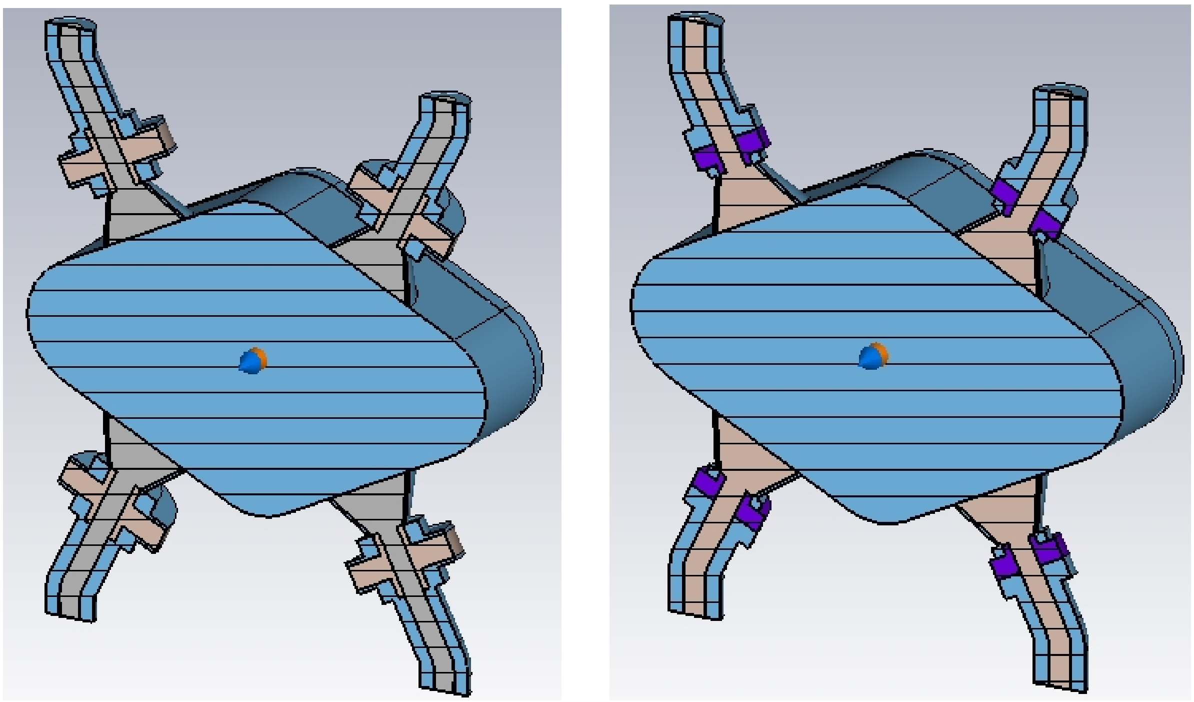

(a) (b)

Fig. 4.10 Rhomboidal BPM models based on PU2 (**a**) and PU4 (**b**).

times smaller. The simulated BPMs based on PU2 and PU4 are reported in Figure 4.10, while the resulting wake potential, transfer impedance, output signal voltage, and spectrum are illustrated in Figure 4.11 ($\sigma_{\mathrm{rms}} = 3$ mm). The dotted line shown in Figure 4.11d, representing the bunch spectrum rescaled to fit the vertical axis span, has been added in order to check the bandwidth overlapping of the PU signals with the one of the exciting beam.

4.4 Conclusions

In this chapter, a detailed analysis of BPM design has been presented from a theoretical point of view. The analytical model provides valuable insight into the key parameters that influence the longitudinal beam-coupling impedance and the transfer impedance, particularly in the case of long bunches and impedance-matched pickups. As the bunch length becomes shorter, the circuit-theory framework employed in the analytical model must be superseded by electromagnetic field theory, which properly captures energy-propagation phenomena. Given the complexity of the interaction between a bunch of charged particles and the BPM structure, numerical methods are indispensable for evaluating the beam-coupling impedance and the signals extracted from the pickup. Another great advantage of the numerical simulation is

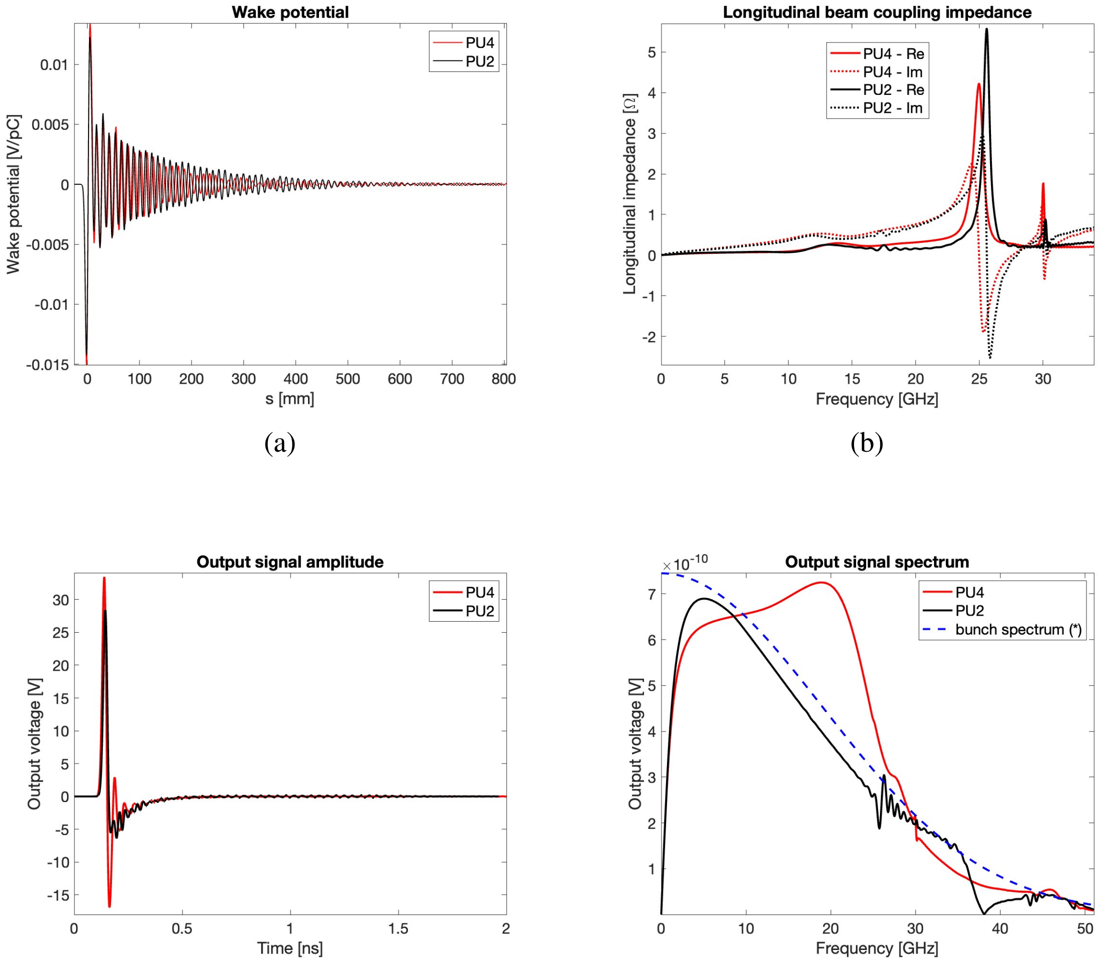

(a) (b)

(c) (d)

Fig. 4.11 Rhomboidal BPM case: wake potential (**a**), longitudinal beam coupling impedance (**b**), output signal voltage (**c**), and spectrum (**d**) for $\sigma_{\mathrm{rms}} = 3$ mm. (*): arbitrary unit.

that it can take into account any kind of geometry of vacuum pipe and pickup. This approach is subject to limitations stemming from the mesh density needed to discretize the simulated volume with adequate resolution to guarantee convergence. According to the need to shift the peaks of the beam-coupling impedance as high in frequency as possible, the pickup design foreseen for Elettra 2.0 adopts a conical geometry of the button exposed to the beam. To reduce the computation time associated with evaluating various pickup geometries based on conical button, a square BPM body shape was adopted. Its comparison with the conventional cylindrical BPM body demonstrates that the resulting quantities are consistent, confirming that the simplified square geometry provides a reliable approximation. Following extensive simulations exploring different pickup shapes and dielectric materials, two geometries have been selected as references for fabrication.

Chapter 5

BPM: from theory to real devices

5.1 Introduction

The numerical simulations reported in the previous chapter allowed to investigate the electromagnetic behavior of different pick up designs when excited by an ultra relativistic beam. Different possible combinations of shapes and materials for the manufacturing have been identified, suggesting that low ε_R insulating materials are preferable. About the magnetic characteristics, the choice $\mu_R = 1$ is mandatory to avoid theintroduction of distortions in the magnetic flux distribution generated by the magnets of the machine lattice.
Starting from the PU4 and PU2 shapes, a practical feasibility study was conducted by contacting well-known button type pickup suppliers. Apart from the specific details connected to each supplier technological process, the common indication was that the PU2 like shapes would have been too complex to be manufactured at an acceptable price, if not at all, and for this reason any further development of such kind of pick up was abandoned in favor of the PU4 like shapes. Another critical issue highlighted during the meetings with potential manufacturers was the quite long realization time even for a small number, approximately 20, of pick up samples, mainly due to materials procurement. Such long delivery time suggested to try to develop in house batches of prototypes intended to validate the numerical simulations both in laboratory, using dedicated microwave test benches, and as far as possible in real operating conditions using relativistic electron beams. In order to gain experience in pick-up manufacturing and characterization, four types of home made pickups, from now on indicated as generations, have been in house machined and assembled following an incremental manufacturing complexity approach. The main differences between such home made pick ups and the "commercial" ones consist basically in the materials and corresponding technologies used for vacuum sealing, electric insulation and central pin-button realization. Once a generation has been proven reliable in real applications, the next generation has been

designed and manufactured to overcome the limitations of its predecessor [12]. The evolution of the pick-ups from a generation to the other has been followed by a corresponding evolution of the test benches aimed to cover the increasingly wider frequency band required to assess in a repeatable manner the expected performance of the home made devices. Once validated, the pick ups can be grouped by four based on their similarity, ideally they should behave all the same, in order to be mounted on a single BPM body to obtain a balanced BPM device. If, for any reason, a not validated pick up were mounted, it could injury the quality of the full BPM assembly.

5.2 RF connectors

As already mentioned in the introduction of the previous chapter, in wakefield simulations the RF connectors were approximated as matched ports over the full excitation signal spectrum. Such approximation is acceptable if the type of connector to be embedded in the pick up has enough bandwidth with respect to the maximum operating frequency of the signal induced by the beam in all possible machine operating conditions. This means that the connector's return and insertion losses are low enough that can be neglected, and that high order propagating modes are not excited by the connector itself. In this case,the connector is supposed able to extract any beam induced signal without perturbing the EM propagation characteristic of the pick up. To match the connector propagation characteristic to the one of the pick up over the full beam spectrum could seem an excessive requirement compared to the working bandwidth of the detectors in charge of monitoring the beam induced signals (for Elettra 2.0 the central frequency of the position monitor front-ends is 500 MHz, with 6 MHz wide pass-band filtering), but it is theoretically justified in order to avoid reflections once the energy extracted from the beam is propagating outside the pick up. In the extreme cases of fully unmatched pick up, such when it or the coaxial line that it feeds is left open or shorted, a portion of the beam extracted energy is reflected back in the vacuum pipe, giving an extra contribution to the wake field effects, not to mention the risk of electric discharge due to high VSWR (Voltage Standing Wave Ratio). Of course open and shorted pick up configurations are not planned working conditions, but they could represent real situations in case of not full bandwidth matched connections and terminations.

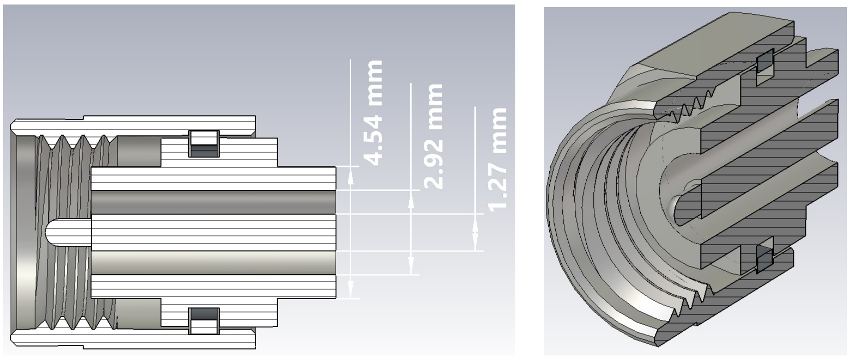

(a) (b)

Fig. 5.1 SMK connector (pin contact): (**a**) cross section, (**b**) 3D cut view.

5.2.1 Coaxial connector for the Elettra 2.0 pick ups

Among the different types of coaxial connectors available on the market whose geometry and materials are specified by dedicated standard (see, for example, MIL-STD-348B [2]), the best candidate to be used for Elettra 2.0 is the SMK connector (pin contact), also known as both 2.92 mm connector and K connector (because it covers the K band frequencies). Its shape is shown in Figure 5.1.

The standard N connector, initially considered as a possible candidate, has been discarded for its mechanical size and limited bandwidth.

Introduced in the mid-1970s, the most interesting features of the SMK connector are:

- it is mechanically rugged;
- its size is compatible with the available room on the top of the pick up and between the components, such as magnets and flanges, in the middle of which the BPMs have to be mounted;
- the connection between it and its counter part on the coaxial cable is made by screwing;
- no dielectric apart from air or vacuum is used, that assures long time compatibility with the level of radiation foreseen for Elettra 2.0;
- it has 50 Ω impedance;
- its maximum rated operating frequency in air (and vacuum) is 40 GHz;
- its first high order mode TE_{11} cutoff frequency is about 45.6 GHz;
- it is compatible (inter-mateability) [37] with SMA and 3.5 mm standard connectors;

In order to further improve its quality, the SMK connector could be manufactured according to the precision coaxial 2.92 mm connector specifications, as defined in IEEE 287 standard (DC to 110 GHz) [1] for precision electrical measurements, that, although compatible with the MIL-STD-348B standard, imposes much stricter manufacturing tolerances that could make extremely difficult and expensive the practical realization of the pick up.
As a final remark about connectors, although a SMK connector can be mated with a standard SMA connector, the maximum operating frequency of the connection bandwidth is always the lower between the maximum operating frequencies of the unmated connectors, that is the one of the SMA connector. In case of measurements performed at frequencies over the maximum allowed bandwidth of the used connectors, unforeseen effects could appear, such as reflection or absorption peaks not present in simulations. Several physical phenomenons could explain these peaks, the most common of which are due to impedance mismatch, high order modes propagation, geometric resonances, energy emission and/or dielectric resonance/dissipation. In particular cases, if required,the connector behavior out of the frequency range could be evaluated if its exact geometry and the conductivity, ε_r and μ_r (complex) values of the used materials are known up to the maximum frequency used in the simulations. If poor quality or damaged connectors are used, unforeseen artifacts can appear even in their nominal operative range, making almost impossible any kind of reliable signal acquisition (and getting crazy in debug attempts).

5.2.2 Coaxial line - connector matching

In order to clarify the rationale behind the sizing of the Elettra 2.0 pick ups, it is essential to consider the fundamental propagation mode of electromagnetic energy in uniform circular coaxial lines, also known as Transverse ElectroMagnetic (TEM) mode. Assuming lossless the EM field propagation, that means that both conducting and dielectric/magnetic materials are not dissipative, the characteristic impedance of the TEM mode is expressed by the well known formula (expressed in SI units):

$$Z_0 = \frac{138}{\sqrt{\varepsilon_r \mu_r}} \log_{10}\left(\frac{D}{d}\right) [\Omega] \tag{5.1}$$

where D is the inner diameter of the outer conductor and d is the outer diameter of the inner conductor. When the EM energy propagates in air or vacuum ε_r = 1 and μ_r = 1, the ratio between the diameters is set equal to 2.3 in order to have Z_0 equal to 50 Ω. In the case of the SMK connector, $D = 2.92$ mm, $d = 1.27$ mm, and the ratio $D/d = 2.3$. To allow undisturbed TEM propagation from the connector to the line and vice versa, the same characteristic impedance Z_0 and the same cross section are required for the connector and the line. This means that in the case of the coaxial line, in vacuum or filled by air, that feeds the SMK connector the diameters will be respectively $D = 2.92$ mm and $d = 1.27$ mm. For this reason the inner diameter of the outer conductor and the outer diameter of the inner conductor of the uniform circular part of the Elettra 2.0 pick ups have been chosen according to SMK connector corresponding diameters. In order to speed up the manufacturing of the home made prototypes, and only for the samples, the nominal diameters have been modified to $D = 3$ mm and $d = 1.3$ mm, maintaining the D/d ratio equal to 2.3.

5.3 General non electric tests and measurements on PU

Before being assembled onto a BPM body, each PU has to be inspected to assess several parameters involved in chemical, mechanical, vacuum, thermal and electromagnetic specifications. Each of these aspects has a direct impact on the final quality of each pick up, and all of them must be checked, as summarized in the following sub sections.

5.3.1 Chemical tests

These tests are performed to check the exact composition of materials used for the different parts of the pick-ups. Typical examples are the validation of the composition of the steel parts that must be connected together by welding, such as the ones made of AISI316l, and the evaluation of the content of materials subjects to activation if shot by X rays or high energy particles, such as Cobalt.

5.3.2 Mechanical tests

Such kind of tests are performed to check that the pick up characteristic dimensions and angles are within defined tolerance intervals. Manufacturing or assembling errors, out of the required tolerance, can bring to not usable pick up. Typical measurements carried out are:

- coaxiality between the inner conductor and the pick up body;
- alignment between the pick up body and the surface exposed to the beam in terms of intrusion or protrusion in the vacuum pipe;
- uniformity of the pick up gap;
- interference fit between the pick-up and the BPM body;

5.3.3 Vacuum tests

Particle accelerators operate under UHV (ultra high vacuum) conditions, that are assured both using materials with low degassing capabilities, and adopting low permeability sealing mechanism. In the specific case of the pick ups, the materials used for their manufacturing have been carefully chosen to be vacuum compatible by their nature, but the technological processes involved in the pick up assembly, in particular the adhesion between the insulator and conductors, must be UHV tested. If the leak rate measured by Helium is too high, greather than $1 \cdot 10^{-10} \frac{mbar \cdot liter}{second}$, the pick up has to be disregarded and marked as faulty.

5.4 Electric tests and measurements on pickups

Electric tests are dedicated to the measurement of both DC (direct current) and RF (radio frequency) characteristics of the pick ups, according to the principle that if the manufacturing, assembling and sealing processes are repeatable within the target tolerances, each pick up behaves according to design specification with minimal dispersion. If the pick ups behave electrically all the same but the measured parameters are shifted with respect to the simulated ones, this could indicate a systematic error in some point of the production processes.

5.4.1 DC tests

DC tests are aimed to characterize the static behavior of the pick up under test in order to detect extreme conditions such as:

- short circuit, using a simple multimeter;
- insufficient insulation, lower than 50 $G\Omega$, using a megaohm meter;

If any of these tests is not passed, the pick up is discarded and marked as faulty.
DC capacitance measurements have been excluded a priori due to the low capacitance range of the expected values, around 2 pF, that makes extremely tricky to define a meaningful test configuration.

5.4.2 RF tests

The behavior of any kind of button type pick-up can be fully characterized by reflection and transmission measurements performed under test reference conditions, using time domain (TD) or frequency domain (FD) signal processing methods.

Reflection measurements

Reflection measurements are executed injecting a test signal in the pick up through its coaxial connector and measuring the reflected back signal amplitude and phase, in case of sinusoidal excitation (FD), or amplitude and time of arrival, in case of pulsed excitation (TD). The other side of the pick up, the one to be exposed to the beam, is left open in air, acting as an emitting antenna. The drawbacks of such an approach are both practical and theoretical:

- the emitting characteristics of an antenna open in air (EM energy propagation) are influenced by air conditions;
- the antenna captures external EM disturbances that induce unwanted signals along the propagation path of the test signal;
- the radiation boundary conditions used in simulations could not match the real EM energy propagation conditions present during measurements.

Due to these drawbacks:

- the comparison between the theoretically calculated reflection data in simulated open air conditions, and the ones got by measurements in real open air conditions could be very difficult;
- the measurements performed on the same device in different times and/or locations could show significative differences.

For these reasons open in air reflection measurements have been performed only to approximately compare the real behavior of one pick up to the other in the context of the same generation.

Transmission and reflection measurements

Transmission measurements can not be directly executed because the beam port of the pick up (in the context of microwave devices the term port indicates an aperture that allows EM energy to enter/exit the device) is not intended to be directly connected to measuring devices. For this reason a dedicated metallic adapter, indicated as test fixture, is required to create a completely closed propagation path that, starting from the RF connector (RF port) of the pick up, passes through the beam port and terminates on one or more 50 Ohm matched test connectors. Once such propagation path has been physically realized, transmission measurements are executed injecting a test signal in the pick up through its coaxial connector and measuring the amplitude and phase (FD) or amplitude and time of arrival (TD) of the signals detected on the test fixture's connectors. Injecting the test signal through a fixture port the flow of the EM energy that propagates through the pick up can be reversed, allowing bi-directional transmission measurements. The main advantages of using metallic test fixture are that:

- the beam port propagation characteristics are defined by the test fixture design (geometry and materials);
- the effect due to the air conditions on the signal propagation inside the test fixture can be rendered practically negligible reducing the air volume present inside the test fixture. If necessary the test fixture could be designed to be vacuum proof, but this imply to deal with complex and expensive manufacturing processes and vacuum compliant materials;
- the external disturbance are almost totally shielded thanks to the high conductive nature of the test fixture external walls. Only static magnetic field could be still present, but its effect is negligible because all the materials used in pick up and test fixture fabrication have $\mu_R = 1$;
- even reflection measurements can be readily performed in completely repeatable conditions;
- both transmission and reflection measurements can be compared to the corresponding simulations because radiation boundaries are not used.

For these reasons all transmission and reflection practical measurements aimed to validate the design of each pick up generation have been carried out with the support of a set of dedicated test fixtures, whose general characteristics are described in the next paragraph.

5.4.3 Test fixtures: general description

The common requirement that each type of test fixture has to satisfy, regardless the number of its ports, its size and the generation of pick up it is designed to host, is that it must assure a reliable, repeatable and simple to be EM simulated test environment accessible only through the text fixture's connectors and the pick up connector. To obtain such goal:

- the mechanical connection between the pick up beam port and the corresponding port (not connector) of the test fixture must be carefully designed and machined in order to assure that the simulated geometry of the surfaces in contact corresponds to the real one. If this assumption is not true, for example because of mechanical mismatch, excessive surface roughness or dirt trapped, unpredictable artifacts could appear in the measured data due to the perturbation of the surface currents that flow along the mechanical connection;

- test fixture connectors must be machined, assembled and mounted following the same indications of the previous point, otherwise unpredictable artifacts could appear;
- the general machining tolerances of the inner parts of the test fixture have to be adequate to the maximum operative frequency foreseen for the test fixture;
- the maximum operative frequency of the test fixture must be not greater than the maximum rated frequency of its connectors;

The simplest type of test fixture, indicated as "2PTF", is based on a two ports, single SMK connector configuration, see Figure 5.2.

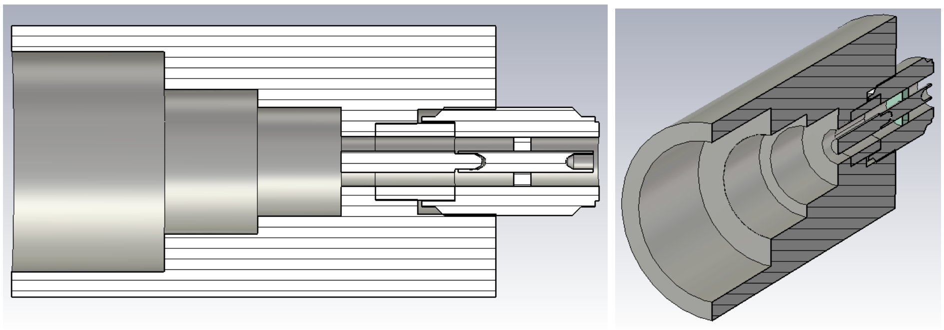
(a) (b)

Fig. 5.2 Two ports test fixture (2PTF): (**a**) cut view, (**b**) 3D cut view.

A short antenna, that couples with the beam port of the pick up, is directly mounted on the central conductor of the test fixture's SMK connector (plug type). The short antenna is aligned along the rotational symmetry axis of the test fixture. When the pick up under test is mounted on the test fixture, the rotational symmetry axis of the pick up aligns with the one of the text fixture. The resulting assembly has two 50 Ω nominal characteristic impedance SMK connectors, the one of the test fixture and the one of the pick up. Thanks to the availability of these SMK connectors, the full 2×2 scattering matrix of the assembly can be measured by a two ports VNA (vector network analyzer) in FD. The same characterization can be obtained by a two ports TDR (Time Domain Reflectometer) that, acquiring transmission and reflection coefficients in TD, is then able to post process them to obtain the scattering matrix in FD. Measures up to 40 GHz have been carried out, that is the maximum rated frequency of the SMK connectors. This test fixture has been used to characterize the RF behavior of the third

and fourth generation of home made pick ups. It has also been used to validate the first batch of 16 prototypes of Elettra 2.0 pick ups, as described in the next chapter.
The main limitation of the 2PTF test fixture is that it can not measure any kind of transfer impedance. To do that, an extra port has to be added to the test setup, as made for the "3PTF" type test fixture, see Figure 5.3. This kind of device has been already used by PSI to measure and sort the button BPM for SLS 2.0 [29].

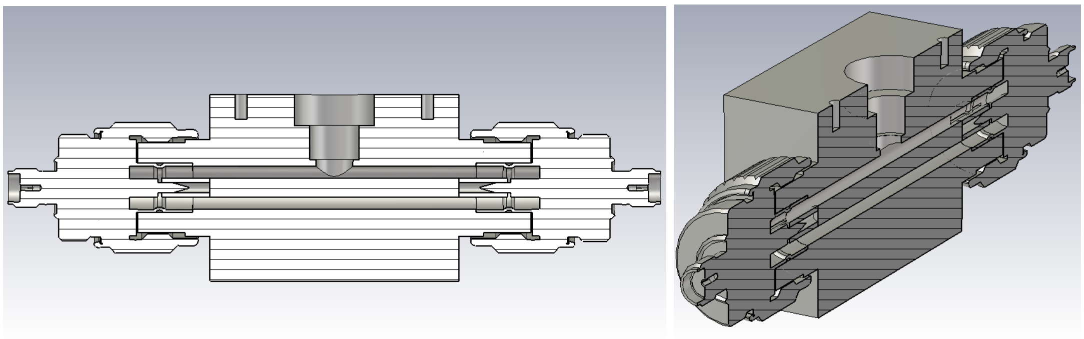
(a) (b)

Fig. 5.3 Three ports test fixture (3PTF): (**a**) cut view, (**b**) 3D cut view.

It is based on a 50 Ω nominal characteristic impedance coaxial line that, through an aperture located at its middle length, is able to couple with the beam port of the pick up under test. The pick up is mounted orthogonally to the coaxial line. The coaxial line structure has been chosen because it supports the TEM propagation mode, the same supported by charged particle relativistic beams. Due to practical machining constraints, the outer diameter of the inner conductor has been fixed to 3 mm, while the inner diameter of the outer conductor has been fixed to 7 mm, according to the IEC 61169-16 standard for N connectors [24]. The ratio between these value is 2.33, corresponding to 50.8 Ω. The calculated cutoff frequency of the first high order mode of the coaxial line, the TE_{11} one, is 19.4874 GHz. The commercial N to SMA adapters (N-MALE to SMA-F) mounted to support the inner conductor of the coaxial line have a maximum operative frequency of 16 GHz. Being lower than the propagation frequency of the TE_{11} mode, 16 GHz is then set as the maximum operating frequency for such kind of test fixture. This test fixture has been used to characterize the transfer impedance of the third and fourth generation of home made pick ups, as detailed described in the next paragraphs. It has also been used to validate the first batch of 16 prototypes of Elettra 2.0 pick ups, as described in the next chapter.
To further extend the number of pick ups that can be tested simultaneously, the 3P type test fixture has been modified to host four pick ups, mounted orthogonally to the coaxial line and spaced 90 ° each other. The total number of RF connectors is six, hence the "6P" naming for

this test fixture.
The last type of test fixture, named "bazooka", was already developed in house (more than twenty years ago) for the measurement of the BPMs mounted in Elettra. Based on a six port design, it was used only for the evaluation of the first generation of home made pick ups. Further details are reported in the paragraph dedicated to this generation of pick ups.

5.4.4 Fundamental electromagnetic models of the test fixtures

The electromagnetic behavior of the test fixtures is influenced by the pick-up they host during testing. In the event of anomalous results, it may be difficult to determine whether the source of the anomaly lies in the test fixture or in the pick-up itself. Establishing a reference pick-up characterized by simple geometry and dielectric material renders the comparison between simulated and measured data less susceptible to uncertainties, particularly those associated with the variation of ε_r as a function of frequency. The most straightforward pick-up design to be manufactured is realized simply as an extension of the internal coaxial structure of the K connector, following the approach already adopted for the antenna of the 2PTF, see Figure 5.4. Given the reduced dimensions of the test fixtures under evaluation, the materials are modelled as ideal: PEC (perfect electric conductor) for metallic parts and background, vacuum for the inner volume. For the purposes of the analysis, the electrical contact between the pick-up and the housing in each test fixture is considered ideal. Two different 3D electromagnetic analysis code have been used for the test fixtures model study, CST [14] and HFSS [5].

For the experimental measurements, a Teledyne LeCroy WavePulser 40iX was employed for time-domain analysis (transmission and reflection up to 40 GHz). For frequency-domain characterization up to 26.5 GHz, a Keysight PNA network analyser was used.

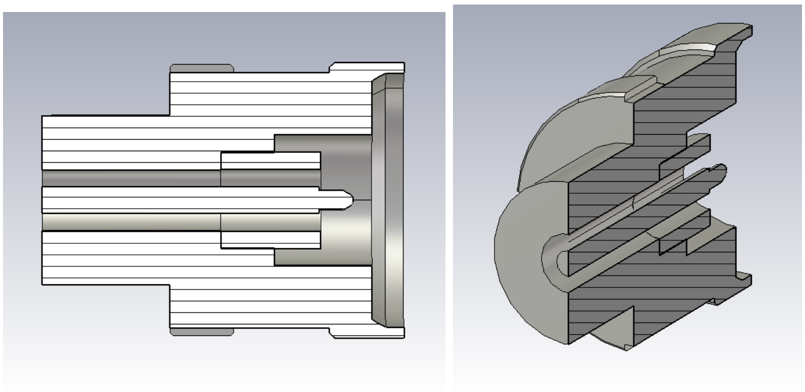

(a) (b)

Fig. 5.4 Uniform pick-up: (**a**) cut view, (**b**) 3D cut view.

2PTF fundamental electromagnetic model

The mechanical model of the 2PTF with the reference pick-up installed is illustrated in Figure 5.5a, and the corresponding electromagnetic model is reported in Figure 5.5b. Within the numerical calculation domain, the real-world connector K (C2) is modelled as coaxial port P2. The same for the other K connector and port. The female K connector, which supports the antenna pin of the reference pick-up, is not depicted in Figure 5.5a. The comparison between the measured and simulated scattering parameters is shown in Figure 5.6. The agreement between measured and simulated data is very good.

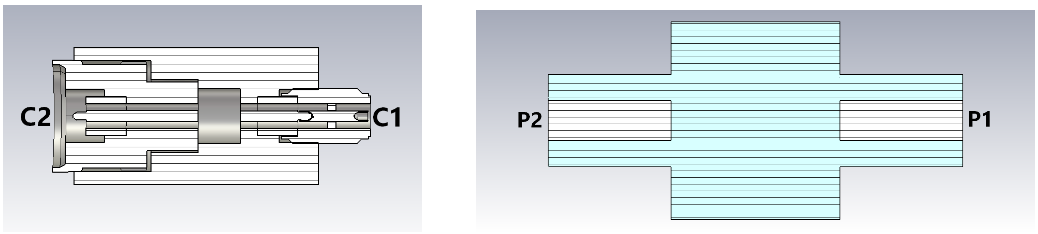

(a) (b)

Fig. 5.5 2PTF: (**a**) cut view, (**b**) 3D cut view.

3PTF fundamental electromagnetic model

The mechanical model of the 3PTF with the reference pick-up installed is illustrated in Figure 5.7a, and the corresponding electromagnetic model is reported in Figure 5.7b. Within the numerical calculation domain, the real-world connector K (C2) is modelled as coaxial port P2. The female K connector, which supports the antenna pin of the reference pick-up, is not depicted in Figure 5.7a. In the electromagnetic model, the C1 and C3 transitions from K to N connectors are considered ideal and are represented by ports P1 and P3. Because of the symmetry of the test fixture, port P1 (C1) and port P3 (C3) can be interchanged without affecting the results. The comparison between the measured and simulated scattering parameters is shown in Figure 5.8. The agreement between measured and simulated data is very good.

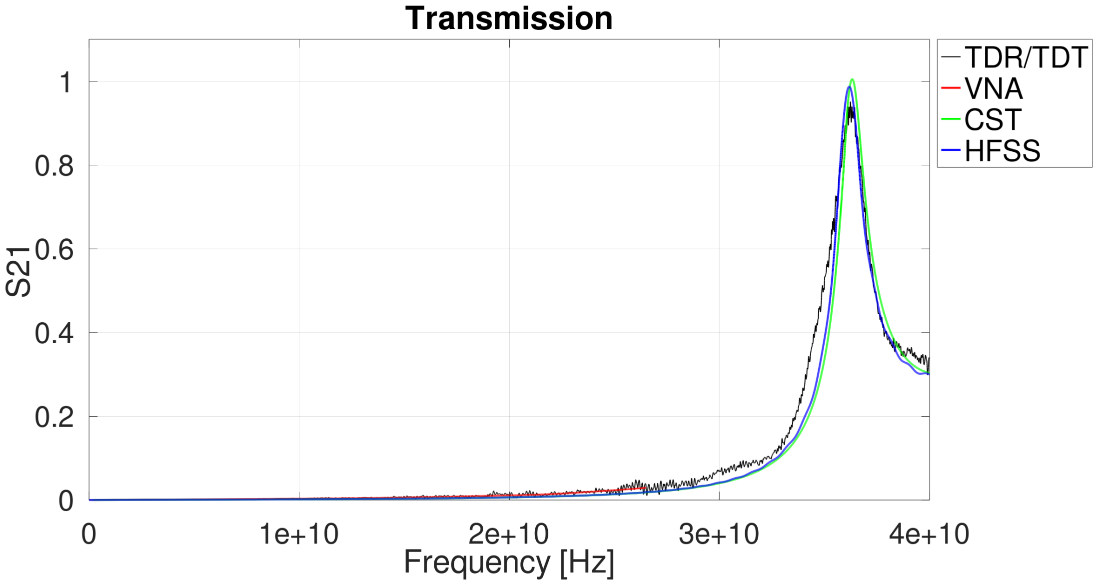

(a) S_{21} frequency response.

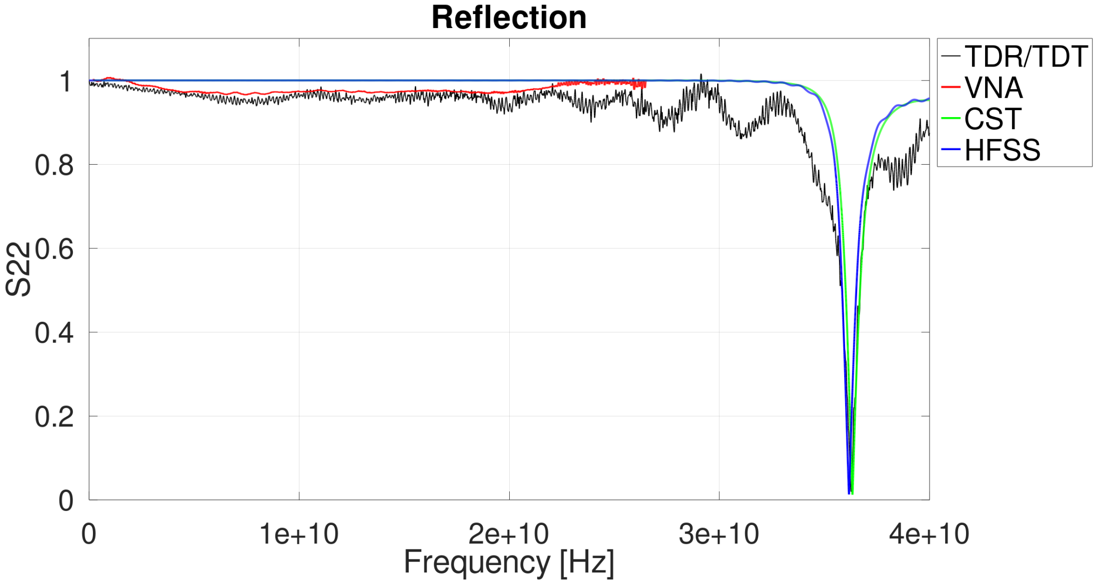

(b) S_{22} frequency response.

Fig. 5.6 Comparison between the measured and simulated scattering parameters for the 2PTF case.

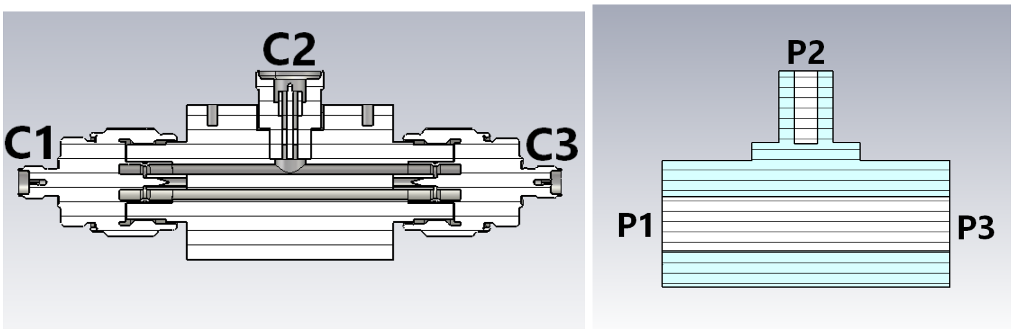

(a) (b)

Fig. 5.7 3PTF: (**a**) cut view, (**b**) 3D cut view.

5.5 The first Home Made Pick Up generation

The first generation of home made pick ups (HMPU) has been designed according to the PU4 shape using already available in house ceramic rings made of Steatite, a quite diffused insulator used for high-voltage low frequency applications. The steatite's relative permittivity ε_R at 50 Hz is 6, whereas its relative permeability μ_R is 1. As a first order approximation, it has been assumed that ε_R and μ_R remain constant with respect to frequency, and that there are no dielectric losses. To assure mechanical compatibility with the Elettra's pick ups, the HMPU body external geometry and dimensions has been chosen to match the holes already available in spare BPM bodies of Elettra.

5.5.1 Pick up structure

The detailed structure of the first generation pick ups is shown in Figure 5.9. The central pin is made of copper. It has a cone base with diameter of 7.4 mm (the Elettra pick up has a button with diameter of 10 mm) and gap 0.2 mm. The pick up body is divided in three parts: two are made of stainless steel, while the third, that hosts a commercial 50 Ω press mount SMA female connector, is made of copper. The ceramic ring is mechanically connected to the central pin and to the housing through a thin layer of ultra high vacuum compatible glue. As already mentioned, the ceramic ring is made of steatite. The uniform coaxial section of the pick up has 50.5 Ω characteristic impedance, with the inner diameter of the outer conductor $D = 6.5$ mm and the outer diameter of the inner conductor $d = 2.8$ mm.

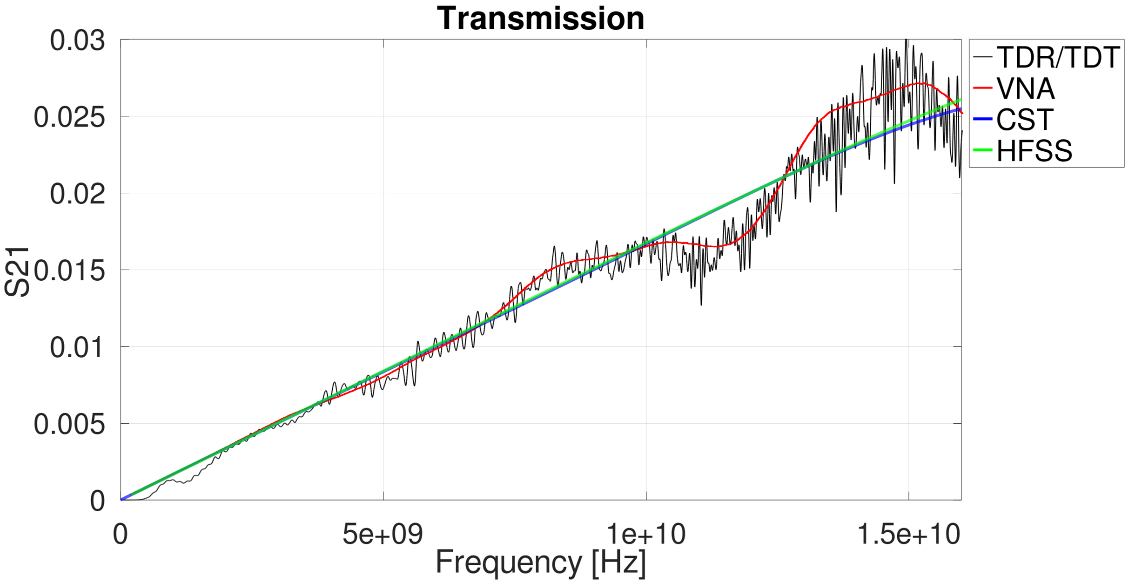

(a) S_{21} frequency response.

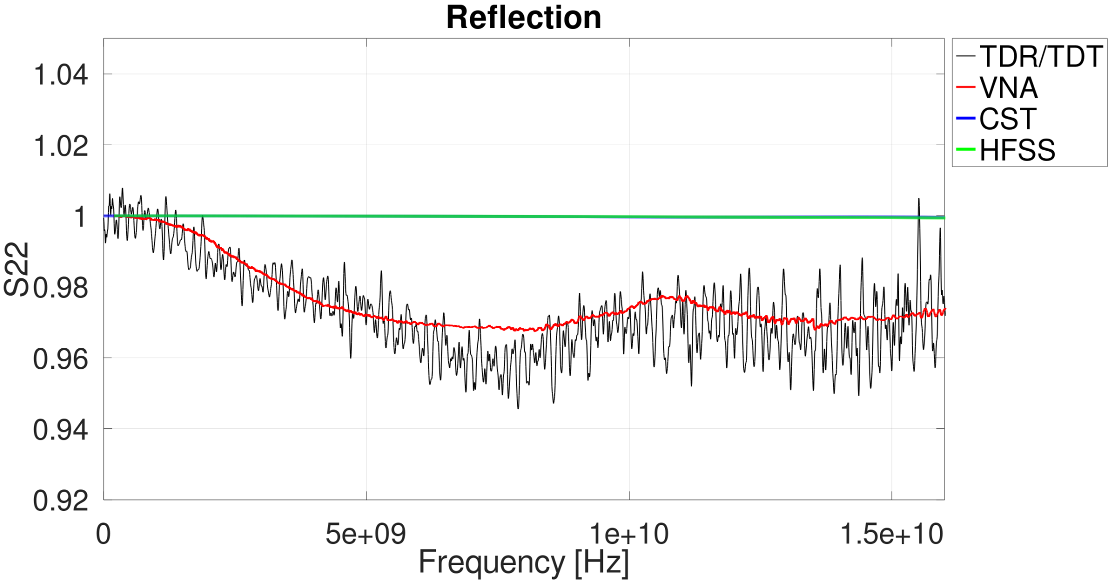

(b) S_{22} frequency response.

Fig. 5.8 Comparison between the measured and simulated scattering parameters for the 3PTF case.

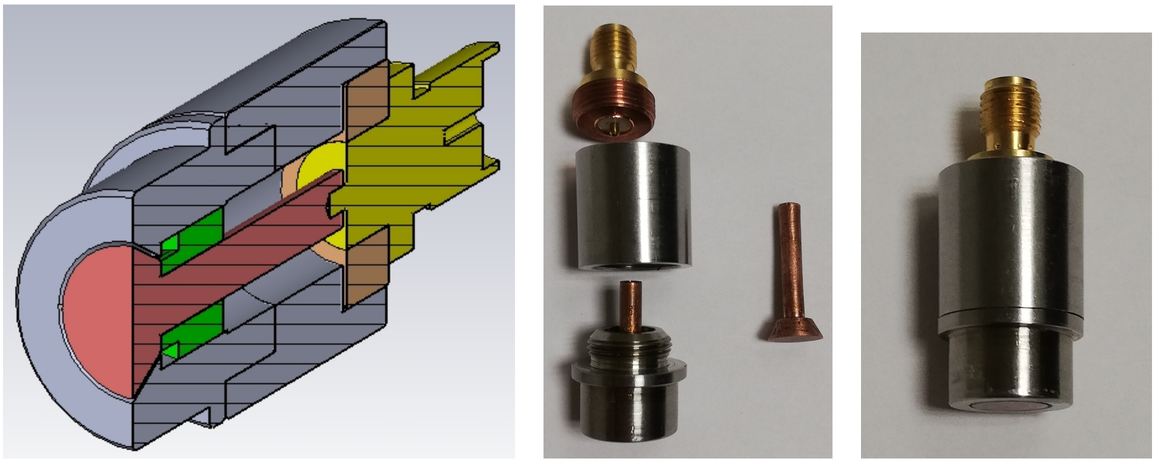
(a) (b) (c)

Fig. 5.9 Manufactured PU: (**a**) cross-section, (**b**) disassembled, (**c**) assembled.

5.5.2 Electromagnetic model

Starting from the physical model shown in Figure 5.9, the following assumption have been made in order to define the simplified EM model of the pick-up, shown in Figure 5.10a:

- the press mount SMA connector is not considered in the simulation because, having a nominal bandwidth of 18 GHz (L-com LCCN3164), it is assumed that it does not introduce any unwanted EM effect;
- the ε_R of steatite is supposed non varying with frequency;
- the ultra high vacuum glue is considered so thin that its effect can be neglected in the range of operating frequencies of the PU;
- the contact between the pin of the SMA connector and the copper central pin is considered perfect as a first guess. This point is particularly critical in terms of RF matching between the coaxial inner structure of the PU and the SMA connector;

The electromagnetic model of the BPM used as six ports test fixture, filled with the four pick-ups, is shown in Figure 5.10b.

5.5.3 Test Bench Experimental results

The experimental verification of the reliability of the numerical simulations was carried out by two sets of measurements performed on a group of four nominally identical first generation HMPUs.

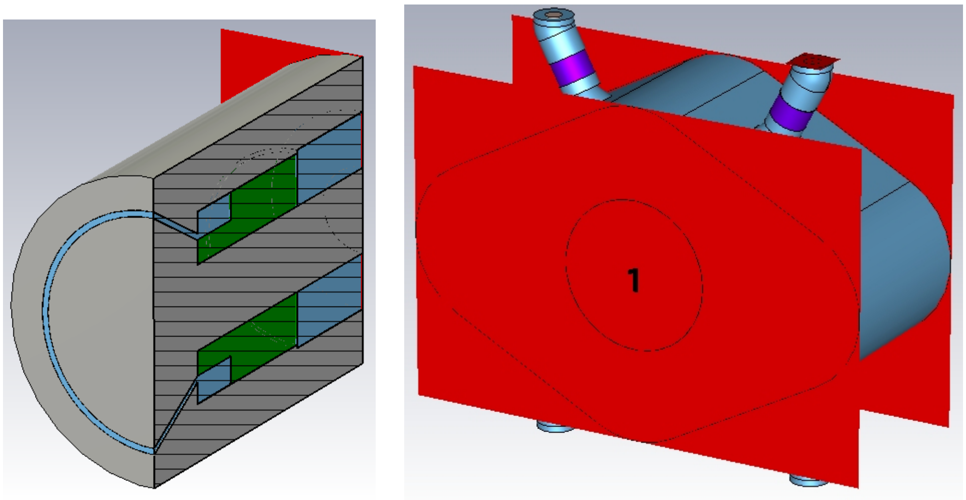

(a) (b)

Fig. 5.10 First generation HMPU electromagnetic models: (**a**) pick-up, (**b**) six ports test fixture.

TDR measurements

The first set of experimental values has been obtained by using a Teledyne T3SP15D reflectometer, which is employed to measure the TDR characteristics of the four manufactured pick-ups in open-air mode. The obtained results are reported in Figure 5.11, where the measured curves are represented by the four colored thin lines, while the simulated one is indicated by the black dotted line. Except from a evident deviation of the red curve, the other three experimental ones are very close to the numerically derived performance, with the observed dispersion that may due to the manufacturing process, which, at this preliminary stage, has not been optimized.

VNA measurements

The second set of laboratory tests on the in-house PUs has been carried out through a VNA to assess how the buttons couple to a particle beam as the frequency changes. The measurement setup consists of two sections of a vacuum chamber with the dimensions equal to those of the current Elettra accelerator, in which a BPM body can be inserted in a central position (Figure 5.12a). The two ends of the vacuum chamber are connected to a pair of N-connectors, which internally support an aluminum conductor of dimensions approximating a coaxial conductor adapted to 50 Ω impedance (Figure 5.12b). Through the dedicated ports, it is then possible to feed the system with an RF signal terminating on a matched load. The buttons hosted in the BPM couple with the EM field (Figure 5.12c). Hence, by analyzing the present

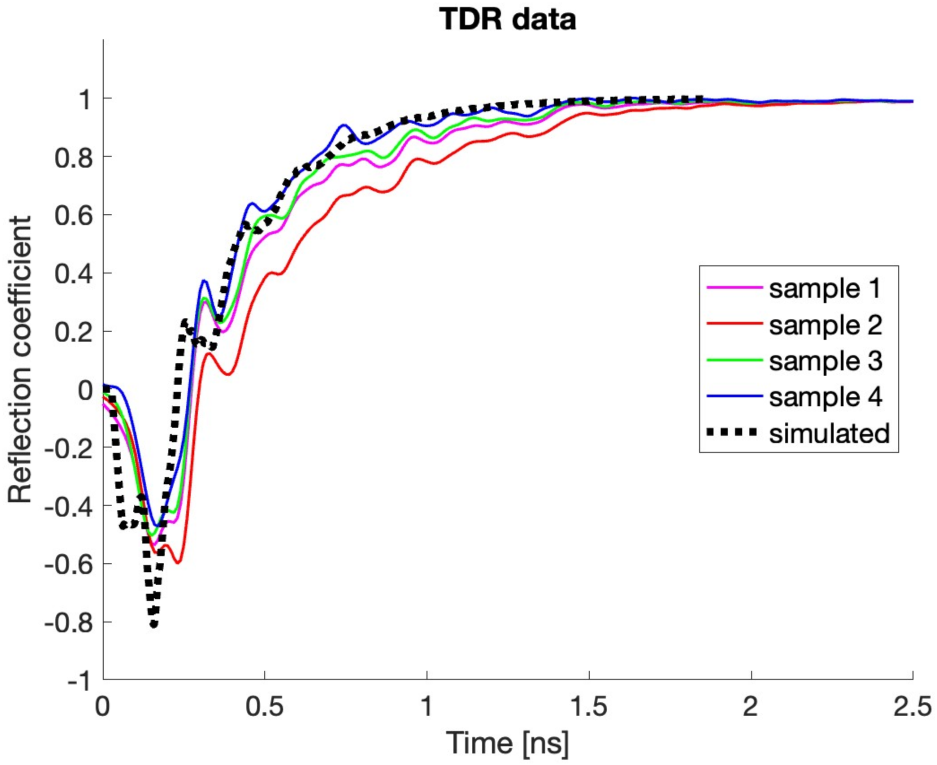

Fig. 5.11 First generation of home made pick ups: experimental and simulated TDR signals.

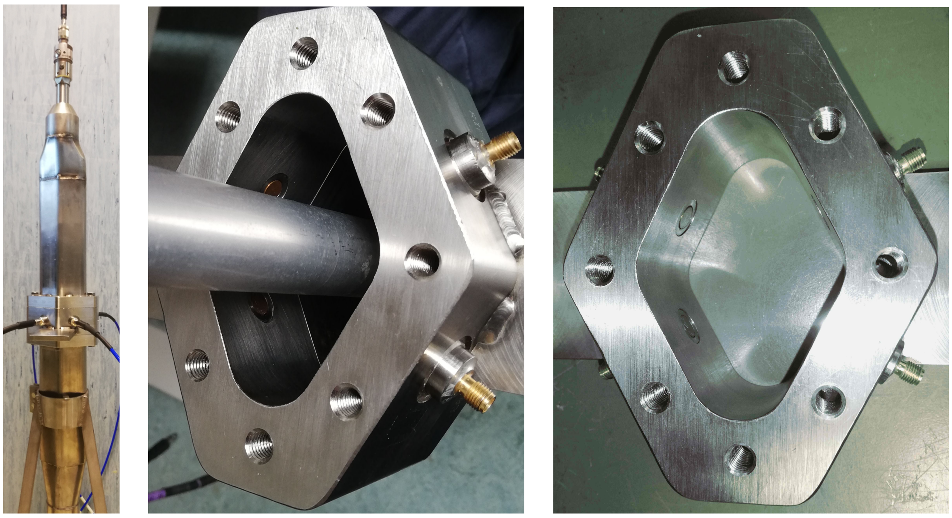
(a) (b) (c)

Fig. 5.12 VNA measurements: (**a**) assembled six ports test fixture, (**b**) inner coaxial conductor, (**c**) BPM body with pick-ups.

signal, it becomes possible to measure the frequency response of the button inserted into its operating environment. The acquisitions have been carried out through a Keysight PNA network analyzer, which has been used to feed the coaxial line while reading the signal present on one of the four buttons, thus showing the trend of the S_{21} parameter as a function of the frequency. Figure 5.13 shows the measured transmission scattering parameters and the simulated S_{21} obtained by the model indicated in Figure 5.10b . The agreement between measured and simulated data is good for conducting tests in real accelerator operating conditions.

5.5.4 Experimental results in real operating conditions

The good agreement between simulations and measured behavior suggested to push forward the experimentation of the first generation HMPUs in a real operating environment. The thin film of glue used to sustain the central pin to the ceramic ring, and the ceramic ring to the pick up body, was not able to pass the vacuum leak test required to check the minimum value of hermeticity mandatory for ultra high vacuum applications. Adding extra glue to each pick up fixed the vacuum leak problem, but the microwave characteristics of the pick ups were altered respect to the previously measured ones. These deviations were not considered an issue in this early prototyping stage, and a brand new BPM body was designed and machined in house. Once successfully vacuum tested the BPM body, the HMPUs were glued on it, and the full BPM assembly, shown in Figure 5.14a, was tested and validate for UHV applications.

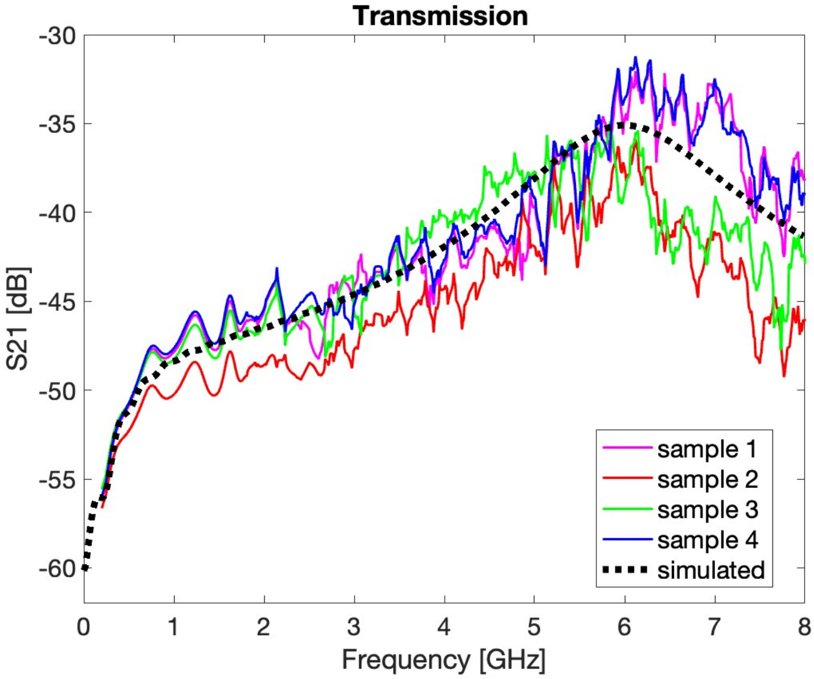

Fig. 5.13 First generation of home made pick ups: experimental and simulated transmission coefficient.

In order to mitigate the risk of vacuum leaks during normal machine operations, the BPM was mounted in the terminal part of the 100 MeV pre-injector linac , downstream a vacuum valve, as shown in Figure 5.14b.

The Pre-injector linac

The Pre-injector linac is the particle accelerator in charge of generate electron bunches from scratch, and accelerate them up to 100 MeV, the input energy of the booster. It consists of the cascade of the following components:

- an electron gun that emits a continuous flow of electrons up to 80 KeV;
- a 500 MHz pre-buncher cavity;
- a 3 GHz buncher cavity;
- two 3 GHz linear accelerating section that accelerate the electron beam up to the injection energy of the booster.

The pre-injector provides single and multi bunch electron beams, as well as operation in top-up mode. In single bunch mode, a 1 ns time duration extraction voltage pulse acts on the

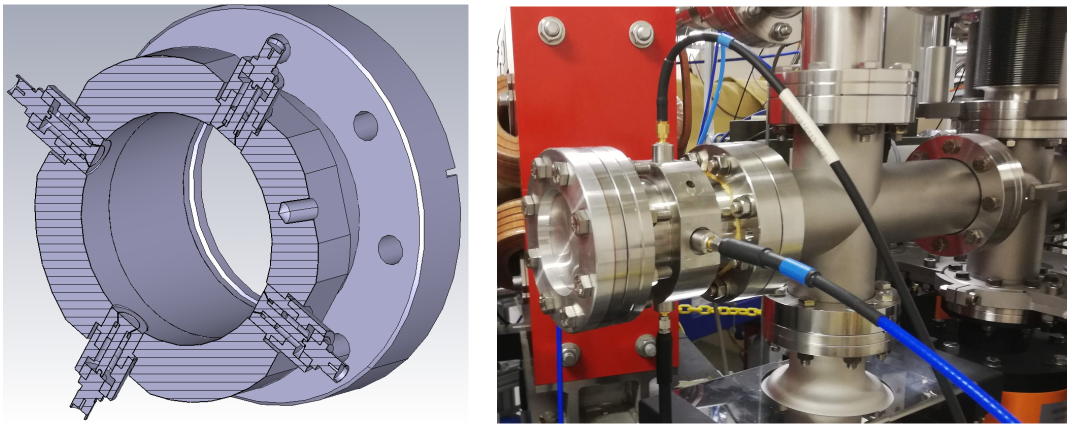

(a) (b)

Fig. 5.14 First generation HMPU BPM assembly: (**a**) cross section, (**b**) real device mounted at the end of the pre-injector.

electron gun. In multi bunch mode the time duration of the extraction voltage pulse can be adjusted up to 300 ns [16].

Pre-injector beam analysis

During a dedicated shift the signals generated by the pre-injector beam passing through the HMPU BPM were acquired by a 6 GHz oscilloscope, both in single bunch and multi bunch operating conditions. Due to the bad quality of the signal extracted from a pick up, only three signals out of four could have been analyzed. The value of the extracted charge per bunch was around 8 pC, an exact value was not required for such kind of preliminary measurements.

Figure 5.15 shows the signals generated by the BPM in multi bunch mode, centered beam conditions, with an extraction pulse duration set to 200 ns. The comparison between the measured time duration of the acquired signals, of the order of 800 ns (4 time divisions, 200 ns/div), with the expected time duration, 200 ns, suggested that there was an error in the measurement setup. Thanks to a transverse trajectory scan, the problem was recognized as "trapped electrons" effect, due to the very short distance between the pick ups and the thin flange that terminates the pre-injector, that acts as partial beam dump (see Figure 5.14b).

With reference to Figure 5.16, comparing the signal generated by a fast charge monitor located close to the gun, trace C1, with the signals generated by two pick ups with the beam slightly off axis, C2 and C3 traces, the "trapped electrons" effect was confirmed. In order to reduce as much as possible the "trapped electrons" effect, the beam was further deflected away from the centered condition.

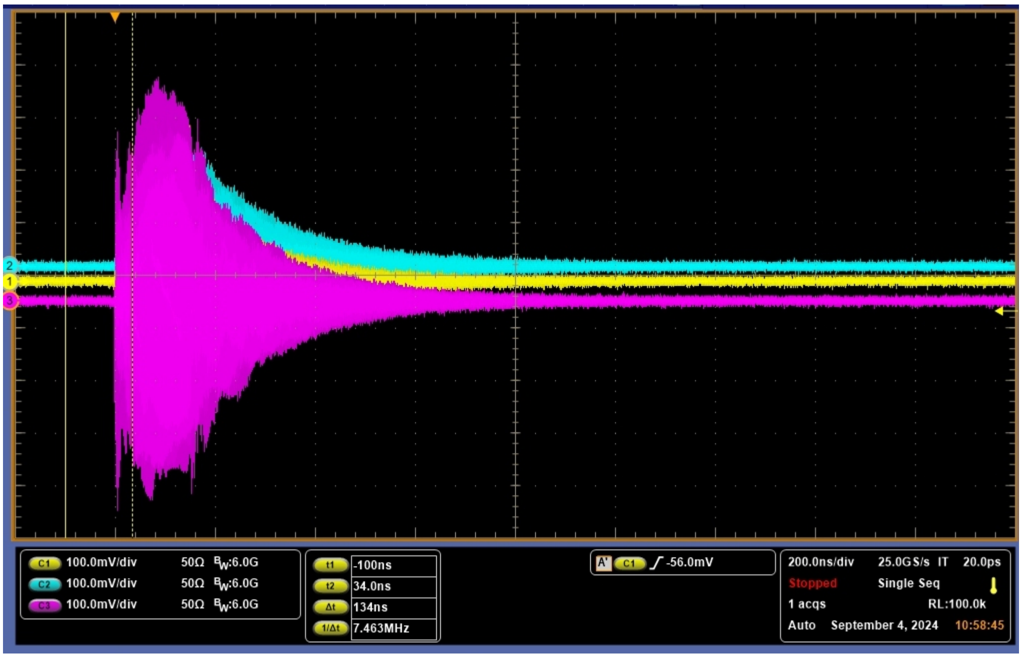

Fig. 5.15 Multi Bunch signals corrupted by “trapped electrons”.

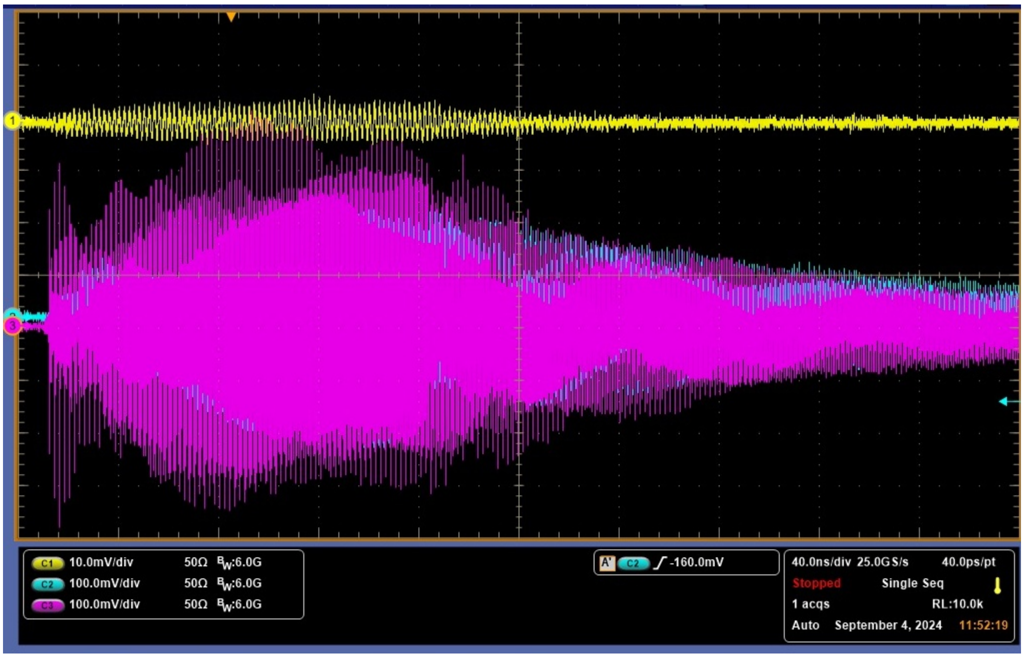

Fig. 5.16 Multi Bunch signals compared with the fast charge monitor signal.

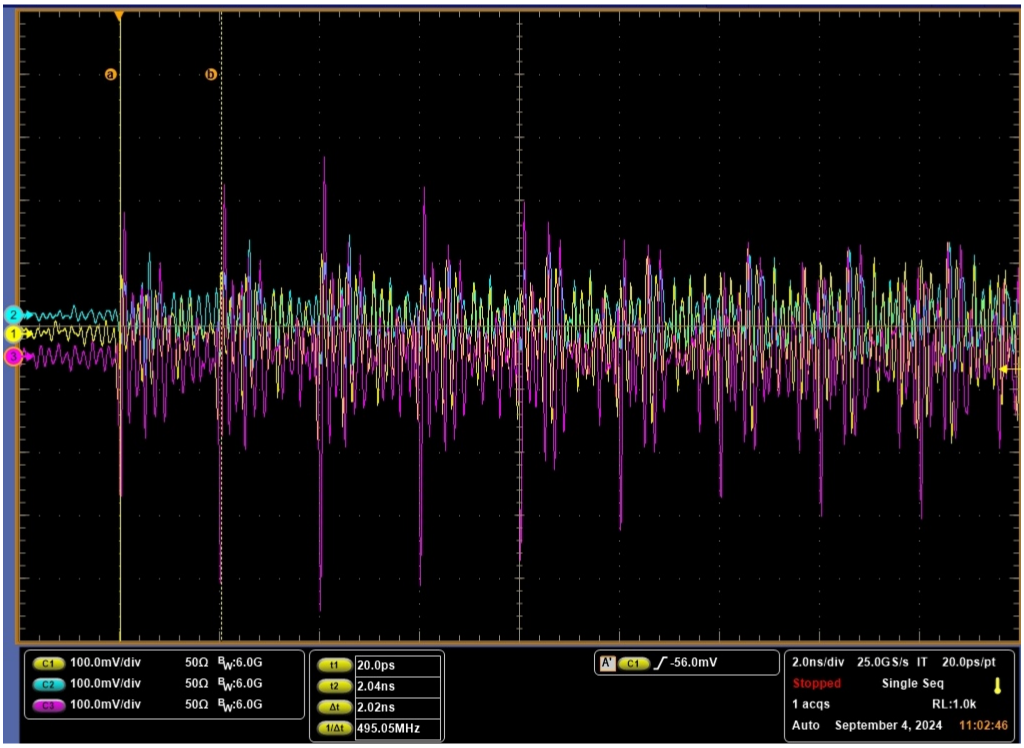

C1 100.0mV/div 50Ω BW:6.0G
C2 100.0mV/div 50Ω BW:6.0G
C3 100.0mV/div 50Ω BW:6.0G

t1 20.0ps
t2 2.04ns
Δt 2.02ns
1/Δt 495.05MHz

A' C1 -56.0mV

2.0ns/div 25.0GS/s IT 20.0ps/pt
Stopped Single Seq
1 acqs RL:1.0k
Auto September 4, 2024 11:02:46

Fig. 5.17 Multi Bunch signals with pre-buncher on.

Figure 5.17 shows the head of the multi bunch beam when the pre-buncher is powered on. The main signal peaks are distant 2 ns each other (corresponding to 500 MHz), according to the charge suppression mechanism implemented by the pre-buncher cavity.

Figure 5.18 shows the head of the multi bunch beam when the pre-buncher is powered off. Now the signal peaks are distant 0.333 ns each other (corresponding to 3 GHz, that is the minimum intra bunch distance for 3 GHz accelerating structures.

Figure 5.19 shows the single bunch filling pattern when the pre-buncher is powered off. The three pulses of the picked up signal overlap with the 1 ns extraction voltage pulse. The three amplitudes of the 3 GHz sub bunches are almost the same, according to the power off status of the pre-buncher.

Figure 5.20 shows the single bunch filling pattern when the pre-buncher is powered on. Now the charge is practically all concentrated in the central sub bunch of the 3 GHz filling pattern, according to longitudinal charge capture capability of the pre-buncher.

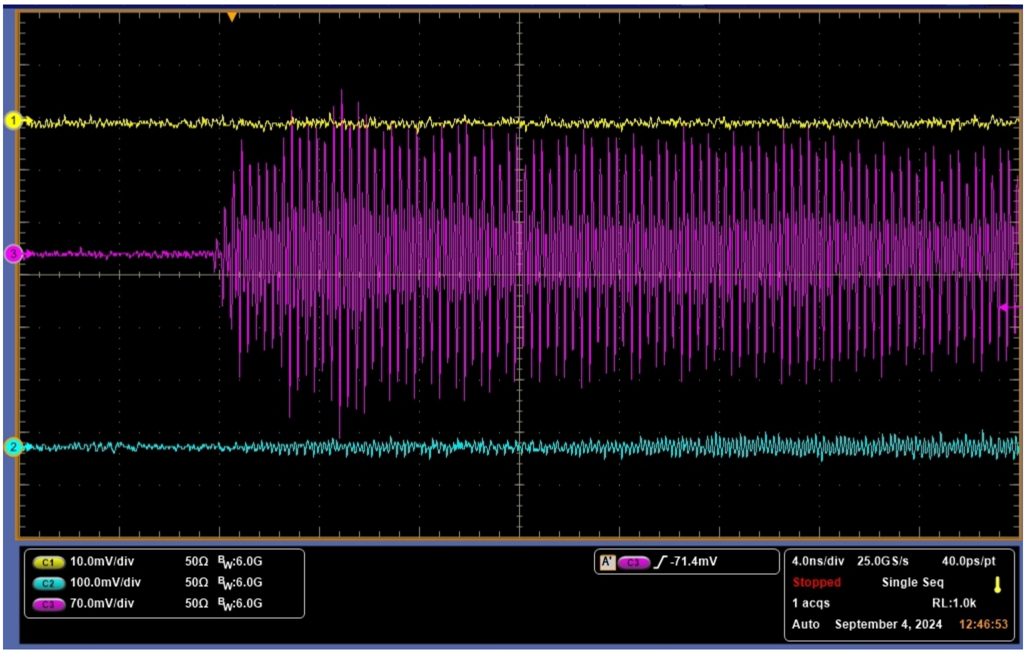

Fig. 5.18 Multi Bunch signals with pre-buncher off.

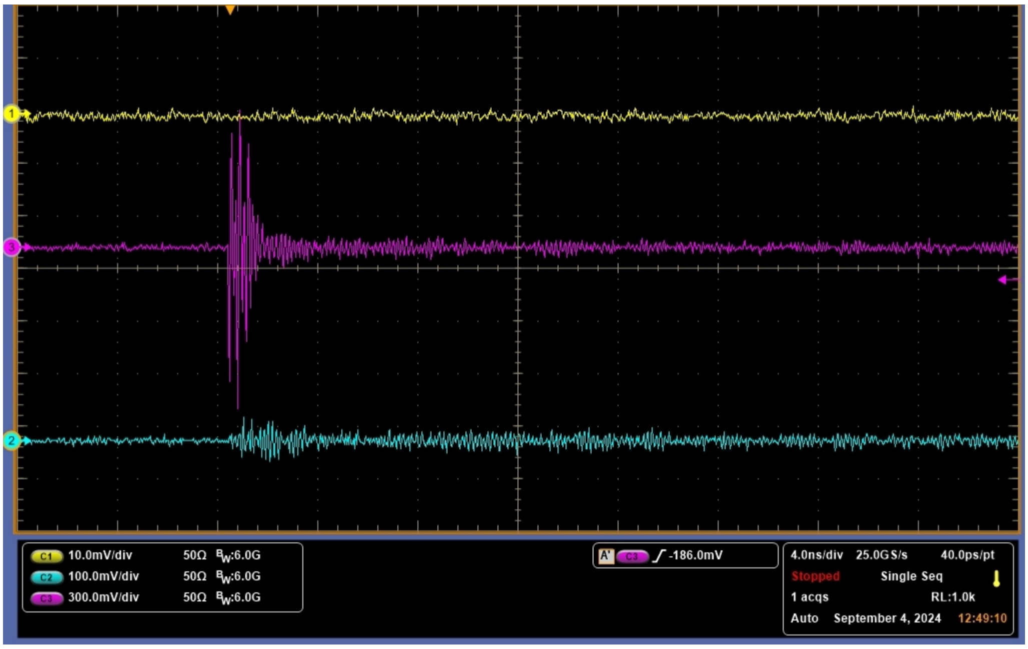

Fig. 5.19 Single Bunch signals with pre-buncher off.

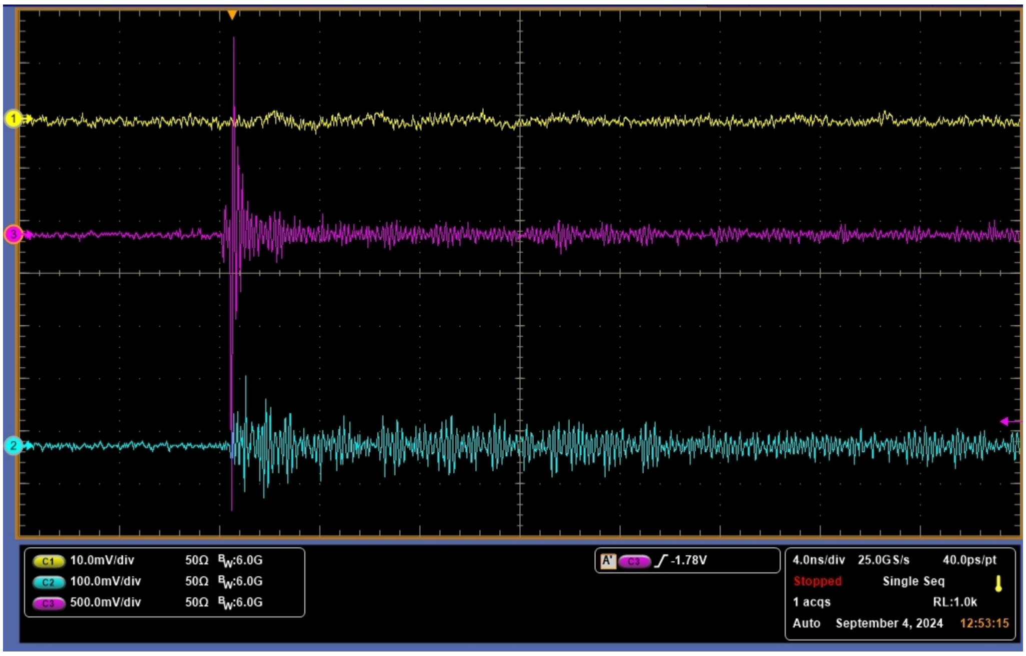

Fig. 5.20 Single Bunch signals with pre-buncher on.

5.5.5 Conclusions about the first generation home made pick up

The first generation of home made pickup prototypes allowed to reach two milestones in the design process of the pickups for Elettra 2.0:

- validate the electromagnetic simulations through real measurements on dedicated test equipment;
- perform meaningful measurements on the pre-injector beam in different operating conditions;
- validate the UHV capabilities of the glued pick ups.

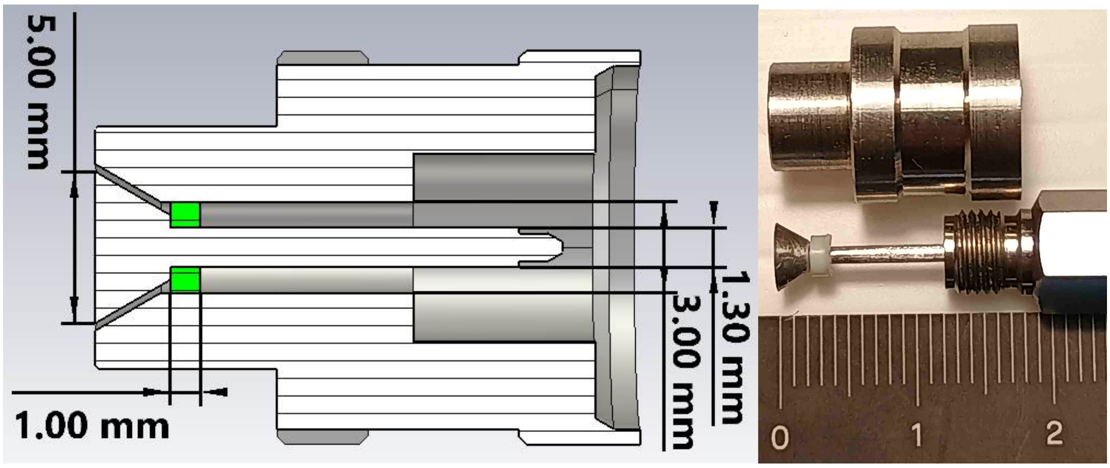

(a) Drawing of the second generation HMPU.

(b) Second generation HMPU before assembling

Fig. 5.21 Second generation HMPU prototype

5.6 The Second Home Made Pick Up generation

The good results obtained by the first generation of the Home Made pick-ups encouraged the manufacturing of a second generation of devices having a conical shape whose size is close to the one foreseen for Elettra 2.0, see Figure 5.21a. The detailed view of the parts used for the construction is shown in Figure 5.21b. The PU body is made of stainless steel, the central pin is made of aluminum. A small ring made of Teflon has been mounted on the top of the conical section to show the location of the insulator. A standard female K connector is also shown in the picture.

In this kind of pickup the ceramic ring is not required any more because the UHV glue acts both as electric insulator and vacuum proof barrier. The nominal ε_R of the glue is 6. The design target thickness of the glue is 1 mm. Due to the small size of such kind of pickup, a dedicated assembly tool has been realized, see Figure 5.22a. Its goals are:

- to assure the right radial and axial mechanical alignment between the central pin and the pickup housing;
- to fix the insulator thickness, limiting the penetration of the glue up to the reference surface defined by the top side of the white cylinder shown in the center of Figure 5.22a.

Figure 5.22b shows the configuration of the assembly just before putting the glue on the reference surface. Once the glue has been deposited, the central pin can be pushed down until it get in contact with the glue.

(a) Empty assembly tool.

(b) Pickup body and electrode ready to be vertically aligned immediately after the glue has been applied.

Fig. 5.22 Assembly tool for the second generation of HMPU.

Due to the reduced dimensions of this type of pickup, to simplify the mechanical machining and, as a consequence, speed up the production time of the pickup body, the K connector collar was not implemented. This means that the connector's reference plane is undefined in this generation of pickups; the comparison between Figure 5.1a and Figure 5.21a makes this clear. The incomplete connector on the pickup side introduces an impedance mismatch along the propagation path of the extracted beam signal. To evaluate the effect of such impedance mismatch, two numerical simulations had been performed through a "theoretical" 3PTF. The thickness of the glue used as dielectric had been assumed equal to 1 mm. The first simulation, named "Zok", is based on a full K connector, that assures a real coaxial line up to the cable connector. The corresponding electromagnetic model is reported in Figure 5.23. The second simulation, named "Zwr", takes into account the effective inner geometry of the pickup up to the cable connector, supposed of K type. The corresponding electromagnetic model is reported in Figure 5.24. The comparison of the transmission performance of the two pickup configurations, Zok and Zwr, expressed by the S_{21} scattering parameter, is shown Figure 5.25. According to the convention defined about the naming of the ports of the 3PTF, port 2 is reserved to the pickup under simulation, and port 1 and 3 are used to feed signal into the coaxial line. Up to 2.5 GHz, the transfer characteristics of the two pickups are almost the same. Taking into account that the Elettra's RF detector operate tuned on 500 MHz, this means that the lack of a complete K connector is not an issue for the second generation pickup prototypes.

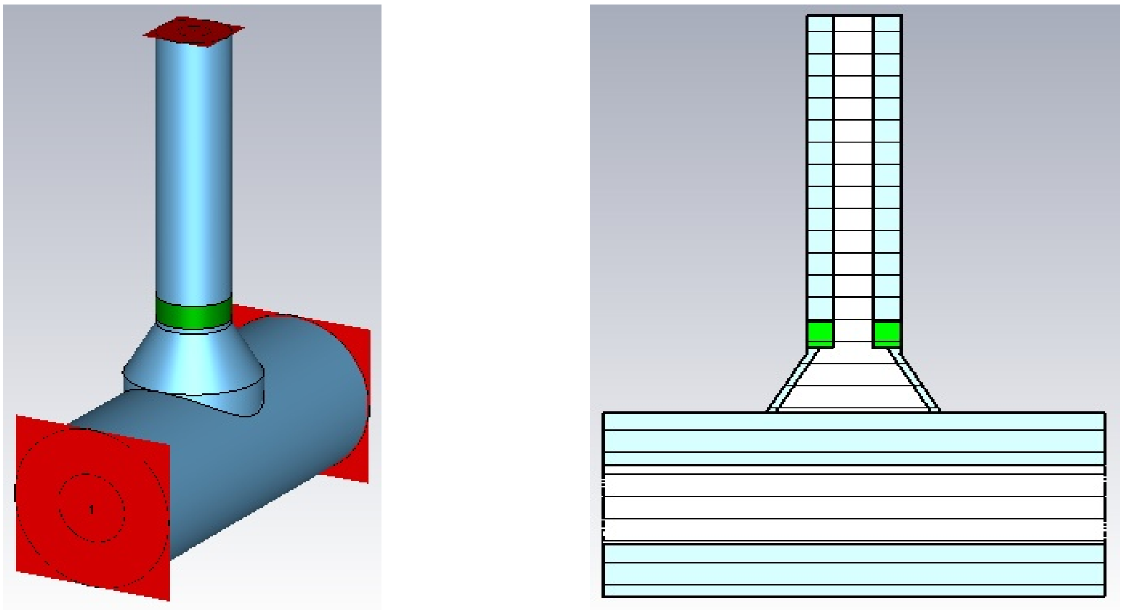

(a) Zok electromagnetic model. (b) Zok electromagnetic model.

Fig. 5.23 Electromagnetic model of the "Zok" second generation HMPU mounted on a 3PTF

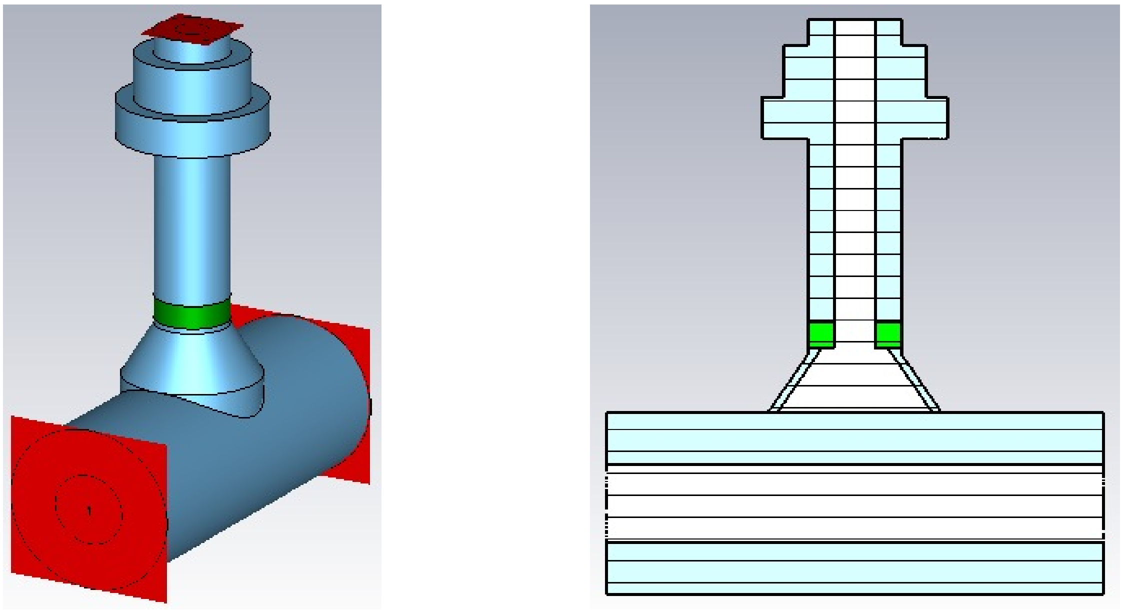

(a) Zwr electromagnetic model. (b) Zwr electromagnetic model.

Fig. 5.24 Electromagnetic model of the "Zwr" second generation HMPU mounted on a 3PTF

On the other hand, over 2.5 GHz the different transmission behavior of Zwr with respect to Zok introduces distortions that are not present in the pickup signals calculated through wakefield simulations, always performed assuming ideal connectors. This means that the

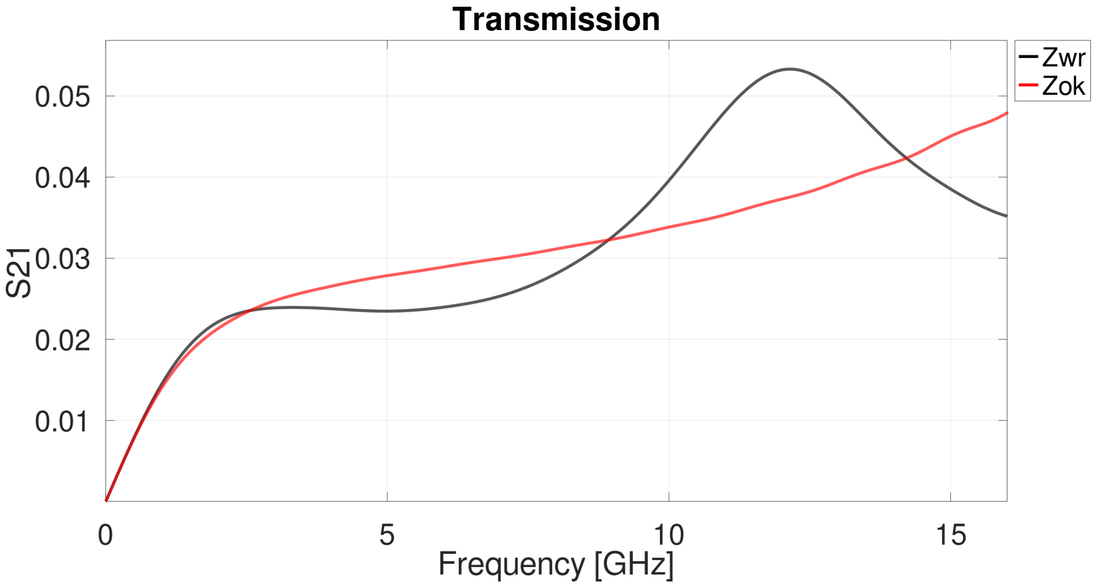

Fig. 5.25 Transmission coefficients comparison between Zok and Zwr like pick-ups.

comparison between the signals induced by the beam in the pickups and the signals acquired in real operation conditions through a wide band oscilloscope are different by definition. Even this case is not considered an issue because in the best measuring conditions, the frequency response of the cables to be used during real tests is known up to 18 GHz. For a preliminary evaluation of the pickup behavior over this frequency any attempt to take into account the effect of the cables became extremely tricky.

5.6.1 Electromagnetic characterization of the first second generation HMPU prototypes.

The necessary parts for six second-generation pick-ups were machined and glued in-house. Once the manufacturing process was complete, the pickups were measured to check in open air (the less repeatable method) their characteristics. The absence of short circuits was verified using a multimeter. Through a Teledyne Lecroy WavePulser 40iX High-speed Interconnect Analyzer, the following data related to the reflection characteristics were measured:

- the S_{11} scattering parameter, as indicated in Figure 5.26;
- the time profile of the reflected signal, as shown in Figure 5.27. The impedance profile along each pickup sample is proportional to the corresponding raw signal (i.e. no post processing corrections are applied).

As clearly shown by Figure 5.26 and Figure 5.27, the measured pick-ups do not behave in the same way, but such differences in their characteristics were accepted at this stage in the evolution of the homemade manufacturing process. These pick ups were mounted onto a dedicated BPM body in order to test their behavior in real operating conditions on the Elettra storage ring.

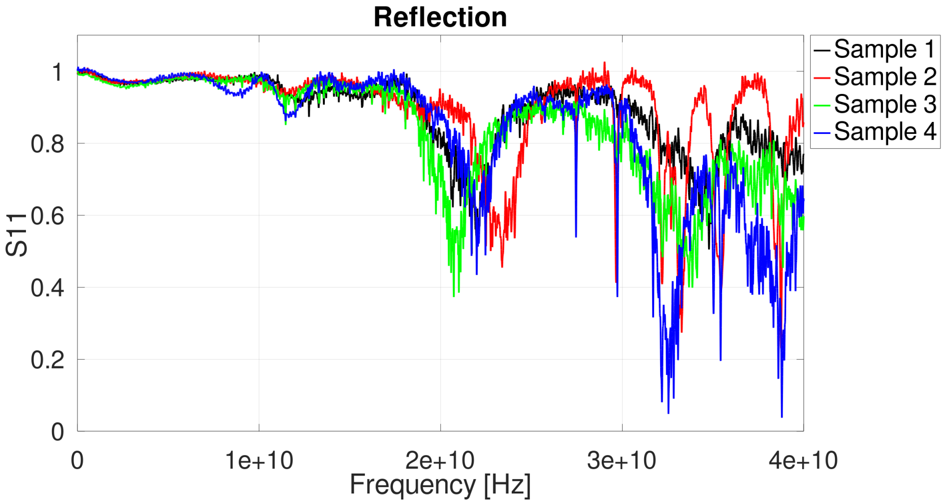

Fig. 5.26 Open air TDR test of the second generation pick-up prototypes.

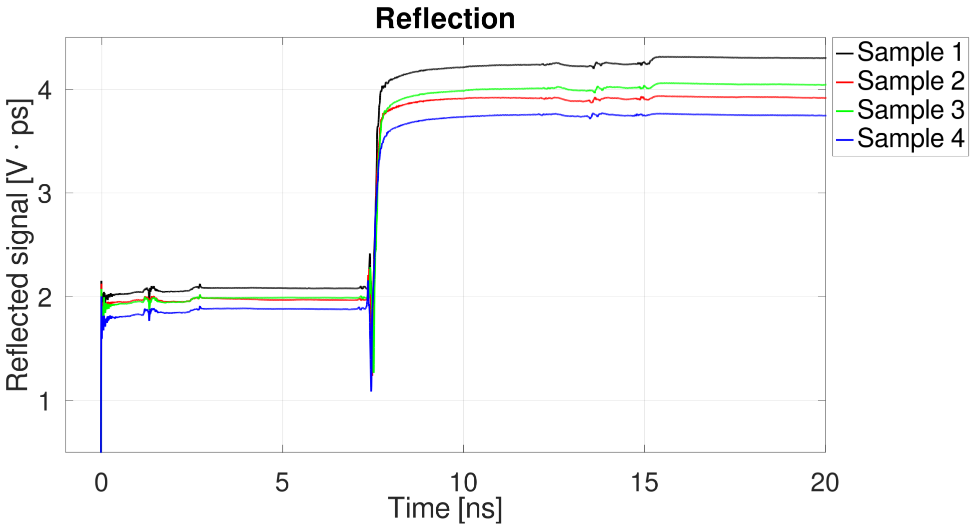

(a) Full range TDR acquired reflected signal.

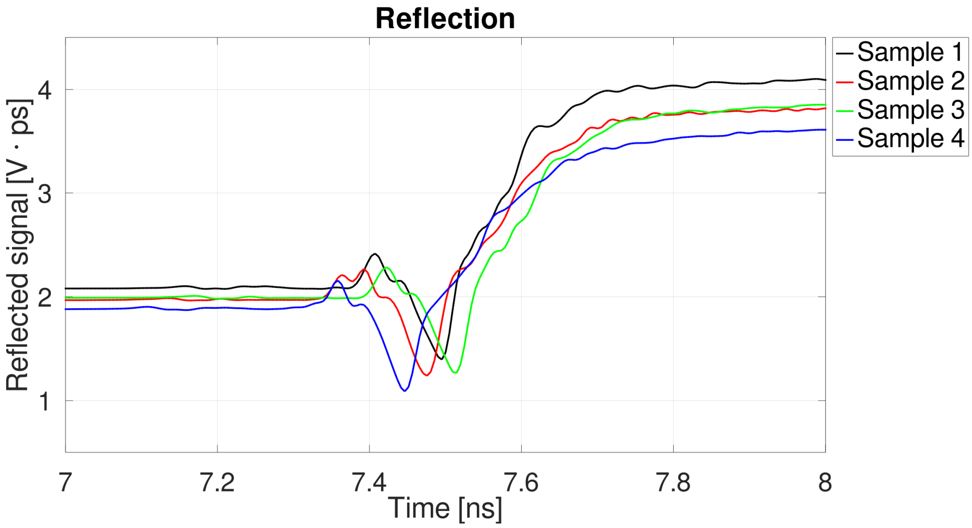

(b) Detailed view of the effect of the conical part of the pick up on the reflected signal.

Fig. 5.27 Time profile of the reflected signal in open air: (**a**) full time range, (**b**) detailed view of the effect of the conical transition.

5.6.2 The second generation BPM

The shape and size of the BPM body that was designed to accommodate the second-generation pickup samples was determined by a compromise between the smallest available vacuum pipe size in Elettra, and the size of the BPMs foreseen for Elettra 2.0. The best match was found in an elliptic low-gap BPM mounted in Elettra, upstream an undulator. Its vertical aperture of 14 mm is close to the corresponding aperture of the Elettra 2.0 BPMs, equal to 17 mm. The inner dimensions of the low-gap BPM were hence cloned to create a brand new BPM body to host the second generation HMPU samples, as shown in Figure 5.28. The horizontal distance between the axis of the pick ups is 20 mm. The solid (black color) shape shown in the center of Figure 5.28b represents the Elettra 2.0 vacuum pipe.
An essential assumption in the practical assembly of this BPM is that the mechanical interface between the pick-up body and its housing on the BPM body is sufficiently tight to eliminate any residual gap through which the beam might lose energy.

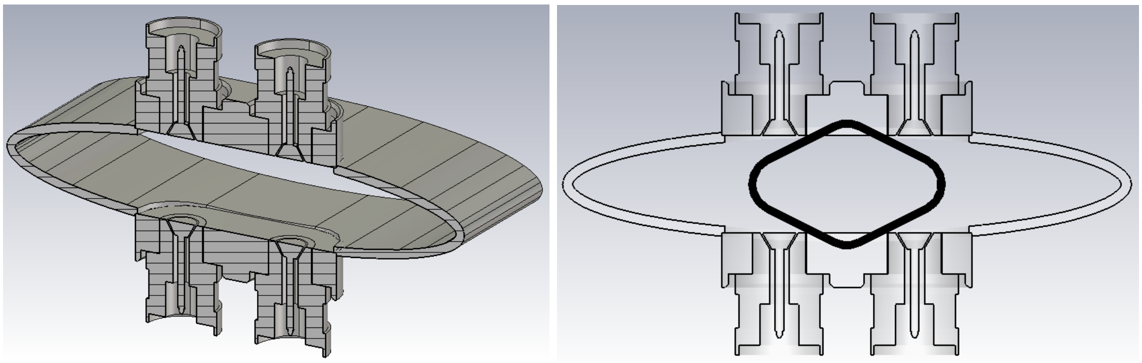
(a) (b)

Fig. 5.28 BPM prototype based on second generation pick ups: (**a**) 3D cut view, (**b**) cut view with overlapped the Elettra 2.0 vacuum pipe shape (solid line).

5.6.3 Electromagnetic simulations

The electromagnetic model of the complete BPM is shown in Figure 5.29a. In order to simplify the wakefield simulations, the pickup geometry is assumed "Zok" like (paragraph 5.6), as shown in Figure 5.29b. The gaussian bunch, propagating on axis, has 1 nC charge. Two values of the bunch length have been assumed in simulations to represent single bunch (SB) and multi bunch (MB) operating conditions of the Elettra storage ring. In SB, the bunch length varies as a function of the machine energy. For this reason, a value of $\sigma_{\mathrm{rms}} = 6$ mm has been selected as a compromise between the natural bunch length at 2.4 GeV, 6.6 mm, and that at 2 GeV, 5.1 mm. In MB, the bunch length is manipulated by tuning a superconducting third harmonic cavity (S3HC) [45] able to lengthen the stored bunches by about a factor of three with respect to the bunch length in SB. For this reason $\sigma_{\mathrm{rms}} = 18$ mm has been chosen for the MB wakefield simulation.

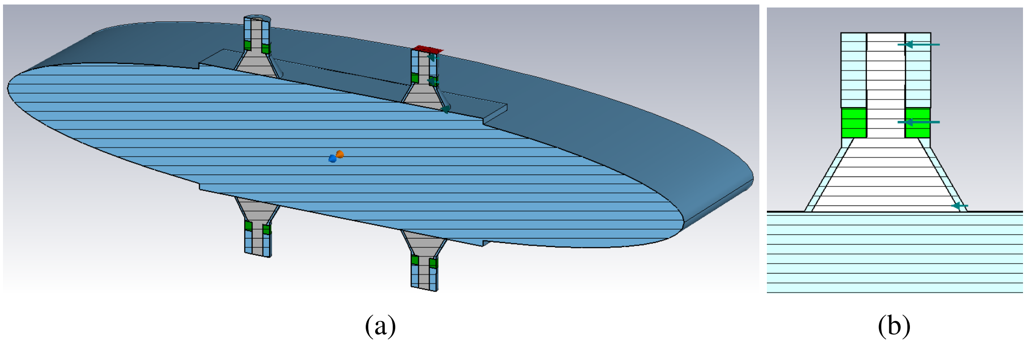

Fig. 5.29 Electromagnetic model of the low-gap elliptic BPM: (**a**) 3D cut view, (**b**) cut view of any pickup.

The aim of these numerical simulations is to provide reference insights into the characteristics of the beam-induced signal available at the RF connectors under ideal conditions. Such information serves as a benchmark, facilitating the interpretation of experimental data and supporting the validation of subsequent measurement procedures.
The SB simulation results are reported in the following four figures. Figure 5.30a shows the temporal evolution of the electric signal extracted through the pick-up RF port. Figure 5.30b shows the single sided corresponding spectrum. Figure 5.31a shows the evolution over space of the wake potential. Figure 5.31b reports the real and imaginary components of the longitudinal beam coupling impedance.

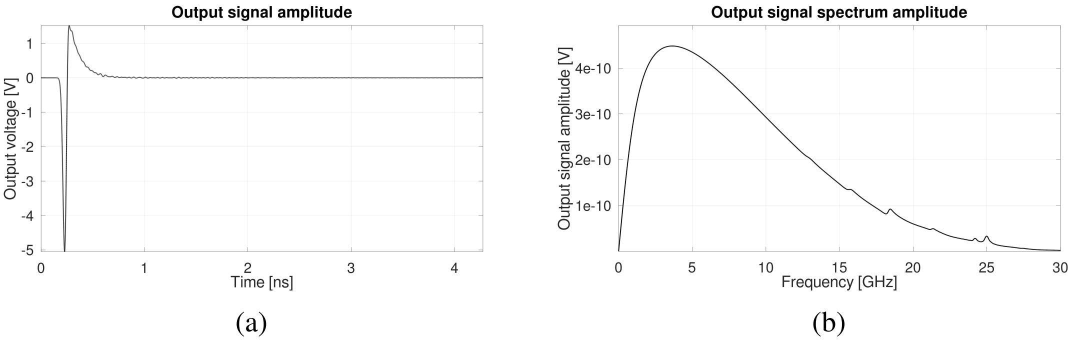

Fig. 5.30 Signal induced by the beam at the pick-up connector in the case of SB simulation: (**a**) time response, (**b**) frequency response.

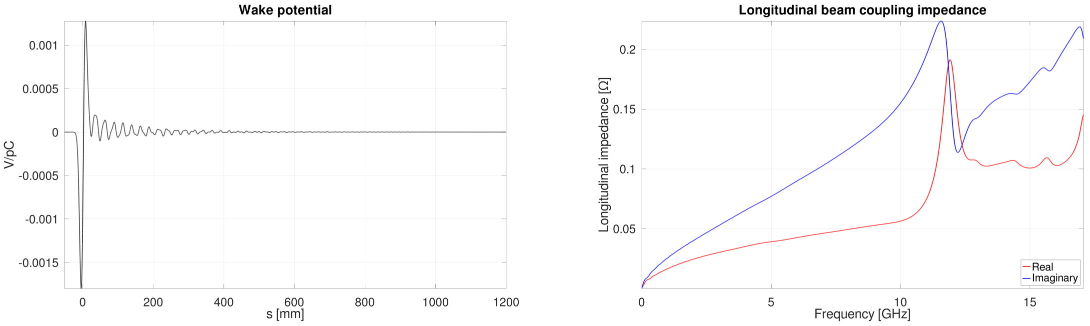

(a) (b)

Fig. 5.31 SB wakefield simulation results: (**a**) wake potential, (**b**) longitudinal beam coupling impedance components.

The MB simulation results are reported in the following four figures. Figure 5.32a shows the temporal evolution of the electric signal extracted through the pick-up RF port. Figure 5.32b shows the single sided corresponding spectrum. Figure 5.33a shows the evolution over space of the wake potential. Figure 5.33b reports the real and imaginary components of the longitudinal beam coupling impedance.

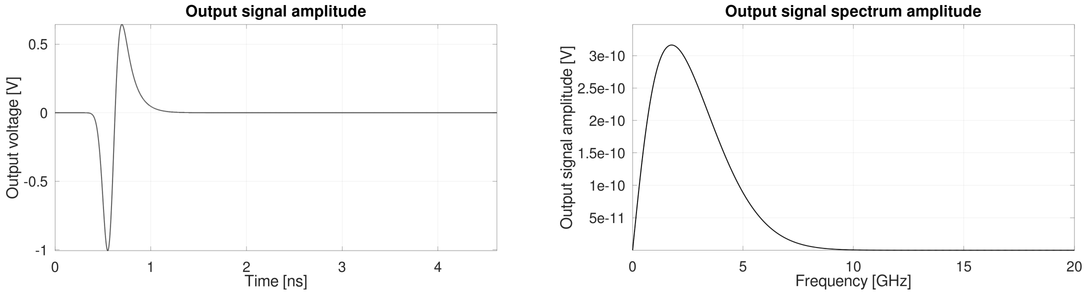

(a) (b)

Fig. 5.32 Signal induced by the beam at the pick-up connector in the case of MB simulation: (**a**) time response, (**b**) frequency response.

5.7 Real measurements in Elettra

Six machine physics shifts were dedicated to the acquisition of the signals generated by the BPM based on the second generation pick-ups. Single bunch, multi bunch and hybrid multi bunch operating conditions were set on Elettra. In each operating conditions the 4 pick up signals were acquired through a Tektronix DPO 72304DX oscilloscope (23 GHz analog bandwidth) at different sample rates. A short run (5 m long) of high quality cables (Sucoflex

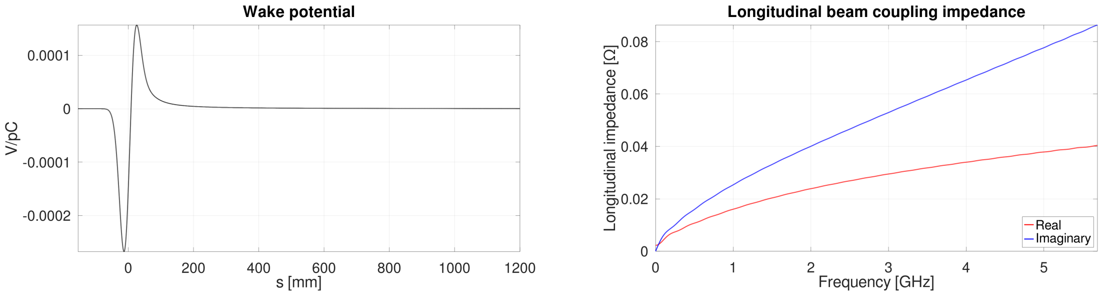

(a) (b)

Fig. 5.33 MB wakefield simulation results: (**a**) wake potential, (**b**) longitudinal beam coupling impedance components.

106, 18 GHz maximum operating frequency) was used to connect directly the pick ups to the oscilloscope.

Single bunch measurements

Single bunch (SB) measurements allowed to characterize the behavior of the BPM in "zero current" conditions, when the bunch current is so low that it is not able to excite collective effects. Taking into account that the Elettra's accelerating cavities frequency is 500 MHz, the relation between stored current and bunch charge in SB is:

$$\int_0^{T_{REV}} i(t)\,dt = Q_{SB} = I_{DCCT} \cdot T_{REV}$$

where T_{REV} is the revolution period of the single bunch (864 ns), Q_{SB} is the total charge stored in the single bunch and I_{DCCT} is the mean value (per revolution) of the current read by the current transformer. Four sets of measurements were performed at 0.3 mA, 1.0 mA, 2.1 mA and 3.0 mA, which correspond to, respectively, 0.26 nC, 0.864 nC, 1.8 nC and 2.6 nC. The generated signals were acquired at both 2 GeV and 2.4 GeV energies. Figure 5.34a shows the trend over a 5 ns acquisition window of the sampled pick-up voltages at 2.1 mA (2 GeV), together with the numerically calculated value at 1.16 mA (1 nC bunch charge). Figure 5.34b reports a detailed view of the same data in the [0.2 - 1.5] ns time window. The shape of the acquired signals is very close to the one numerically calculated. Regarding the signals' amplitude, the ratio between the measured and simulated signal amplitudes, around 1, does not follow the ratio between the measured (2.1 mA) and simulated (1.16 mA) currents, equal to 1.81. This discrepancy between measured and simulated signal amplitudes is due to the combination of the cables attenuation, the DCCT measurement error, the mechanical alignment errors of the BPM, the 'Zwr' type of RF connector used, and the difference between the effective SB bunch length and the one used for simulation.

Due to the bunch lengthening effect caused by machine impedances, doubling the bunch charge didn’t doubled the signal amplitudes.

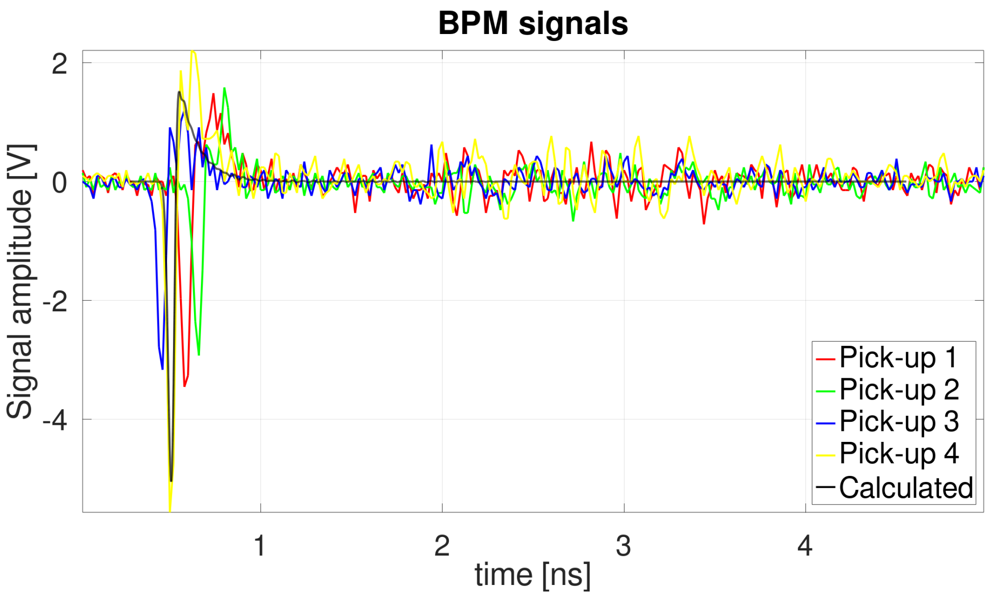

(a)

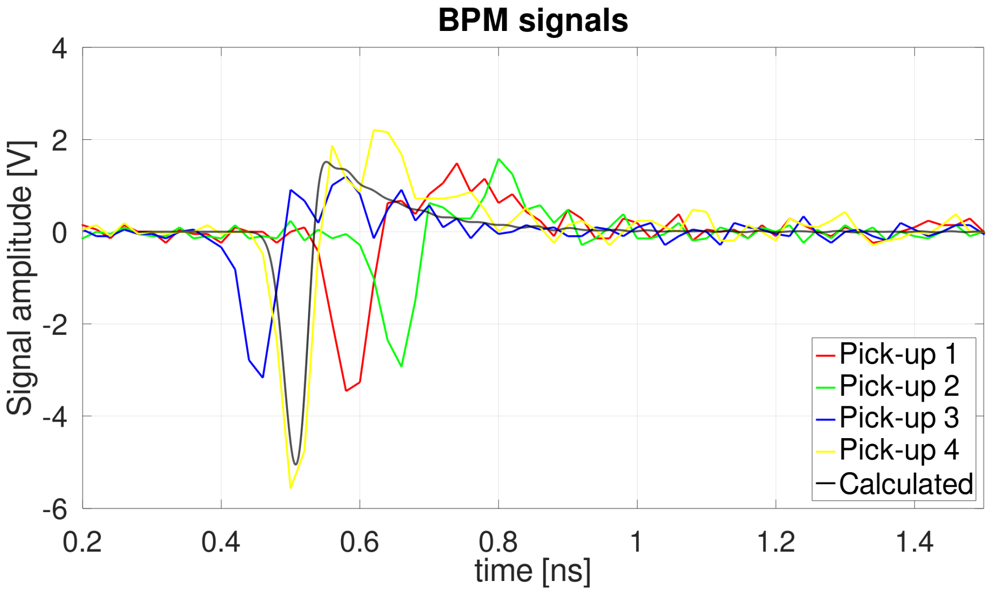

(b)

Fig. 5.34 Voltage signals acquired by the oscilloscope (single bunch current of 2.1 mA at 2 GeV: (**a**) 5 ns acquisition window, (**b**) detailed comparison between the acquired signals and the calculated one.

Multi bunch measurements

Figure 5.35a shows the MB beam signals acquired with 310 mA stored current at 2 GeV. Figure 5.35b reports a detailed view of the same data in the [1.6 - 3] ns time window, to which is added the calculated signal waveform (1 nC per bunch charge in simulation corresponds to 500 mA stored current). As seen in SB measurements, there are discrepancies between the amplitudes of the measured and simulated signals; the reasons are the same already mentioned.

Hybrid multi bunch measurements

The hybrid multi bunch operating mode (i.e. an extra charged isolated bunch is injected in the center of the dark gap, see Figure 5.36a) was used only for a quick check of the results already obtained in SB and MB. All the considerations made about the signals acquired in MB and SB were confirmed by hybrid operating mode. Due to insertion of 6 dB attenuators to protect the oscilloscope input stages, the waveforms reported in Figure 5.36 have to be rescaled by a factor of 2 to get their effective amplitude.

5.8 Conclusions about the second generation home made pickup

The second generation of pickup prototypes made it possible to perform real measurements in the Elettra storage ring, both in multi-bunch and single-bunch conditions. The comparison between the pickup signals obtained from measurements and those from wakefield simulations shows very good agreement in terms of time-domain waveform shape. The amplitude differences between simulation and measurements can be ascribed to various factors, including uncontrollable ones (e.g., alignment errors) and unavoidable effects such as signal attenuation due to propagation over long cable lengths. The signals extracted from the beam are suitable for use in real operating conditions.

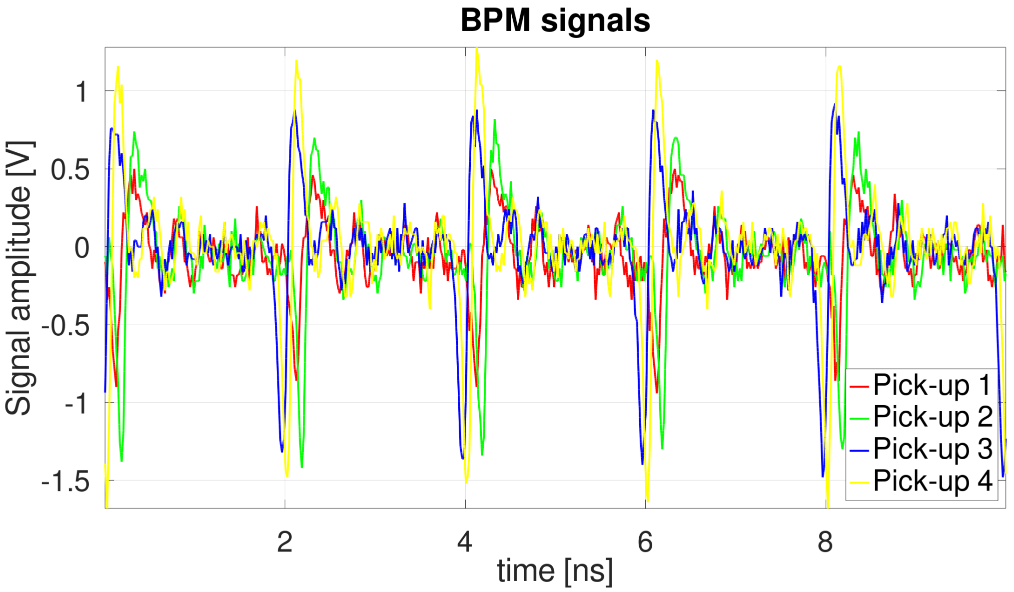

(a)

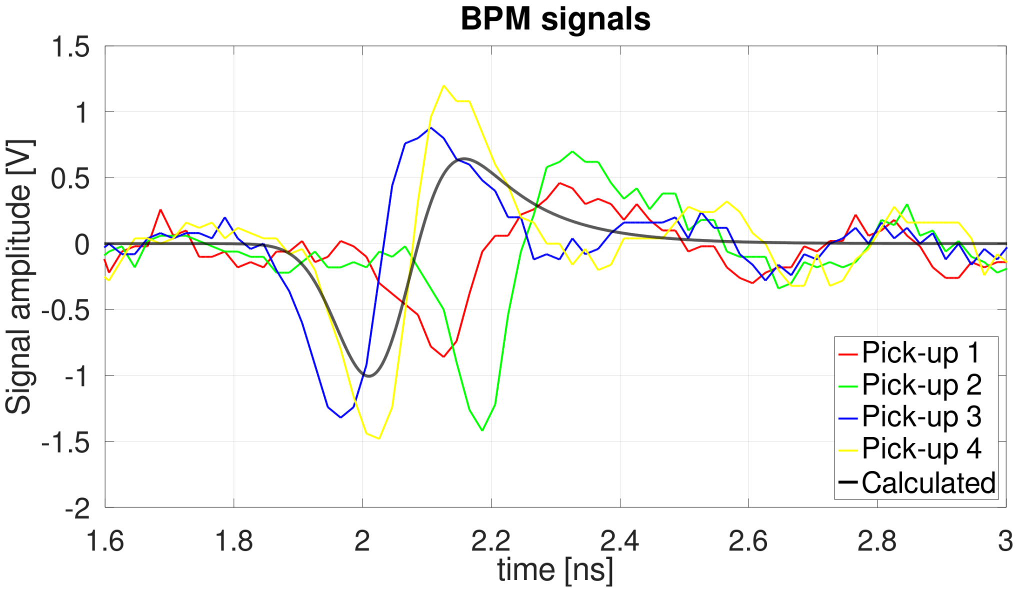

(b)

Fig. 5.35 Voltage signals acquired by the oscilloscope (310 mA stored current at 2 GeV): (**a**) 10 ns acquisition window, (**b**) detailed comparison between the acquired signals and the calculated one.

5.9 The Third Home Made Pick Up generation

5.9.1 Pick up structure

The third generation PU is shown in Figure 5.37.

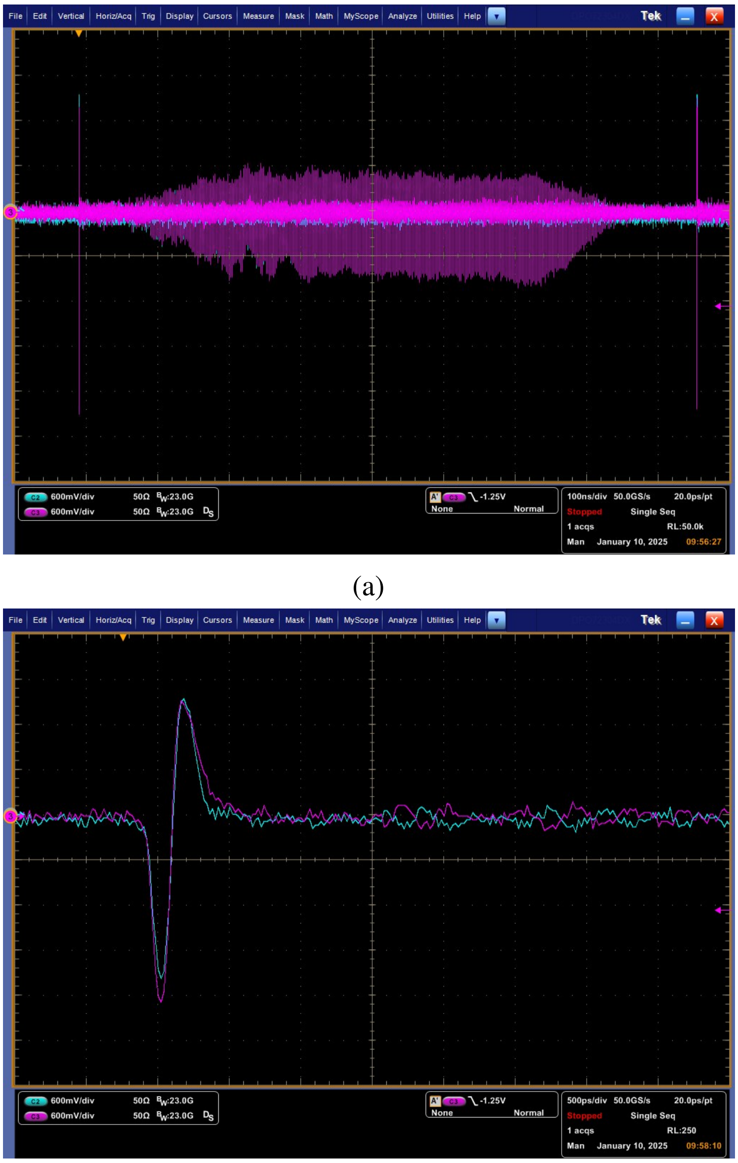

(a)

(b)

Fig. 5.36 Voltage signals acquired by the oscilloscope: (**a**) full storage ring filling pattern, (**b**) detailed acquisition of the bunch in the dark gap.

The materials, sealing technology, and overall design of the second generation have largely been retained. The RF connector has been modified by the incorporation of a metallic ring in direct contact with the pick-up body, thus constituting the outer sleeve portion of a complete K connector. The nominal thickness of the glue has been set at 2 mm in order to accommodate the greater length of the pick-up body. This adjustment is intended to ensure mechanical stability and coaxiality of the central pin with respect to the pick-up body. The bottom surface of the pick-up body is no longer coplanar with the surface of the conical

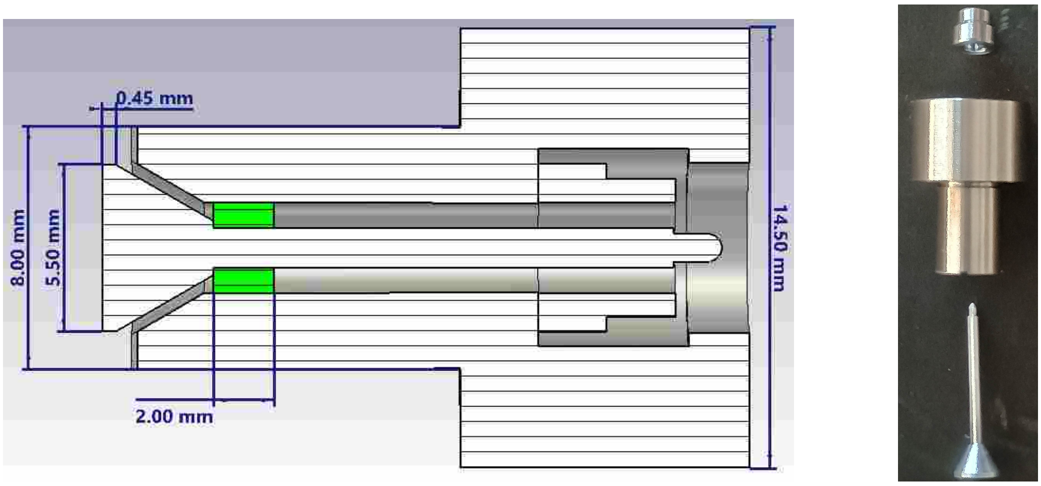

(a) Drawing of the third generation HMPU.

(b) Third generation HMPU before glueing.

Fig. 5.37 Third generation HMPU prototype

button exposed to the beam, indicating a modification in the relative alignment between the two components. The adoption of this markedly different design, relative to previous generations, is motivated by the need to eliminate the risk that any gap resulting from the mechanical mounting of the pick-up into the BPM body might be exposed to the beam. The assembly tool developed for this generation of HMPU is shown in Figure 5.38a. The four radial grooves visible on the surface of the pick-up body, see Figure 5.38b, are designed to assure vacuum pumping of the gap between the pick-up body and its housing.

(a) Empty assembly tool and pick-up components before assembling.

(b) Components mounted on the assembly tool during glue curing.

Fig. 5.38 Third generation HMPU prototype assembly tool

5.10 SMA sealing technology

The sealing mechanism between the pick-up body and the BPM body is now based on shape-memory alloy (SMA) technology [34], see Figure 5.39. The pick-up (PU) is positioned on its housing (H) on the BPM body (BB). An aluminum gasket (G) is then mounted around the housing (H) and the pick-up (PU). Finally, the SMA collar (C) is mounted to enclose the gasket (G). The particular feature of the material employed in the construction of the collar lies in its capacity to contract upon heating, maintaining the shape acquired at elevated temperature once returned to ambient conditions. Upon contraction, the collar compresses the gasket onto the pick-body and its housing. This process ensures that the components in contact are securely adhered together, thereby achieving ultra high vacuum tightness under operational conditions. Starting from room temperature, the collar has been heated up to 200 °C and then left cooling at room temperature.

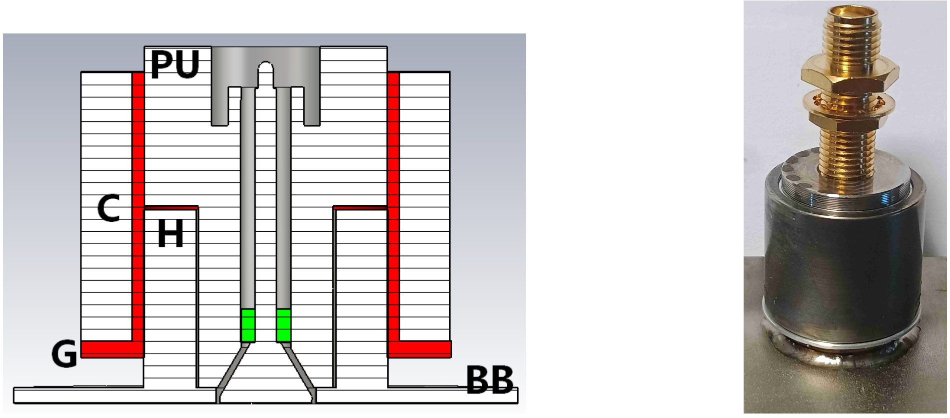

(a) Mounting scheme of the third generation pick-ups.

(b) Third generation pick-up mounted on BPM body.

Fig. 5.39 Third generation HMPU prototype

Given that bake-out is performed at around 250 °C, this sealing mechanism operates effectively without the need for the elevated temperatures typically associated with welding [13]. Another advantage of SMA technology is that the joint between the BPM body and each pick-up can be opened simply by cooling the SMA collar with liquid nitrogen. This feature is extremely useful when validating diagnostics equipment, especially button-type pick-ups. These can be easily replaced with other models by simply performing a thermal cycle and replacing the gasket.

5.11 EM characterization of the prototypes

To validate the behavior of the ten third-generation pick-up prototypes prior to mounting on the BPMs, they were measured in open air. An analysis aimed at providing an accurate comparison between the simulation results and the measured data was carried out on just one sample through 2PTF and 3PTF.

5.11.1 Open air measurements

As the time domain reflectometry results in open air closely resemble those already presented for the first and second generations, they are not reproduced here.

5.11.2 Test fixtures measurements

For the experimental measurements, a Teledyne LeCroy WavePulser 40iX was employed for time domain analysis (transmission and reflection up to 40 GHz).

3PTF measurements

The electromagnetic model used for simulations, both through CST and HFSS, is shown in Figure 5.40a. Figure 5.40b shows the pick-up mounted and locked on the 3PTF. Figure 5.42a reports the transmission coefficient S_{21}.

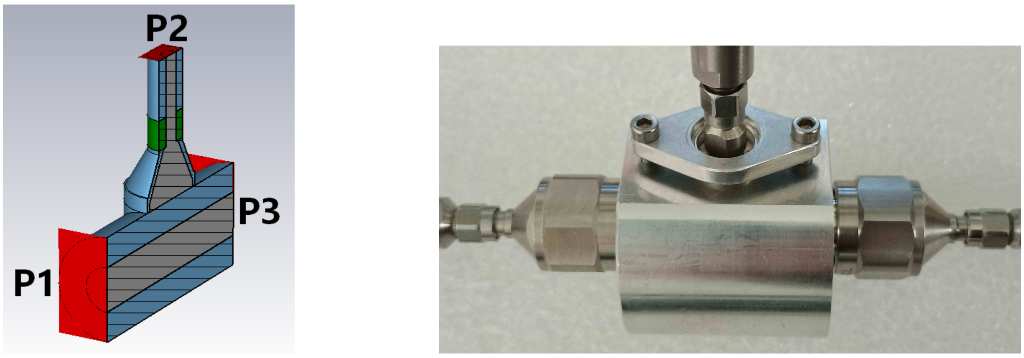

(a) (b)

Fig. 5.40 Third gen pick-up mounted on 3PTF: (**a**) electromagnetic model, (**b**) real device.

2PTF measurements

The electromagnetic model used for simulations, both through CST and HFSS, is shown in Figure 5.41a. Figure 5.41b shows the pick-up mounted on the 2PTF and secured in place by the fixing ring. Figure 5.42b reports the transmission coefficient S_{21}.

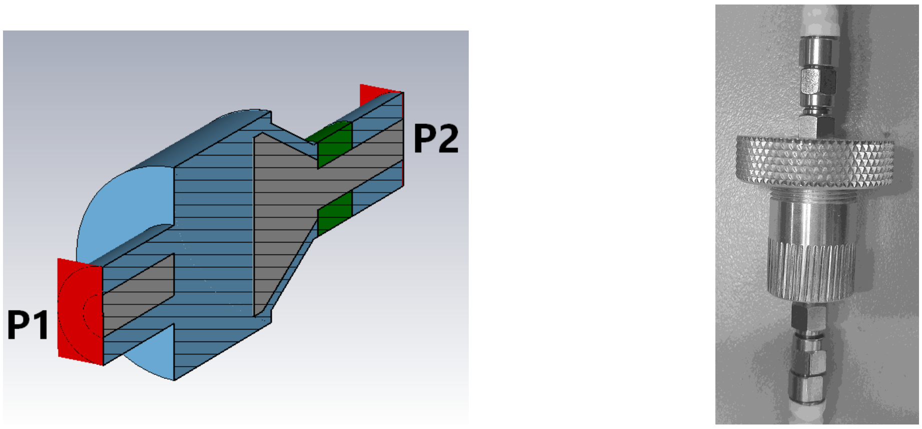

(a) (b)

Fig. 5.41 Third gen pick-up mounted on 2PTF: (**a**) electromagnetic model, (**b**) real device.

Considerations about measured results

A comparison of the simulated and measured frequency responses reveals a certain discrepancy, the causes of which may be ascribed both to inaccuracies in the assembly of the pick-up and to the limited accuracy in the knowledge of the relative permittivity ε_r. Simulations carried out with different values of ε_r exhibit a high degree of mutual consistency; however, none of them satisfactorily account for the experimental results. For this reason further investigations were performed through X-ray Computed Tomography (CT), see section 5.16.

5.12 The third generation BPM

The inner shape of the BPM body that hosts the third generation pick-ups is the same as the second generation. Due to the larger bulk imposed by the SMA collars, the distance between the pick-ups is greater than that of the second-generation BPMs. Its value, as measured between the centers of the button surfaces, is 24 mm along the horizontal axis. Measured in the same way, the vertical distance is 13.3 mm.

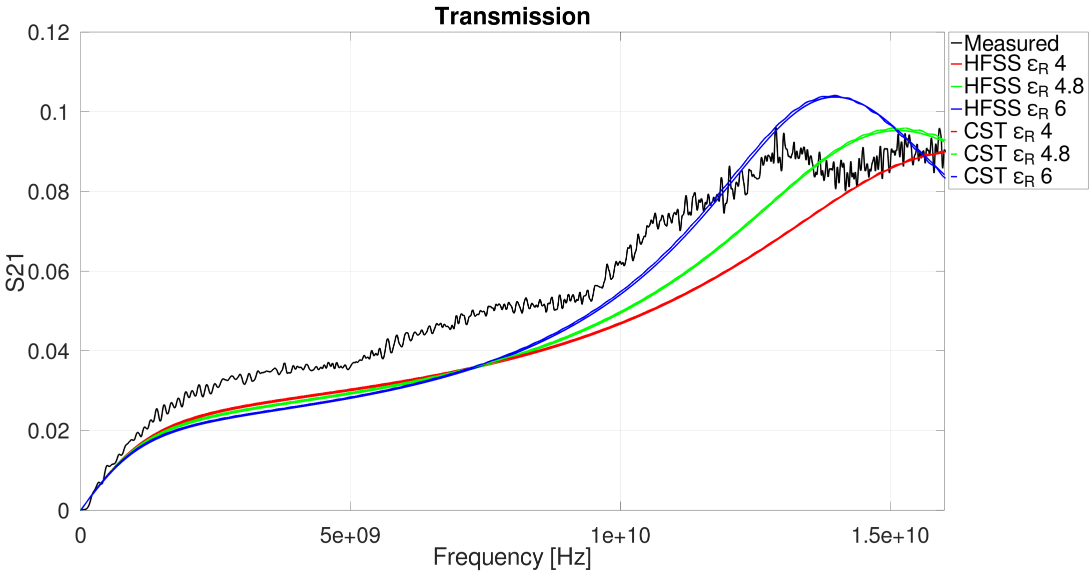

(a) S_{21} frequency response.

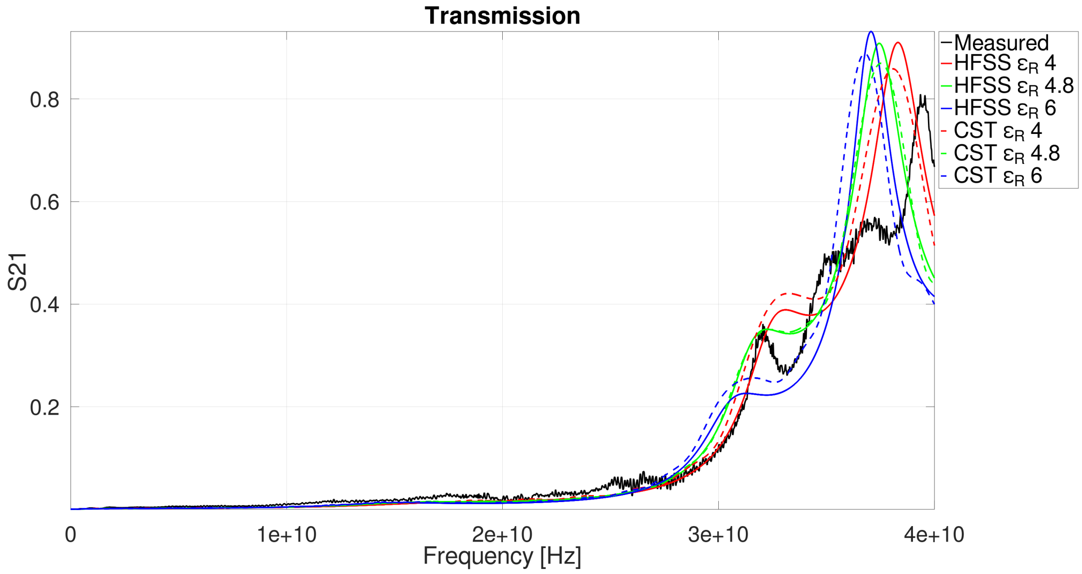

(b) S_{21} frequency response.

Fig. 5.42 Transmission measurements: (**a**) 3PTF up to 16 GHz, (**b**) 2PTF up to 40 GHz.

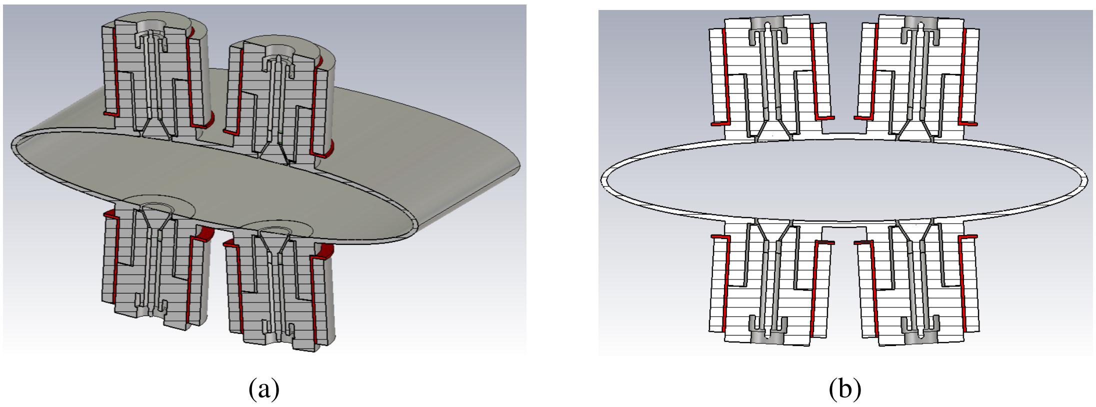
(a) (b)

Fig. 5.43 BPM prototype based on third generation pick-ups: (**a**) 3D cut view, (**b**) cut view.

5.13 Electromagnetic simulations

The EM model of the third generation BPM is shown in Figure 5.44. In order to compare the expected 'ideal' behavior with the measured response, two sets of wakefield simulations were carried out, assuming $\sigma_{\text{rms}} = 6$ mm (SB) and $\sigma_{\text{rms}} = 18$ mm (MB), respectively.

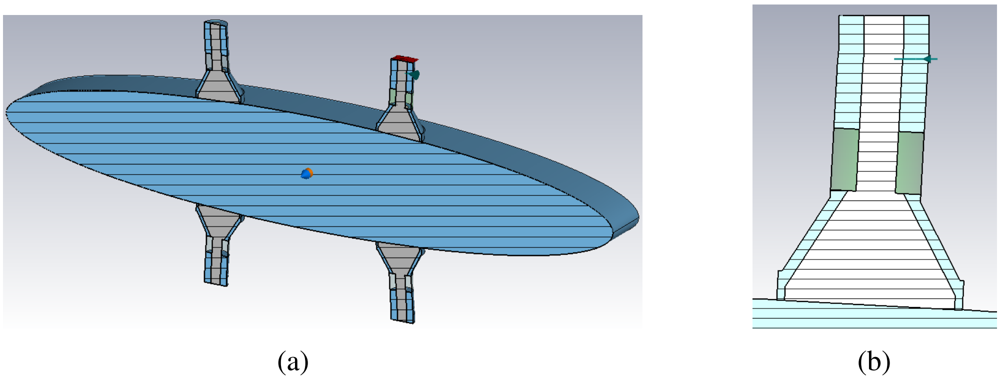
(a) (b)

Fig. 5.44 Electromagnetic model of the third generation BPM: (**a**) 3D cut view, (**b**) cut view of any pick-up.

The SB simulation results are reported in the following four figures. Figure 5.45a shows the temporal evolution of the electric signal extracted through the pick-up RF port. Figure 5.45b shows the single sided corresponding spectrum. Figure 5.46a shows the evolution over space of the wake potential. Figure 5.46b reports the real and imaginary components of the longitudinal beam coupling impedance.

The MB simulation results are reported in the following four figures. Figure 5.47a shows the temporal evolution of the electric signal extracted through the pick-up RF port.

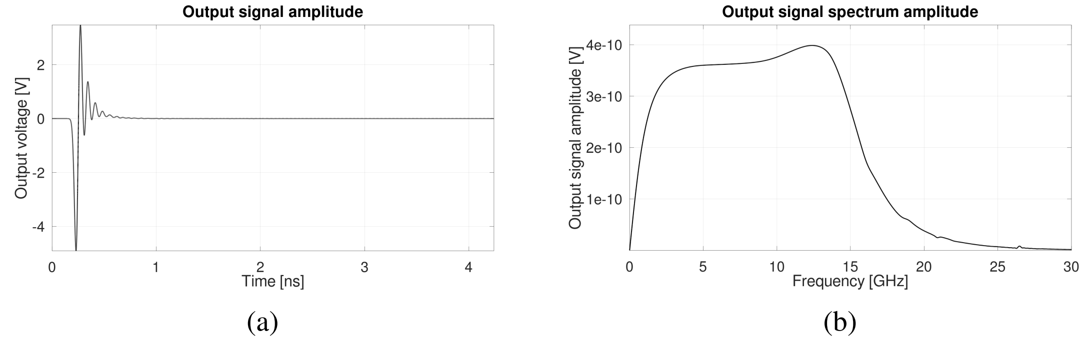

Fig. 5.45 SB output signal induced by the beam at the pick-up connector: (**a**) time response, (**b**) frequency response.

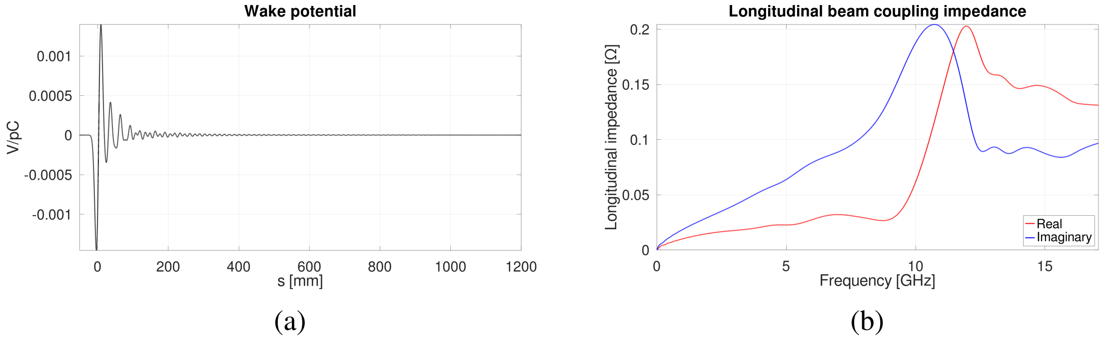

Fig. 5.46 SB wakefield simulation results: (**a**) wake potential, (**b**) longitudinal beam coupling impedance components.

Figure 5.47b shows the single sided corresponding spectrum. Figure 5.48a shows the evolution over space of the wake potential. Figure 5.48b reports the real and imaginary components of the longitudinal beam coupling impedance.

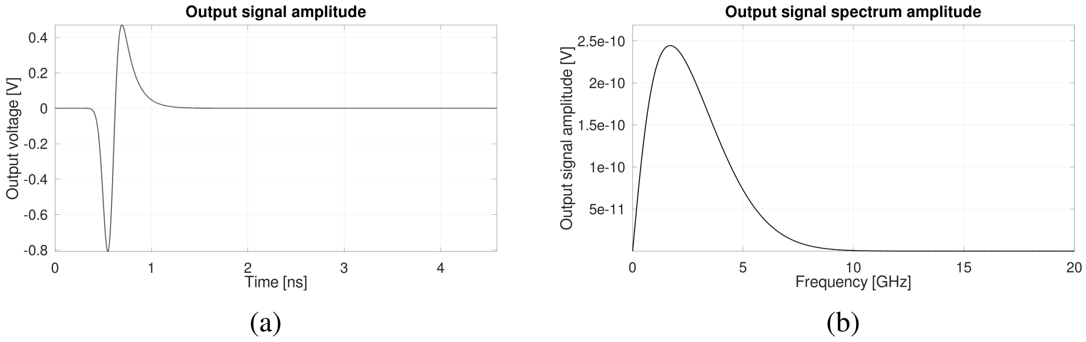

Fig. 5.47 MB output signal induced by the beam at the pick-up connector: (**a**) time response, (**b**) frequency response.

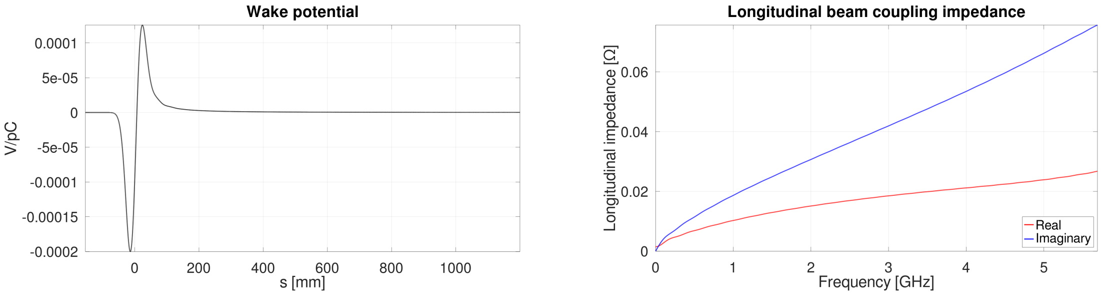

(a) (b)

Fig. 5.48 MB wakefield simulation results: (**a**) wake potential, (**b**) longitudinal beam coupling impedance components.

5.14 Comparison between second and third generation BPM numerical results

The main differences between the EM model of the second and third generation BPM are:

- the diameter of the pick-up, 5 mm versus 5.5 mm;
- the thickness of the glue, 1 mm versus 2 mm;
- the different shape of the terminal side of the conical electrode;
- the location of the pick-ups with respect to the symmetry axes of the vacuum pipe.

Given the reduced dimensions of the devices under investigation, the simulations were performed under the assumption of ideal materials. In this framework, the energy lost by the beam during its transit through the BPM is partially extracted through the pick-up RF ports and partially scattered back into the vacuum pipe. The loss factors calculated for a centered beam are reported in Table 5.1. An analysis of the spectral amplitude of the pick-up output signal allows the identification of the voltage corresponding to 500 MHz, as summarized in Table 5.2. Considering that the simulations carried out correspond to ’one-shot’ cases, i.e. aperiodic signals, the values presented in Table 5.2 need to be rescaled in order to determine the effective amplitude under periodic operating conditions. The transfer impedance values at 500 MHz are indicated in Table 5.3.

Table 5.1 Loss factor

Loss factor [V/pC]		
	SB ($\sigma_{\text{rms}} = 6$ mm)	MB ($\sigma_{\text{rms}} = 18$ mm)
BPM 2 gen	5.2×10^{-4}	8.7×10^{-5}
BPM 3 gen	4.0×10^{-4}	5.5×10^{-5}

Table 5.2 Output voltage amplitude at 500 MHz

Signal amplitude [V]		
	SB ($\sigma_{\text{rms}} = 6$ mm)	MB ($\sigma_{\text{rms}} = 18$ mm)
BPM 2 gen	1.60×10^{-10}	1.58×10^{-10}
BPM 3 gen	1.34×10^{-10}	1.30×10^{-10}

Table 5.3 Transfer impedance at 500 MHz

Transfer impedance [Ω]	
BPM 2 gen	0.080
BPM 3 gen	0.067

5.15 The third generation combined BPM

To perform comparative tests between different pick-ups, a 40 cm long low-gap vacuum chamber, hereafter referred to as the combined BPM (CBPM), was arranged to host three groups of pick-ups with vacuum sealing ensured by SMA collars, see Figure 5.49.

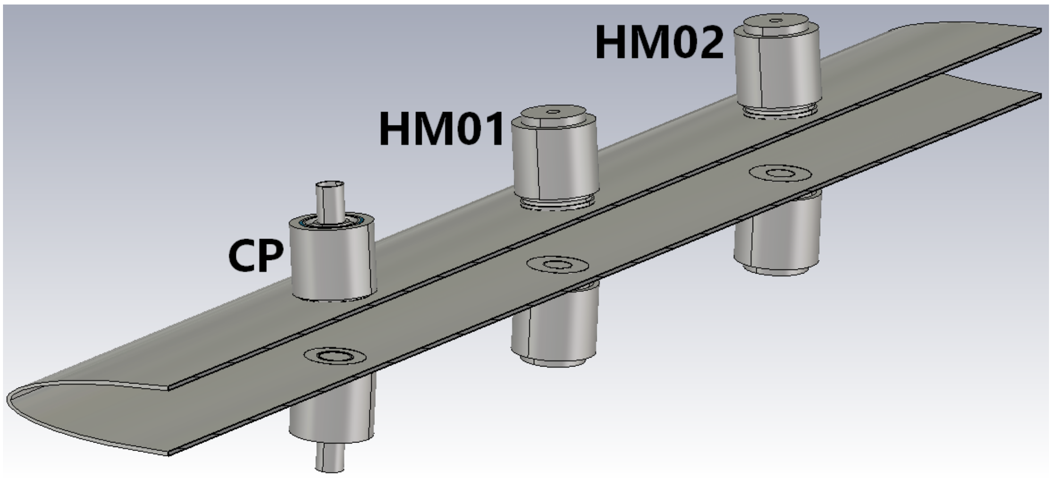

Fig. 5.49 Combined BPM with three groups of pick-up.

Two of these groups were assembled using eight third-generation pick-ups (HM01 and HM02), while the third group employed a set of four commercial pick-ups based on ceramic insulation (CP). The short spacing between the three groups, 10 cm, was deliberately chosen to ensure that the detected signals remained as comparable as possible between corresponding pick-ups. The drawback of this design choice lies in the potential risk of electromagnetic interference among the different groups of pick-ups, induced by wakefields. The internal geometry and dimensions of the CBPM are identical to those of the second-generation BPM. The principal objectives of the third-generation pick-ups and their associated BPM devices were, on the one hand, to compare beam-induced signals and the corresponding calculated beam positions across different families of commercial pick-ups, and on the other hand, to validate vacuum sealing through SMA technology. Figure 5.50 shows the CBPM mounted in the Elettra storage ring. As the beam propagates from left to right, it sequentially excites CP, then HM01, and finally HM02. Owing to the availability of two pre-existing BPMs connected to the flanges of the CBPM, a total of five measuring locations aligned along the same straight direction are provided. With respect to the beam propagation direction through the CBPM, the BPM located immediately upstream, designated LGin, is a low-gap type, while the BPM positioned immediately downstream, designated Rout, corresponds to the rhomboidal Elettra type. This configuration allows for a thorough cross-comparison of the characteristics of signals acquired using different types of BPMs.

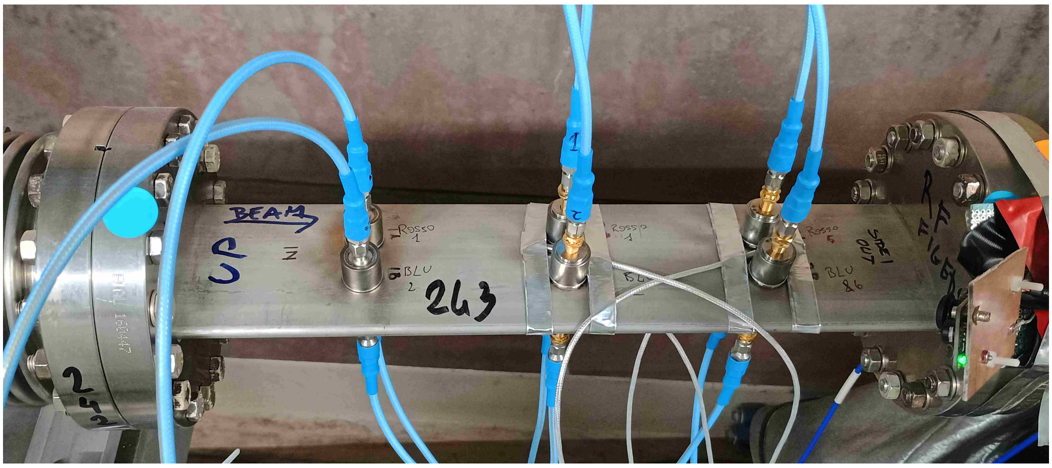

Fig. 5.50 BPM group with shape-memory alloy.

5.15.1 Measurements with real beam

Multi bunch and single bunch measurements were performed to check the ability of the third generation BPM to extract enough power from the beam to drive the RF front ends of the beam position detectors, see Figure 4.1. Indeed, aside from the specific differences between the BPMs currently operating at Elettra, and those under testing in view of Elettra 2, the acquisition electronics used to process the signals generated by the pick-ups are identical [9]. The unification of the position-processing electronics is enabled by the RF front end, which can accommodate a wide dynamic range of input signals, up to 60 dB. Through the regulation of its internal amplifiers and attenuators, the RF front end ensures that the signals supplied to the ADCs (analog-to-digital converters) are appropriately scaled to an optimum level, thereby enhancing the accuracy of the conversion process.

To carry out the comparison, the position (x,z) and sum (S) signals calculated by the position processors connected to LGin, CP, HM01 and Rout BPMs were logged at 280 mA, 2 GeV multi bunch machine operating conditions. The sum signal, equal to the sum of the numerical values of the four digitized voltages, is proportional to the beam current. The particular proportionality coefficient relating this signal to the calibrated measurement expressed in units of current is determined by the specific geometry of the BPM. Through adjustments to the attenuator settings of RF front ends, it was possible to scale the calculated sum signals to values that were mutually consistent. Consequently, the proportionality coefficients were empirically established, ensuring that the sum signals of the four BPMs under comparison produced nearly equivalent readings. The comparison between the sum data obtained in two different top-up working conditions is shown in Figure 5.51. Due to the absence of a common trigger in the logger system, which records continuously over time and delivers the results to a software data-capturing interface, the four traces are not synchronized. Nonetheless, the time traces exhibit consistent behavior throughout the measurement period. The lack of calibration in terms of current units is represented in the graphs by arbitrary units (a.u.).

Single-bunch measurements carried out under machine conditions comparable to those applied for the second-generation BPM confirmed that the third generation exhibits a similar behavior.

Figure 5.52 shows the latest measurement acquired with the third-generation BPM to characterize the pickup signals under exotic storage-ring filling patterns, such as that foreseen for operation with transverse deflecting cavities [17], where one out of every two buckets will be populated with electrons.

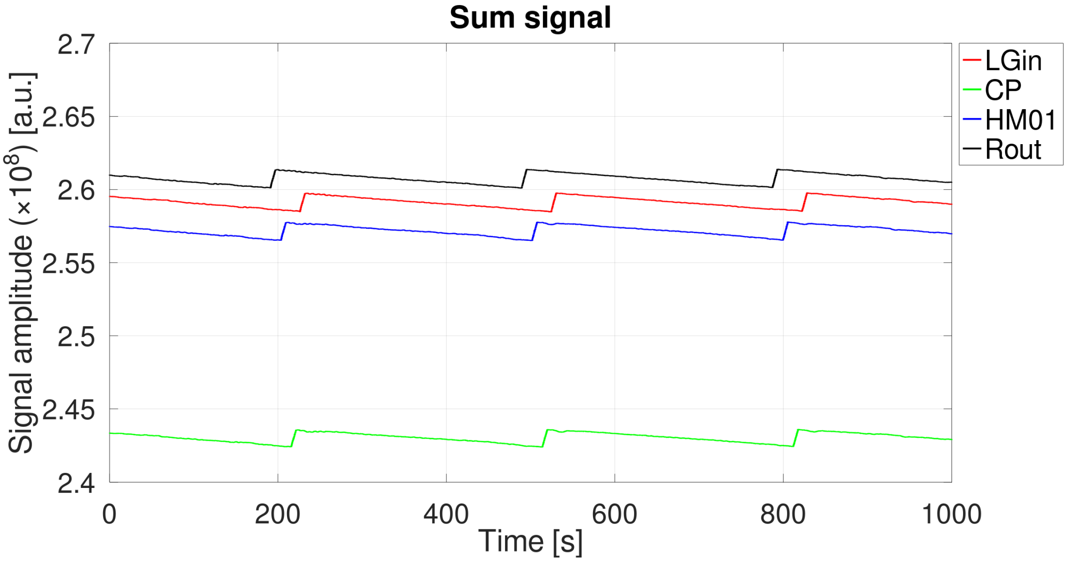

(a)

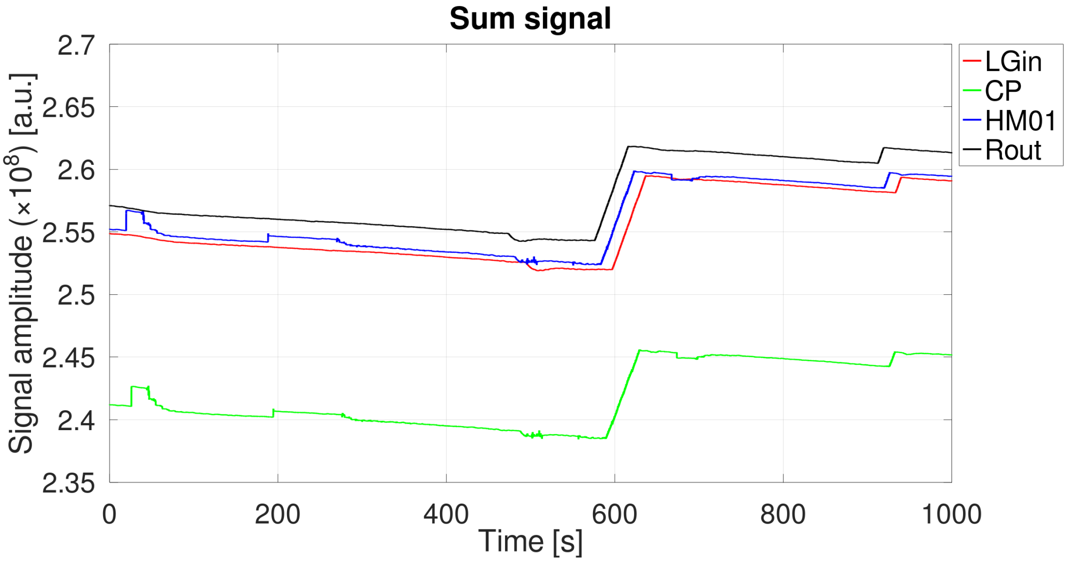

(b)

Fig. 5.51 Sum signals calculated for the four BPMs under comparison: (**a**) current refill injection every 300 s, (**b**) current refill injection on demand.

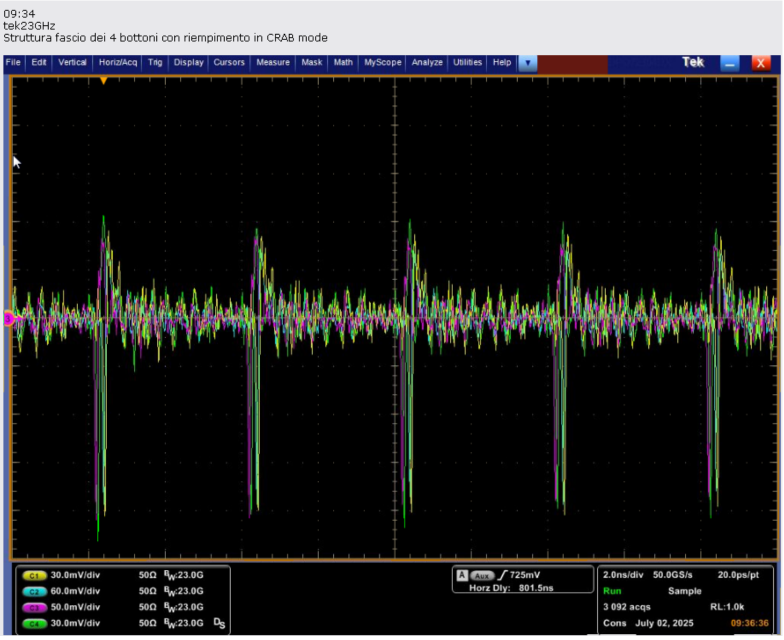

09:34
tek23GHz
Struttura fascio dei 4 bottoni con riempimento in CRAB mode

C1 30.0mV/div 50Ω BW:23.0G
C2 60.0mV/div 50Ω BW:23.0G
C3 50.0mV/div 50Ω BW:23.0G
C4 30.0mV/div 50Ω BW:23.0G DS

725mV
Horz Dly: 801.5ns

2.0ns/div 50.0GS/s 20.0ps/pt
Run Sample
3 092 acqs RL:1.0k
Cons July 02, 2025 09:36:36

Fig. 5.52 The last measure performed on Elettra (July, 2^{nd}, 2025): characterization of the fill pattern foreseen for operation with transverse deflecting cavities.

5.16 Computed tomography scan

Following its electromagnetic characterization through 2PTF and 3PTF measurements, see section (5.11.2), the third-generation pickup sample was further analyzed using X-ray computed tomography scanning [19]. The information derived from the CT images, which captures the real internal structure of the pickup, can thus be compared with the electromagnetic model used in simulations, which in turn is based on the mechanical model.

A set of selected images is presented in Figure 5.53, providing a visual illustration of the results. Compared to the nominal drawing, see Figure 5.37, three types of anomalies can be identified:

- the distribution of the glue is non-homogeneous. The defects range from bubbles, as in details A, C and E, to extended void regions, such as D, B and G;
- as illustrated in F, glue can be observed within the gap between the conical button and the pick-up body.;
- the glued region exhibits an axial length exceeding 2 mm.

These anomalies are sufficient to account for the differences in electromagnetic behavior between simulation and experiment.

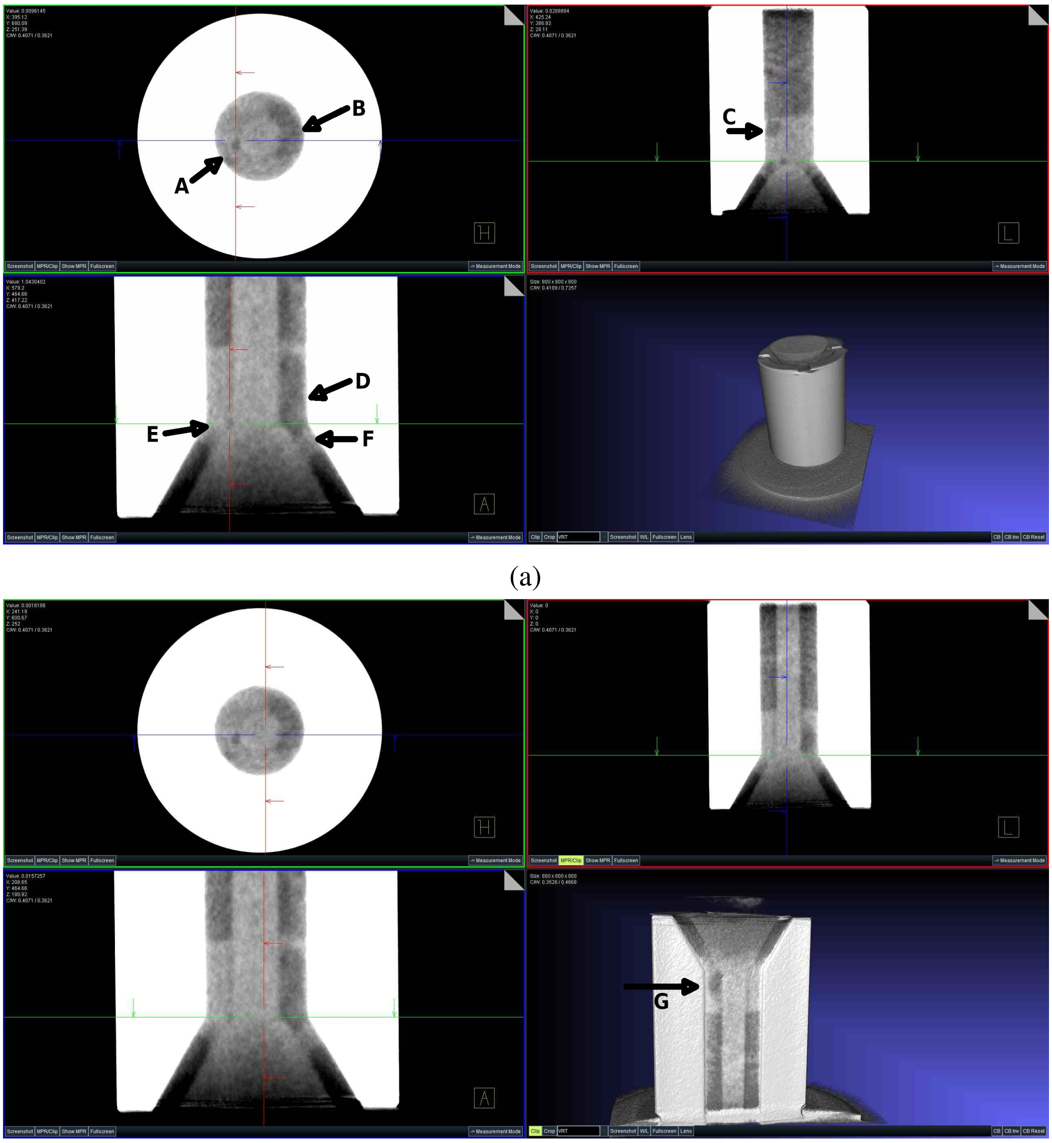

(a)

(b)

Fig. 5.53 CT images of the third generation pickup prototype (courtesy D. Dreossi): (**a**) defects detected in the internal glue filling, (**b**) defects detected in the internal glue filling.

5.17 Conclusions about the third generation home made pick up

Through the third-generation pickup prototypes, two further important milestones in the development of the BPMs for Elettra 2.0 were achieved:

- validate the complete BPM signal acquisition chain, from the pickup signals to the calculated beam positions (and ancillary information, e.g., the sum signal) delivered through the control system. The excellent results obtained varying the attenuators on the RF front ends demonstrate that the beam position acquisition system shown in Figure 4.1 is ready for Elettra 2.0.

- validate the SMA vacuum-sealing technology, which is expected to be adopted for the BPMs dedicated to diagnostics-specific operations. This approach allows the pickups to be replaced with different types, selected according to the specific function they are required to fulfill.

5.18 The Fourth Home Made Pick Up generation

The fourth generation has been designed to improve the quality of the electrical contact between the outer sleeve of the K connector and the pick-up body. In addition, the external geometry of the pick-up has been modified to incorporate a welding lip, thereby ensuring ultra-high vacuum tightness once welded to the BPM body. The corresponding drawing is presented in Figure 5.54. The portion of the pick-up facing the beam has been maintained with the same dimensions as in the third generation, while its overall length has been adopted from the second generation. The cylindrical sleeve is press-fitted onto the pick-up body in order to ensure both high-quality electrical contact and a secure mechanical connection. Through this mechanical design, the K connector embedded within the pick-up is guaranteed to operate reliably over its nominal bandwidth.
Several prototypes of this generation were manufactured in-house to assess through 2PTF and 3PTF test fixtures their electromagnetic behavior as a function of the insulation-ring dimensions and material.

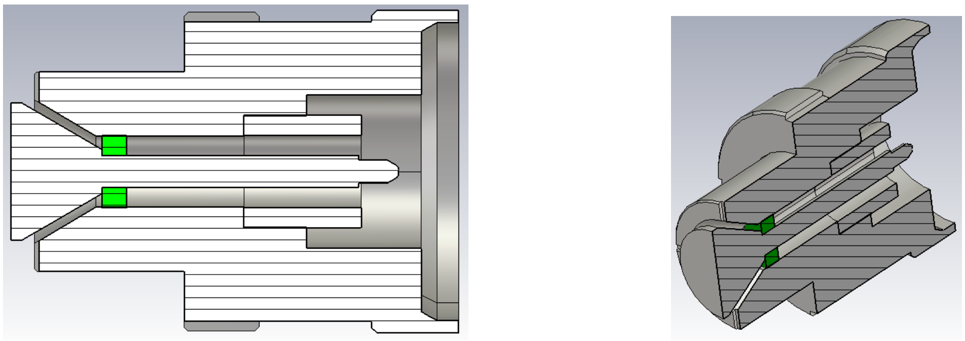

(a) Drawing of the fourth generation HMPU. (b) Fourth generation HMPU 3D cut view.

Fig. 5.54 Fourth generation HMPU prototype

5.19 Conclusions

The long path from theory, discussed in Chapter 4, to practical implementation, addressed in the present chapter, required adapting the theoretically derived pickup shapes and materials to real, manufacturable designs. The first major challenge encountered was the extremely long delivery time for any type of prototype from external manufacturers, which was incompatible with the Elettra 2.0 project schedule. For this reason, several prototype sets were fabricated in-house to allow a rapid validation of their electromagnetic design based on measurable characteristics. The first generation of home-made pickups demonstrated, both in laboratory tests and during operation in the Elettra pre-injector, that their performance was sufficiently good to justify investing in the design of a second generation tailored to the vacuum-pipe dimensions of Elettra 2.0. The second generation of home-made pickups was tested in laboratory conditions as well as during operation on the Elettra storage ring. The measured performance showed good agreement with the predictions of the numerical simulations. A third generation of home-made pickups was designed to evaluate an innovative vacuum-sealing technique employing shape-memory alloys (SMA). This technology enables the pickup body to be sealed to the BPM body by heating the mating components to a temperature significantly lower than that used in conventional welding. A dedicated test setup employing SMA sealing was implemented to compare the performance of two BPMs using third-generation prototypes with that of a BPM equipped with commercial pickups. The results obtained were excellent, providing the opportunity to test under real operating conditions the full beam position acquisition and processing system that will be used for Elettra 2.0. The fourth generation of pickups ultimately constitutes the reference design submitted to the manufacturing companies for series production.

Chapter 6

The First ELETTRA 2.0 pick up prototypes

6.1 Introduction

The practical realization of the fourth generation of homemade pickups allowed the quick validation of their electromagnetic design. However, it did not address the issue of their long-term reliability under ultra high vacuum conditions. This limitation could potentially be overcame by improving the bonding process between the pickup electrode and the pickup body. Due to time constraints, it was decided not to investigate this issue further at this stage. As a consequence, the construction of the complete series of pickups for Elettra 2.0 must rely on traditional glass-metal or ceramic-metal vacuum sealing technologies. Glass is the preferred option in terms of RF performance, as described in Chapter 4. Moreover, the reduced dimensions of the pickups further support the adoption of glass, since brazing ceramic components of such small size involves significant manufacturing constraints and, consequently, higher costs. Several vacuum feedthrough manufacturers were consulted to identify at least one capable of delivering the final components using established assembly and sealing technologies. The baseline reference design provided to each manufacturer corresponds to the technical drawing of the fourth-generation pickup.

At the time of writing, the final pickup designs had been fully defined in collaboration with three companies. Two of them employ glass for vacuum sealing, while the third one uses ceramic. The first design to be approved chronologically has recently been manufactured. Based on glass sealing technology, the first 16 prototypes have successfully passed both factory acceptance tests (FAT) and site acceptance tests (SAT). The electromagnetic SAT results are reported in the following paragraphs.

6.2 The first 16 prototypes

Starting from the reference design drawing proposed by Elettra - Sincrotrone Trieste, the company responsible for manufacturing the first 16 prototypes refined the final drawing of the pickup design to accommodate the manufacturing constraints imposed by its specific production process. The materials used for the construction of the pickups are molybdenum for the electrode, AISI 316L for the housing, glass for vacuum insulation and mechanical support of the electrode. The thickness of the glass, originally set to 1 mm in the reference design, was increased to approximately three times this value to comply with the maximum allowable leak rate for Elettra 2.0 (see Chapter 5 for further information on vacuum specifications). The mechanical interface between the pickup body and the collar defining the reference plane of the K connector was also modified by the company. This modification does not introduce any issues, as it does not alter the geometry of the coaxial line that delivers the beam-induced signal to the K connector.

6.3 Electromagnetic validation

To reliably and repeatably validate the electromagnetic behavior of these pickup prototypes, two sets of RF measurements were performed. These measurements were carried out using two types of test fixtures: a three-port test fixture (3PTF) and a two-port test fixture (2PTF). Each set of measurements was further subdivided into time domain and frequency domain measurements:

- Time domain measurements were performed using a Teledyne Lecroy WavePulser 40iX high-speed interconnect analyser (TDR/TDT), with a bandwidth of 40 GHz;
- Frequency domain measurements were carried out using a Keysight PNA-X network analyser (VNA), with a bandwidth of 26.5 GHz.

Even though the bandwidth provided by the 3PTF, 16 GHz, is adequate for the characterization of the pickups, additional measurements were carried out up to 40 GHz with the 2PTF. This extended band makes it possible to assess the similarity of the pickups' behavior up to the maximum operating frequency of the K-connector.

Hereafter, the term 'measuring instrument' will be used to refer collectively to both TDR/TDT and VNA devices, with the specific type always identifiable from the context.
Some of the measurements shown in the following figures yield unphysical results (e.g. reflection scattering parameters exceeding unity). These occurrences are tolerated as they stem from uncalibrated yet rapid measurement procedures, particularly in the time domain,

and do not compromise the overall objective of validating the first 16 prototypes. In the context of the forthcoming production of 900 pickups for the BPMs of Elettra 2.0, the RF measurements are primarily intended to verify, quickly and reliably, that all pickups exhibit consistent behaviour within an acceptable dispersion range centred around a realistic mean value. This ensures that similar, ideally identical, pickups will be welded onto each BPM body.

6.4 3PTF based electromagnetic tests

The three-port test fixture is shown in Fig. 5.3. Port 2 of the measuring instrument is connected to the pickup under test, while the remaining two ports are connected to other two ports of the measuring instrument. Consequently, the reflection characteristics of each pickup are represented by the S_{22} scattering parameter.

Owing to the symmetry of the 3PTF, its two coaxial line ports can be connected interchangeably to port P1 and port P3 of the measuring instrument without affecting the measurement results. Therefore, the coupling between each coaxial line connector of the 3PTF and the pickup connector can be characterized by either the S_{21} or S_{23} scattering parameter, which are numerically identical. For this reason, only S_{21} is represented in the following pictures.

A further advantage of the 3PTF symmetry is that it can also be used with a a two-port measuring instrument by terminating one of the coaxial line ports with a matched load. In this configuration, only the S_{21} and S_{22} scattering parameters can be measured.

In order to obtain a minimal statistical characterisation of the RF behaviour of the prototypes, the mean value and standard deviation have been calculated for each set of S_{21} and S_{22} measurements. Although the maximum nominal operating frequency of the 3PTF is 16 GHz (see Chapter 5), the full band of the VNA has been used for preliminary evaluations. Time domain measurements, on the other side, have been always carried out at the maximum bandwidth of the TDR/TDT instruments, even when the plot data have been shown up 16 GHz.

6.4.1 VNA measurements

Measure bandwidth 26.5 GHz

Figure 6.1a and Figure 6.1b show the S_{21} and S_{22} scattering parameters, respectively, as measured with the VNA up to 26.5 GHz. The standard deviation computed over the population of 16 pickup prototypes is shown in Figure 6.2a for S_{21} and Figure 6.2b for S_{22}.

By comparing the frequency responses of the individual pickup, it can be observed that:

- The S_{21} curves are in very good agreement up to approximately 18 GHz. Above this frequency, higher-order modes in the coaxial line are excited.
- A pronounced dispersion peak is observed in the S_{21} curves around 22 GHz.
- With the exception of the peak near 22 GHz, the S_{22} measurements are more dispersed than the corrisponding S_{21} results.

Measure bandwidth 16 GHz

Figure 6.3a and Figure 6.3b show the S_{21} and S_{22} scattering parameters, respectively, measured with the VNA up to 16 GHz, which corresponds to the nominal operating frequency range of the 3PTF. Within this frequency span, only the fundamental TEM mode is able to propagate. In order to get high quality measurements, the VNA has been calibrated over 16000 points uniformly distributed across the band, just before to start the measurements on the prototypes.

The corresponding standard deviation is shown in Figure 6.4a for S_{21} and Figure 6.4b for S_{22}.

Detailed view of the 400 MHz - 1.6 GHz frequency band

The center frequency of the RF detectors used in Elettra 2.0 to determine the beam position is 500 MHz. A second group of detectors, employed in the longitudinal and transverse multi bunch feedback systems, operates at 1.5 GHz. For these reasons, it is mandatory that the pickups exhibit nearly identical behavior, at least in the vicinity of these two frequencies.

Figures 6.5a and 6.5b show the S_{21} and S_{22} scattering parameters, respectively, measured with a VNA in the 400 MHz–1.6 GHz frequency band. As shown in Figure 6.6a for S_{21} and Figure 6.6b for S_{22}, the dispersion of the pickup characteristics is very small for both transmission and reflection.

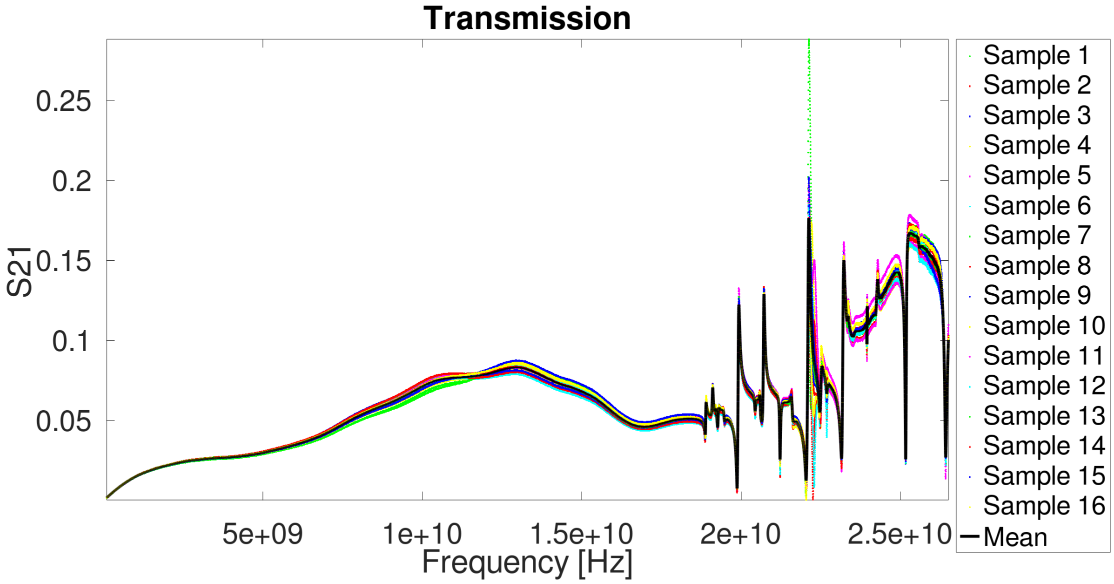

(a) S_{21} frequency response.

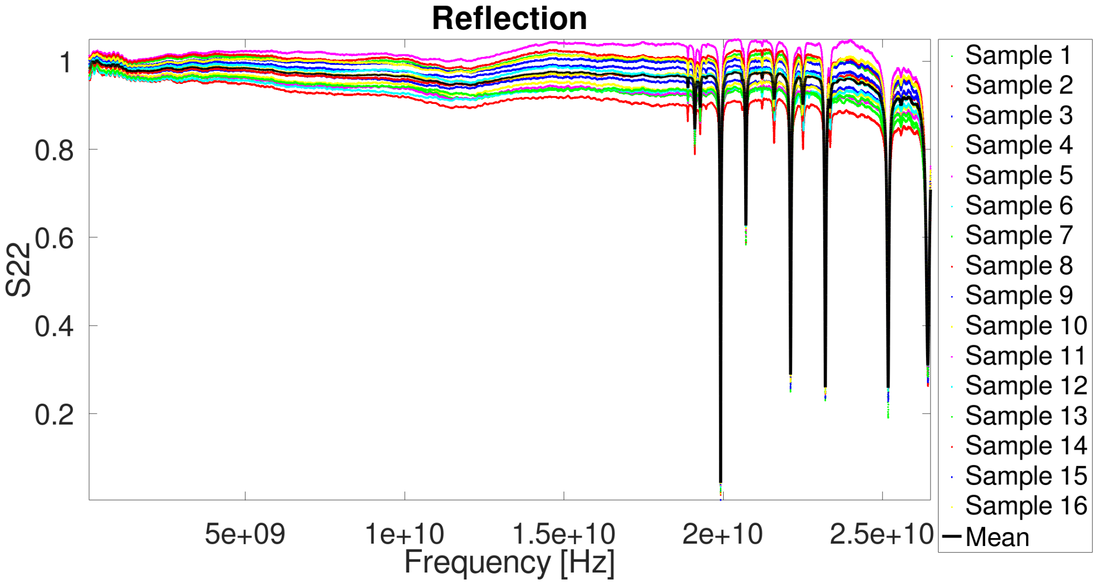

(b) S_{22} frequency response.

Fig. 6.1 3PTF: S_{21} and S_{22} frequency responses up to 26.5 GHz measured by VNA.

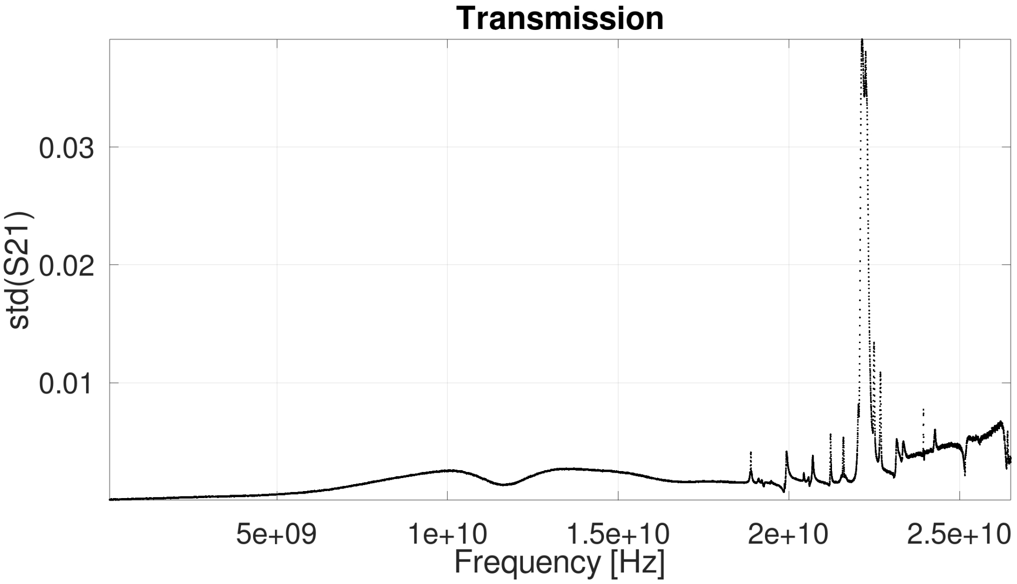

(a) S_{21} standard deviation.

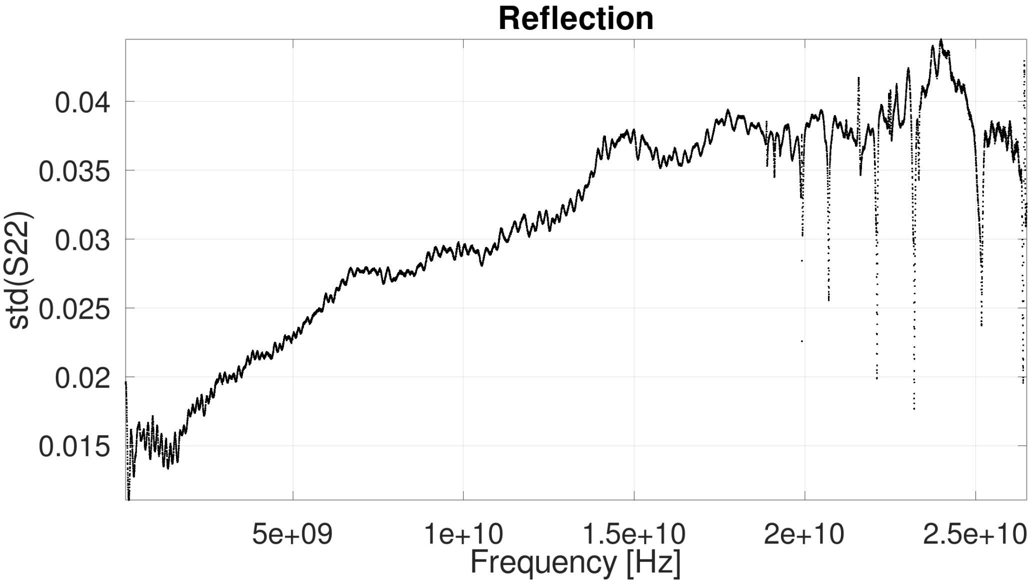

(b) S_{22} standard deviation.

Fig. 6.2 3PTF: standard deviation of S21 and S22 up to 26.5 GHz in the case of VNA measurement.

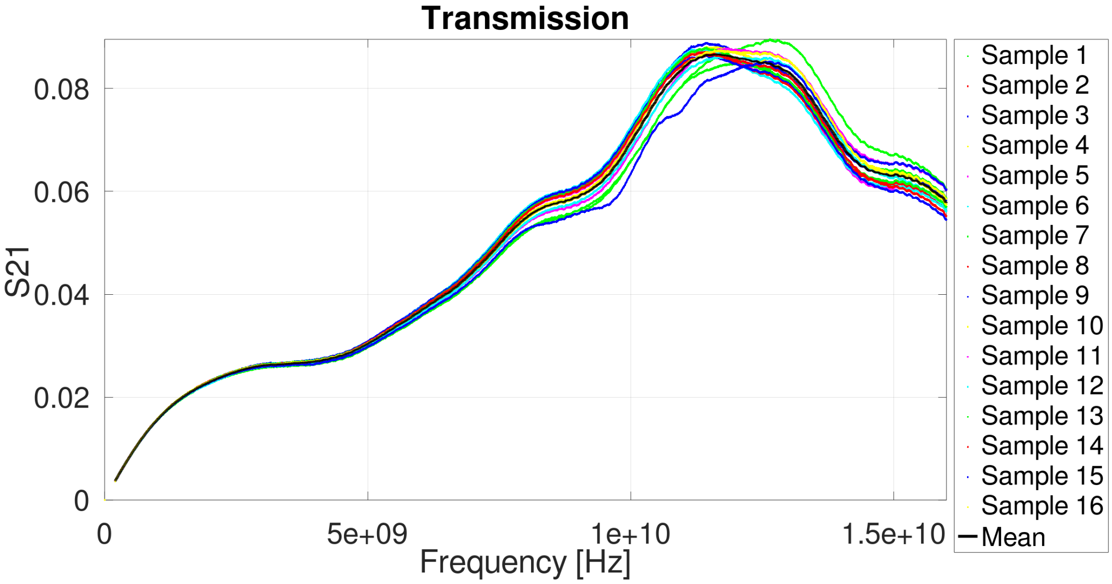

(a) S_{21} frequency response.

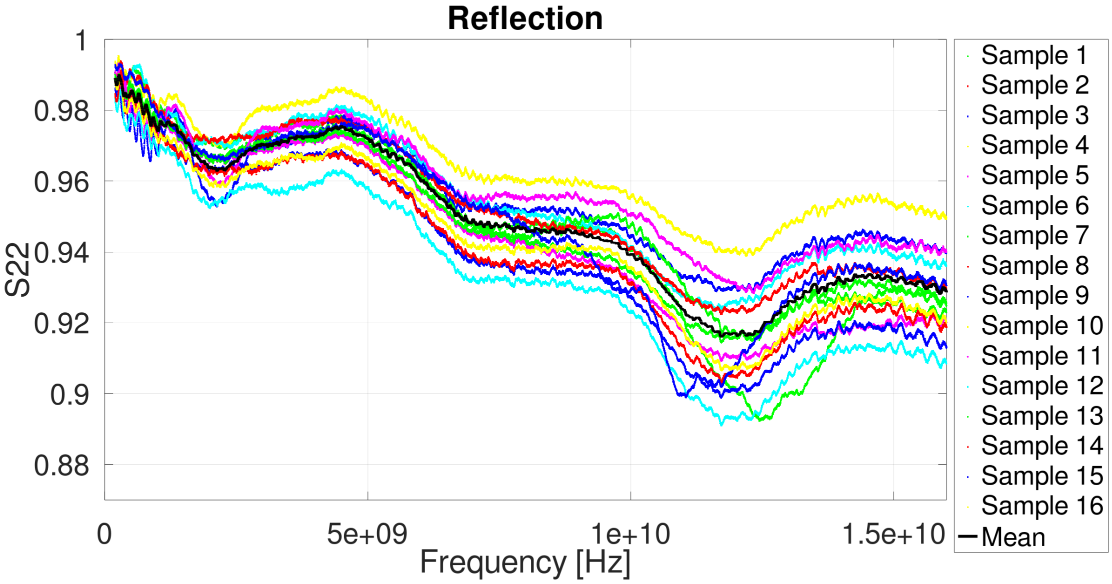

(b) S_{22} frequency response.

Fig. 6.3 3PTF: S_{21} and S_{22} frequency responses up to 16 GHz measured by VNA.

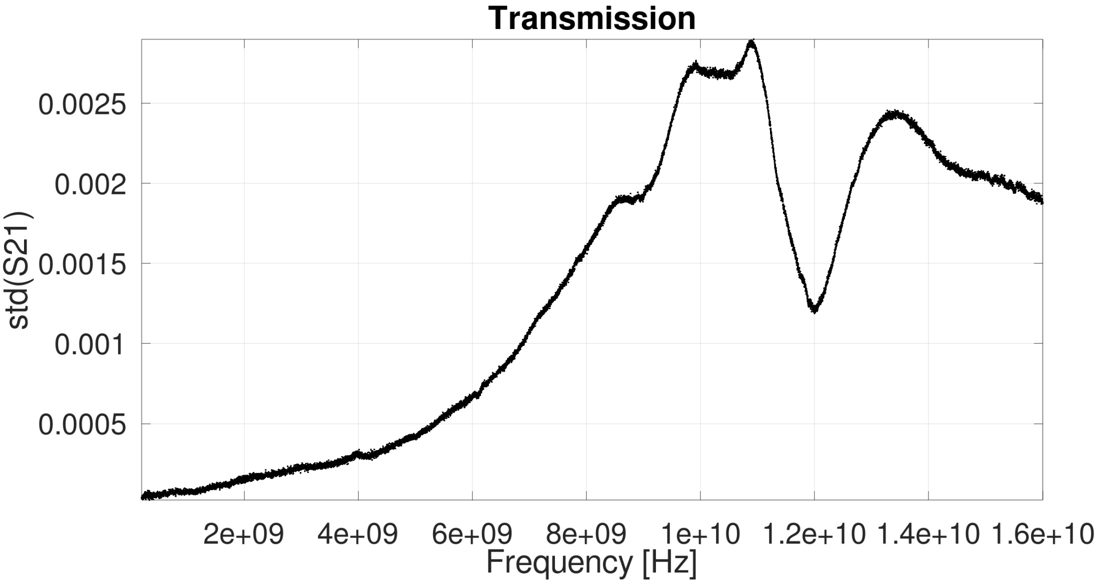

(a) S_{21} standard deviation.

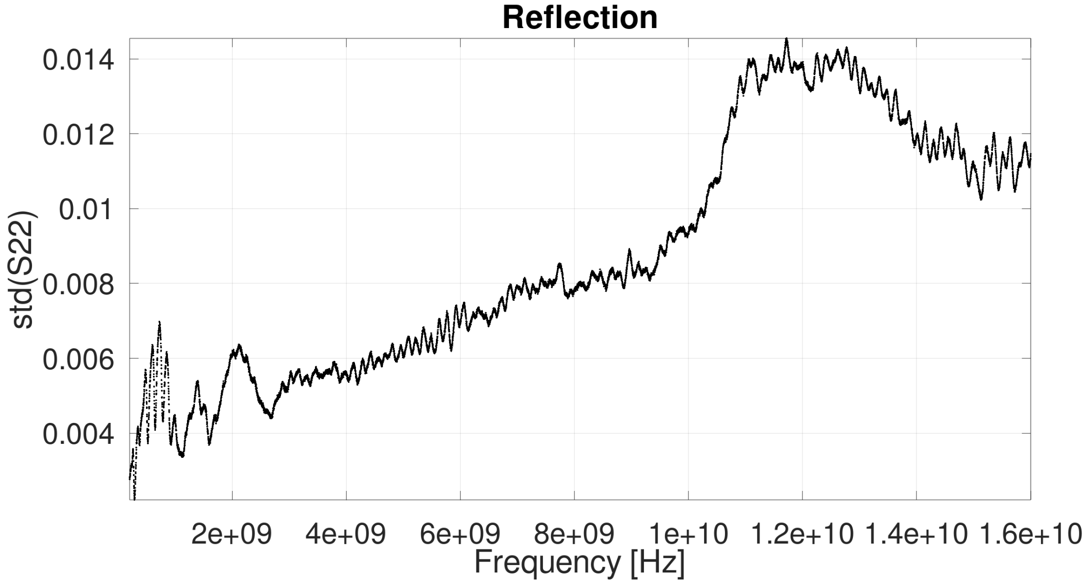

(b) S_{22} standard deviation.

Fig. 6.4 3PTF: standard deviation of S21 and S22 up to 16 GHz in the case of VNA measurements.

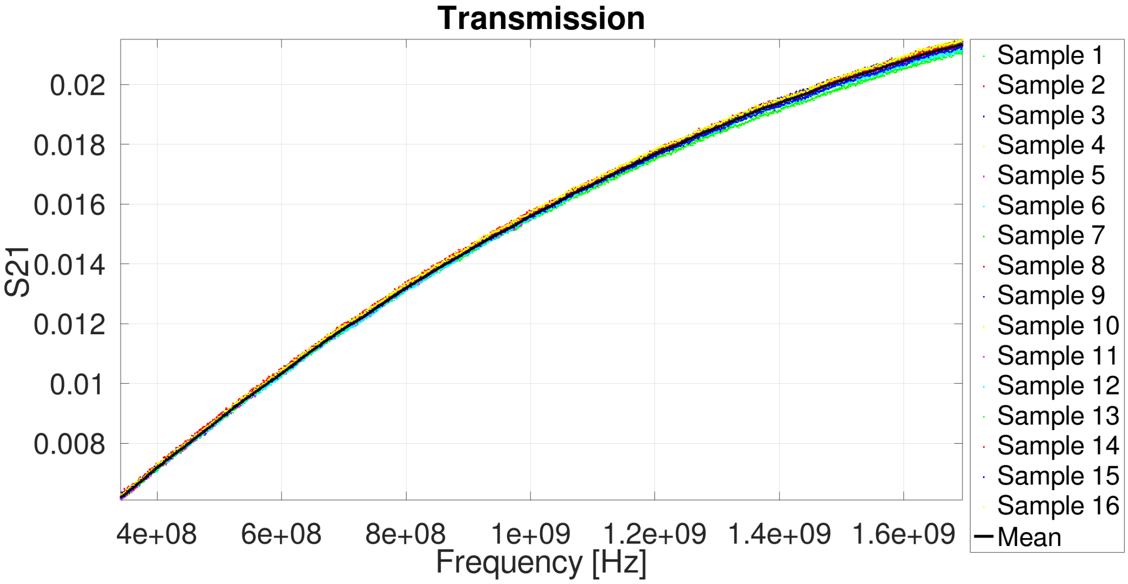

(a) S_{21} frequency response.

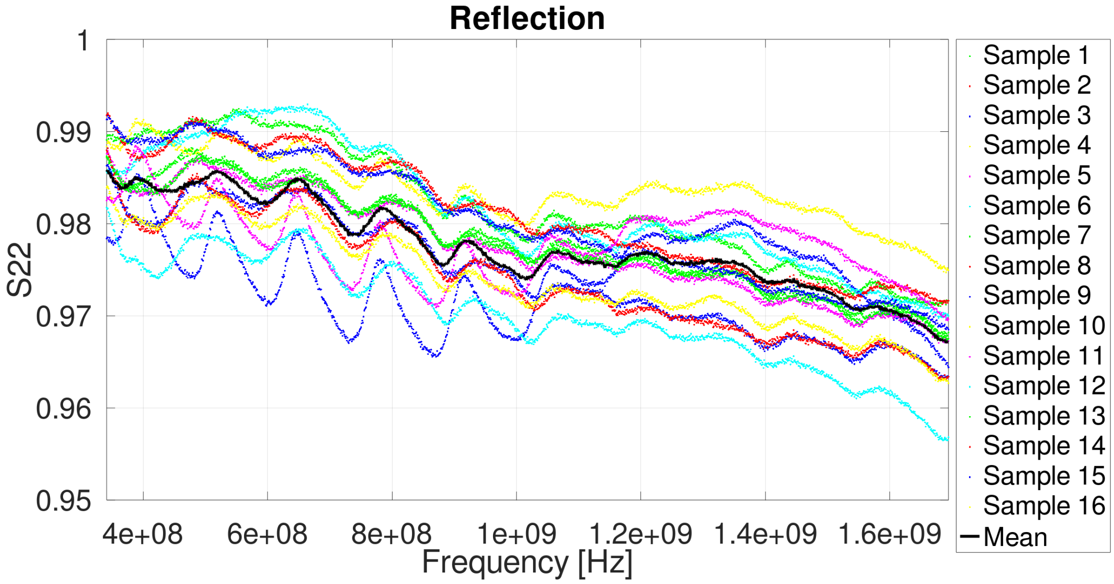

(b) S_{22} frequency response.

Fig. 6.5 3PTF VNA measured S_{21} and S_{22} in the frequency band [0.4 - 1.6] GHz.

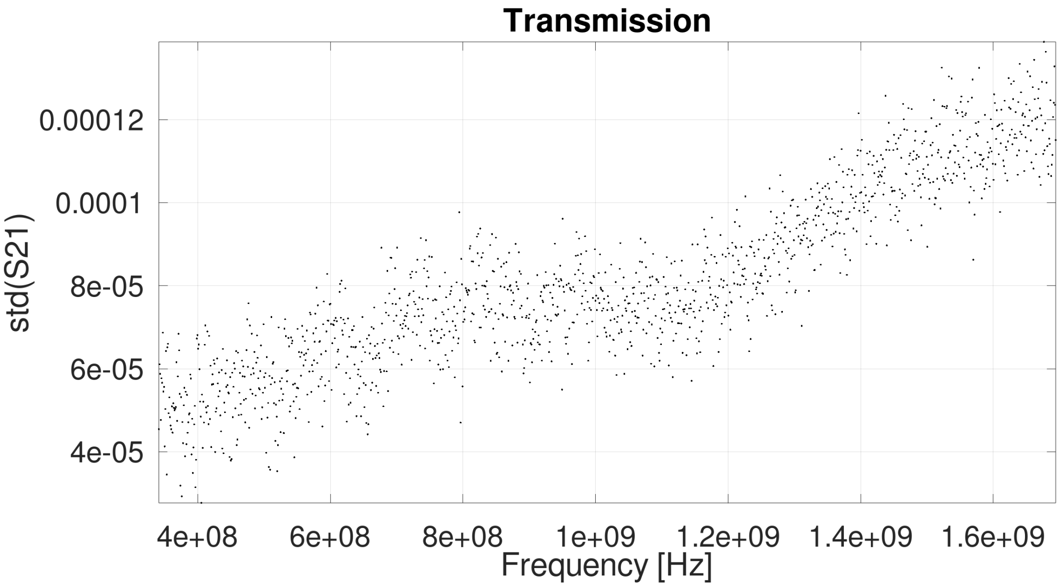

(a) S_{21} standard deviation.

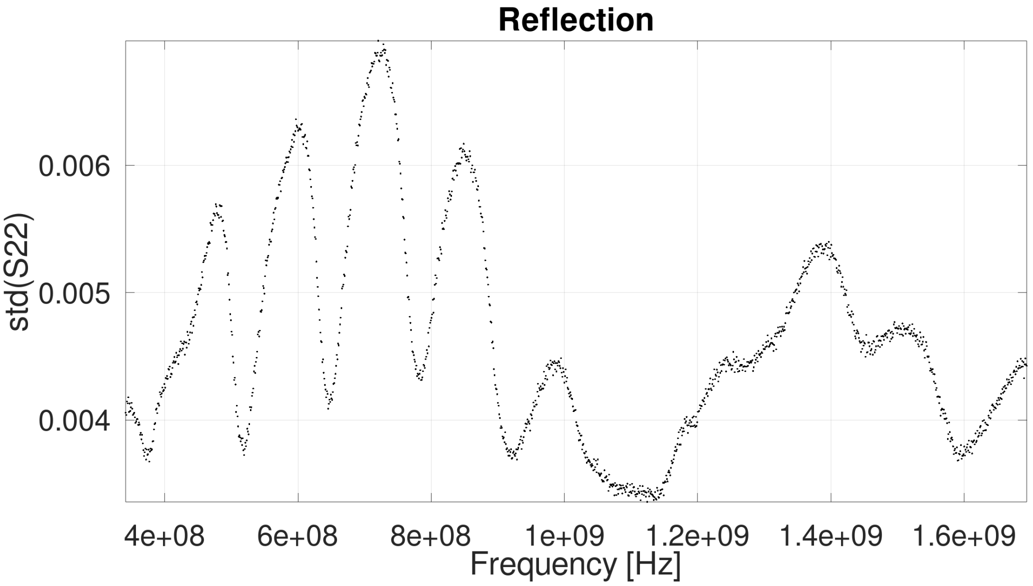

(b) S_{22} standard deviation.

Fig. 6.6 3PTF VNA standard deviation of S21 and S22 in the frequency band [0.4 - 1.6] GHz.

6.4.2 TDR/TDT measurements

Figures 6.7a and 6.7b show the S_{21} and S_{22} scattering parameters, respectively, measured with a TDR/TDT up to 16 GHz. A comparison of the frequency responses for each pickup shows that the corresponding curves are in very close agreement.

The standard deviation calculated over the population of 16 pickup prototypes is shown in Figure 6.8a for S_{21} and Figure 6.8b for S_{22}. A direct comparison of the standard deviation curves clearly indicates that the reflection measurements exhibit greater dispersion than the transmission measurements.

6.4.3 Conclusions about 3PTF measurements

The measurements performed with the 3PTF up to 16 GHz on the 16 pickup prototypes show very small dispersion around the mean value. The dispersion is even smaller in the range [0.4–1.6] GHz, which represents the practical frequency band to be considered for the fundamental characterization of the pickups. This band comprises the central frequencies of the position detectors of Elettra 2.0 (500 MHz for the global orbit feedback and 1.5 GHz for the bunch-by-bunch feedback). The low dispersion of the measured data provides the best confirmation of the excellent repeatability of the the pickup manufacturing process.

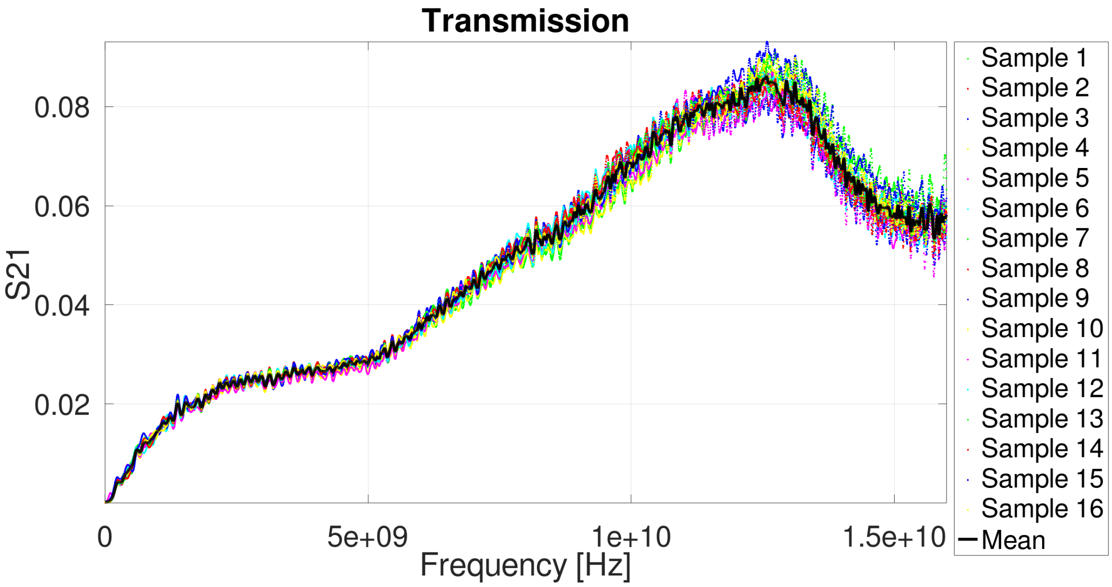

(a) S_{21} frequency response.

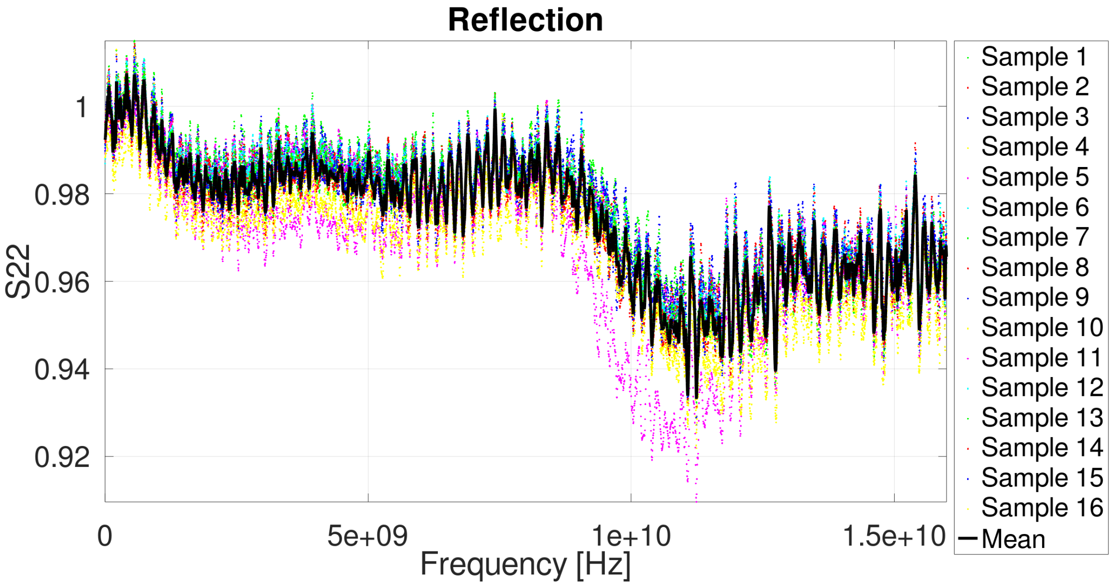

(b) S_{22} frequency response.

Fig. 6.7 3PTF tests: S_{21} and S_{22} frequency responses measured by TDR/TDT.

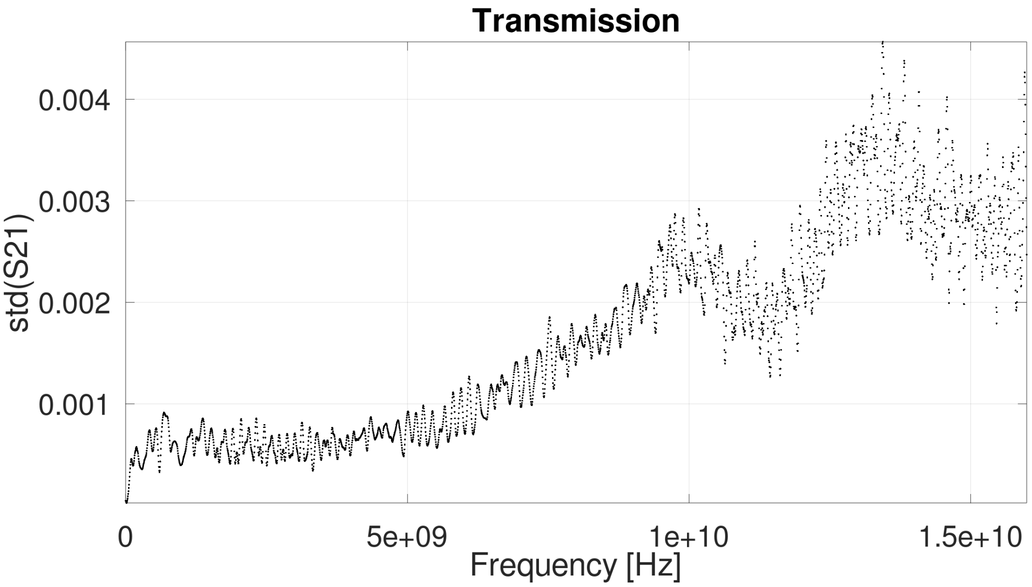

(a) S_{21} standard deviation.

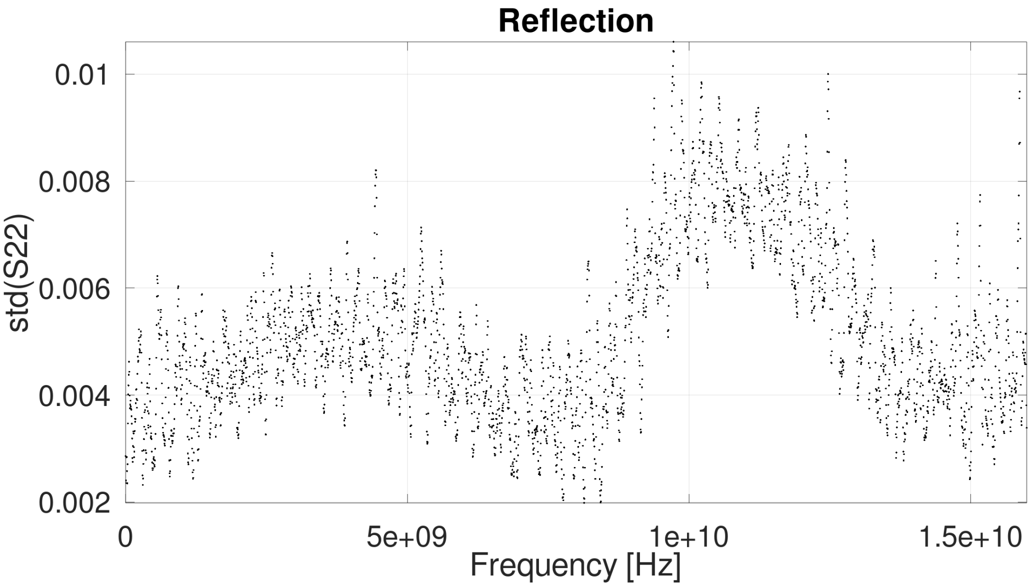

(b) S_{22} standard deviation.

Fig. 6.8 3PTF: standard deviation of S_{21} and S_{22} in the case of TDR/TDT measurements .

6.5 2PTF based electromagnetic tests

In order to get a complete electromagnetic characterization of the pickup prototypes up to 40 GHz, the nominal bandwidth of the K connector, another set of time domain (TDR/TDT) and frequency domain (VNA) measurements have been performed through a 2PTF. Thanks to its small size, cavity-like geometry, the 2PTF can operate within the 40 GHz frequency range without exciting higher-order modes. The RF connector of each pickup under test has always been connected to port 2 of the measuring device, while the RF connector of the 2PTF has always been connected to port 1.

For the purpose of obtaining a minimal statistical characterization of the RF behavior of the prototypes, the mean value and standard deviation have been calculated for each set of S_{21} and S_{22} measurements.

6.5.1 VNA measurements

Two sets of VNA measurements have been performed to check the repeatability of the measurement process, specifically with regard to the effects of the mechanical contact between the test fixture and the pickup under test. These effects have already been discovered by TDR/TDT characterization of the pickup prototypes, as reported in the previous paragraph. Figure 6.9a and Figure 6.9b show the first set of results for S_{21} and S_{22}, respectively. The transmission anomaly indicated by A in Figure 6.11a, located around 22 GHz, corresponds to the reflection peaks indicated by P in Figure 6.12b. Figure 6.10a and Figure 6.10b that represent, respectively, the standard deviation of S_{21} and S_{22}, confirm the presence of anomalies at around 22 GHz.

By adjusting the tightening torque of the ring nut that holds in place the pickup on the 2PTF housing, it has been possible to drastically reduce the measured anomalies, as shown in Figure 6.11a for transmission, and Figure 6.11b for reflection. About transmission, comparing Figure 6.9a with Figure 6.11a, the anomaly A visible in the first figure has disappeared in the second one. The residual trace of its presence in the second set of transmission measurements can instead be revealed comparing Figure 6.10a and Figure 6.12a. About reflection, only small peaks compared to the original ones visible at 22 GHz in Figure 6.9b are still present in Figure 6.11b. The confirmation of the reduction of S_{22} dispersion in the second set of measurements is also obtained comparing Figure 6.10b and Figure 6.12b.

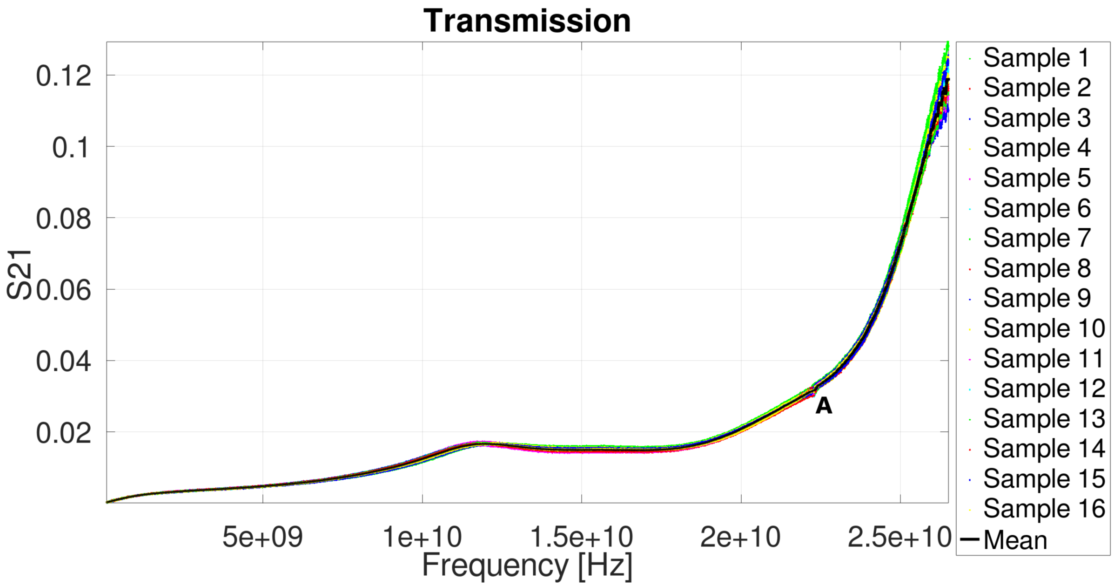

(a) S_{21} frequency response.

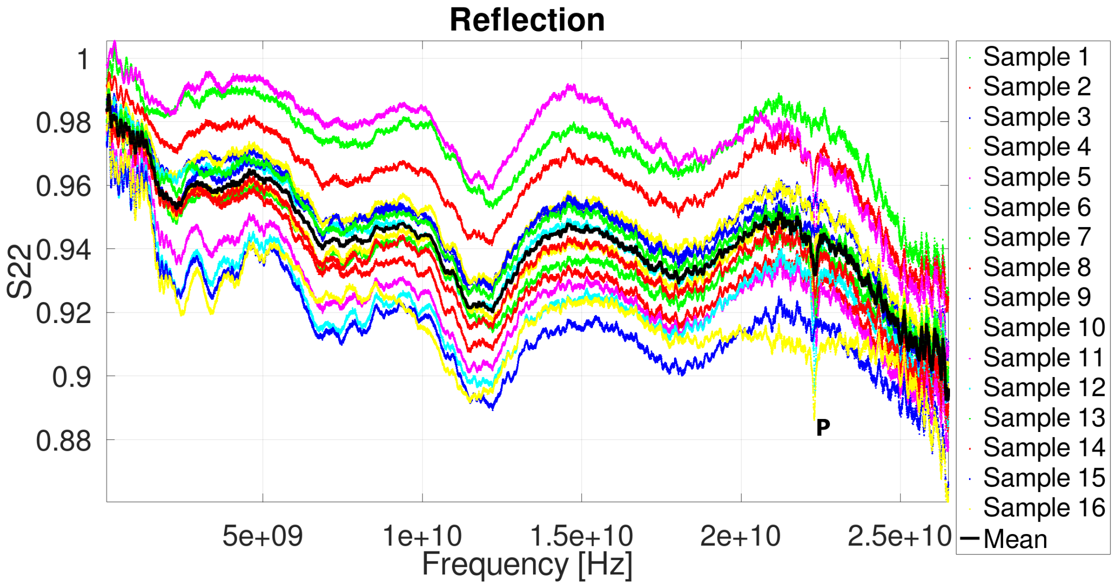

(b) S_{22} frequency response.

Fig. 6.9 2PTF VNA measured S_{21} and S_{22} up to 26.5 GHz.

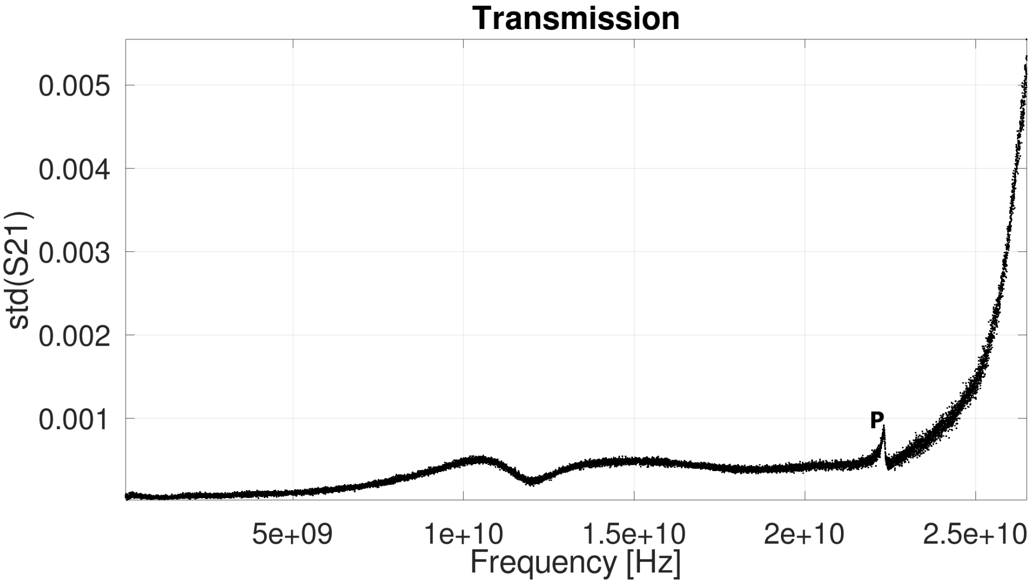

(a) S_{21} standard deviation.

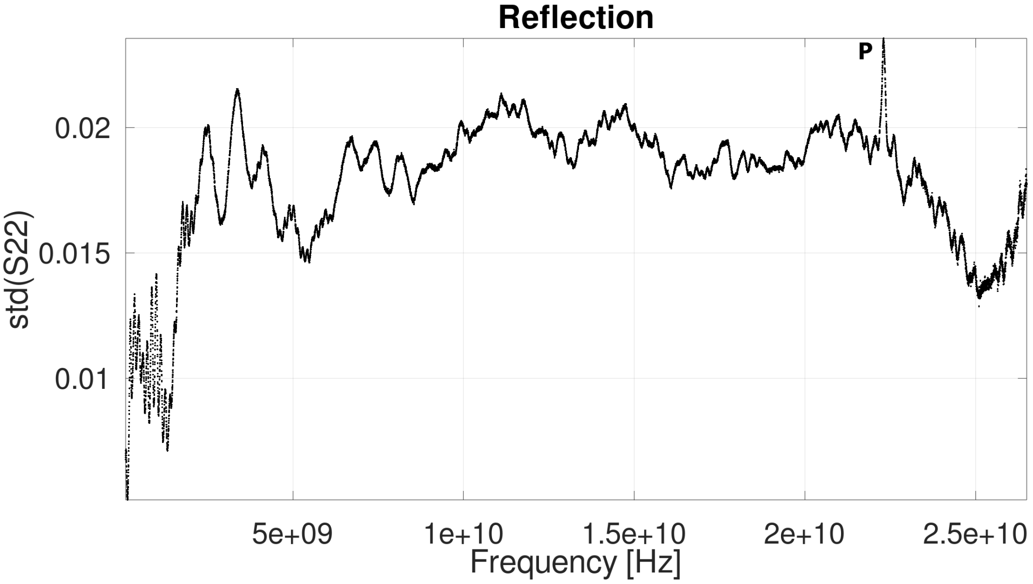

(b) S_{22} standard deviation.

Fig. 6.10 2PTF VNA standard deviation of S21 and S22 in the frequency band [0.4 - 1.6] GHz.

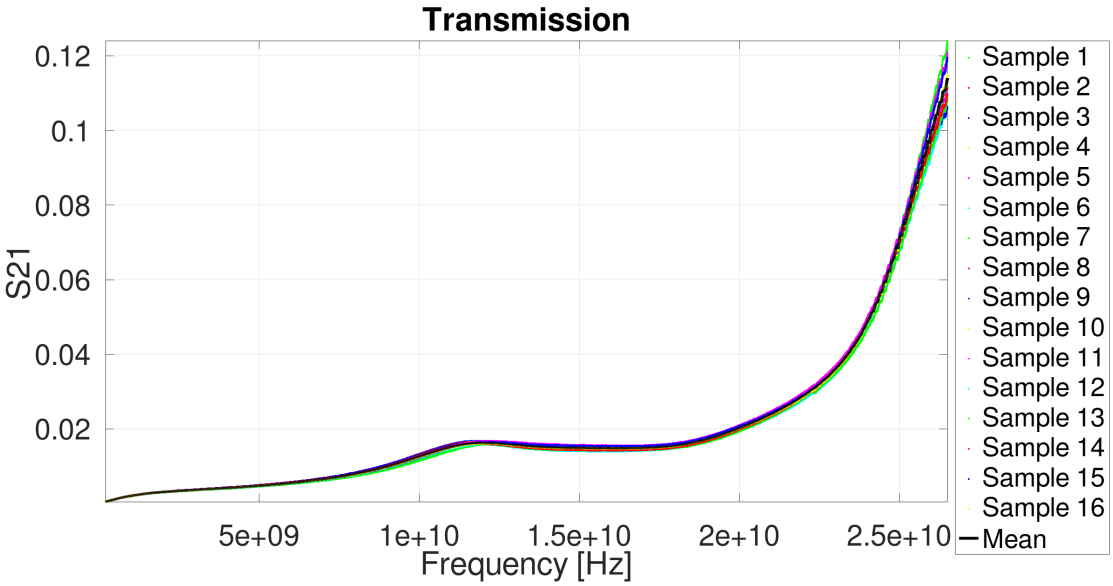

(a) S_{21} frequency response.

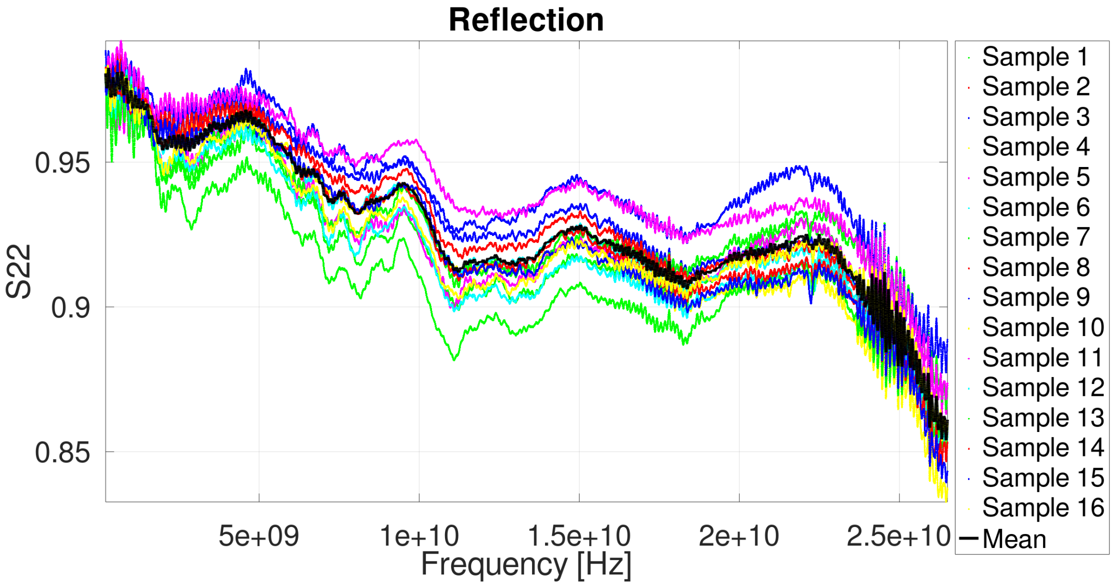

(b) S_{22} frequency response.

Fig. 6.11 2PTF VNA measured S_{21} and S_{22} up to 26.5 GHz.

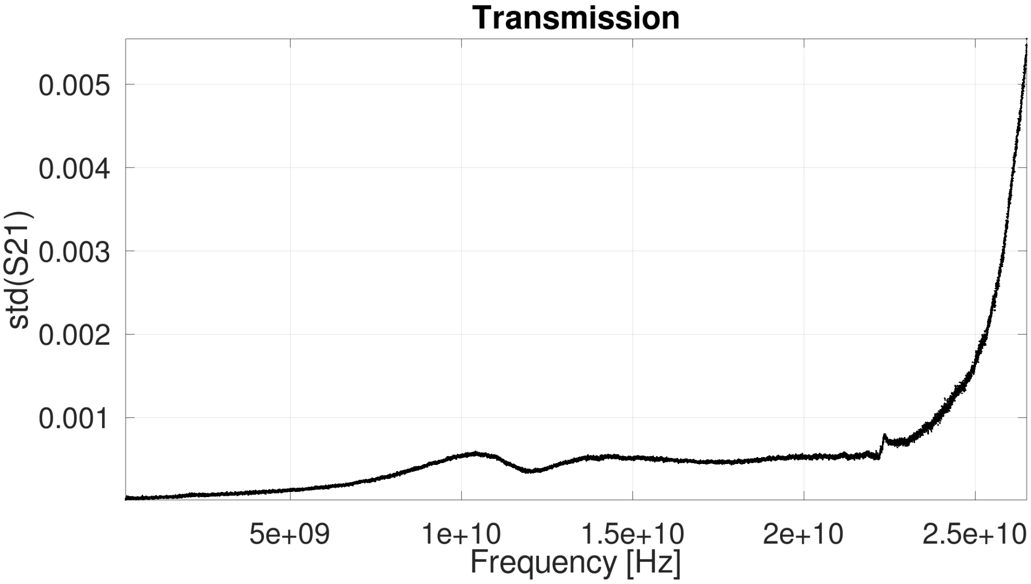

(a) S_{21} standard deviation.

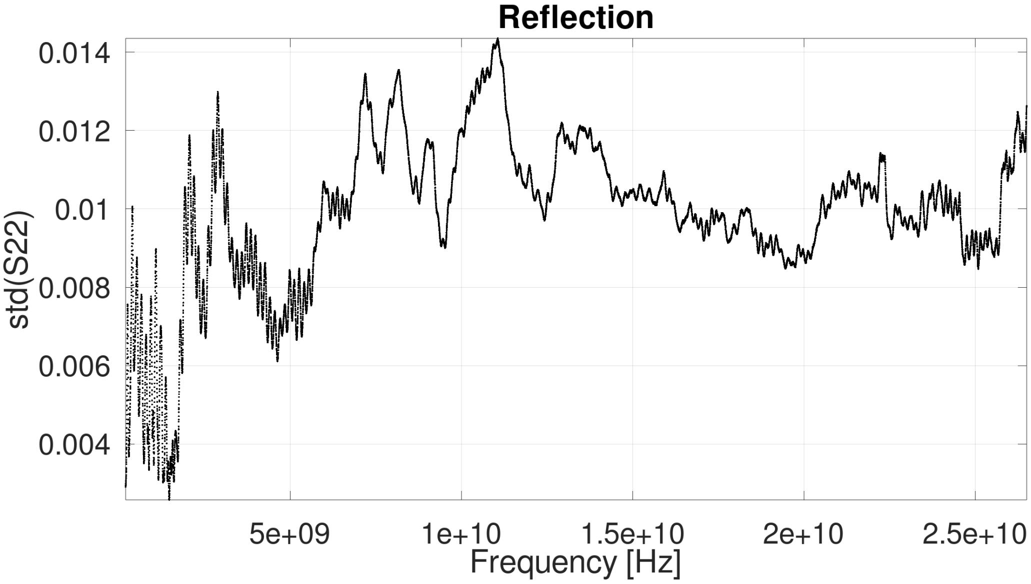

(b) S_{22} standard deviation.

Fig. 6.12 2PTF VNA standard deviation of S21 and S22 up to 26.5 GHz.

6.5.2 TDR/TDT measurements

Figure 6.13a and Figure 6.13b show, respectively, the S_{21} and S_{22} scattering parameters measured by TDR/TDT up to 40 GHz. The standard deviation calculated on the population represented by the 16 pickup prototypes is shown in Figure 6.14a for S_{21} and Figure 6.14b for S_{22}, respectively. The anomalous peak P of the S_{21} and S_{22} scattering parameters exhibited by some samples around to 28 GHz are due to the poor electric contact between the pickup under test and the 2PTF housing. After removing the pickup, cleaning the contact surfaces, and putting the pickup back in its housing, this effect has been strongly reduced. This effect clearly indicates the importance of avoiding poor mechanical contact, as this can alter the propagation of surface currents along the inner side of the 2PTF.

6.5.3 Conclusions about 2PTF measurements

Measurements performed using the 2PTF enable the prototypes to be characterized up to 40 GHz. A critical issue arises from the mechanical contact between the test fixture and the pickup under test. If the pickup is not kept in position accurately during the measurements, anomalies can appear at certain points in the frequency spectrum. This effect is similar to measurement artifacts that occur in high-frequency measurements due to RF connectors being screwed with the wrong torque. Once the pickups are correctly mounted on the 2PTF, the standard deviations of the VNA measurement show a very good repeatability of the behavior of the prototypes. TDR/TDM measurements, on the other side, show that the standard deviation of transmission increases over 30 GHz. The reason of this behavior has not been investigated yet.

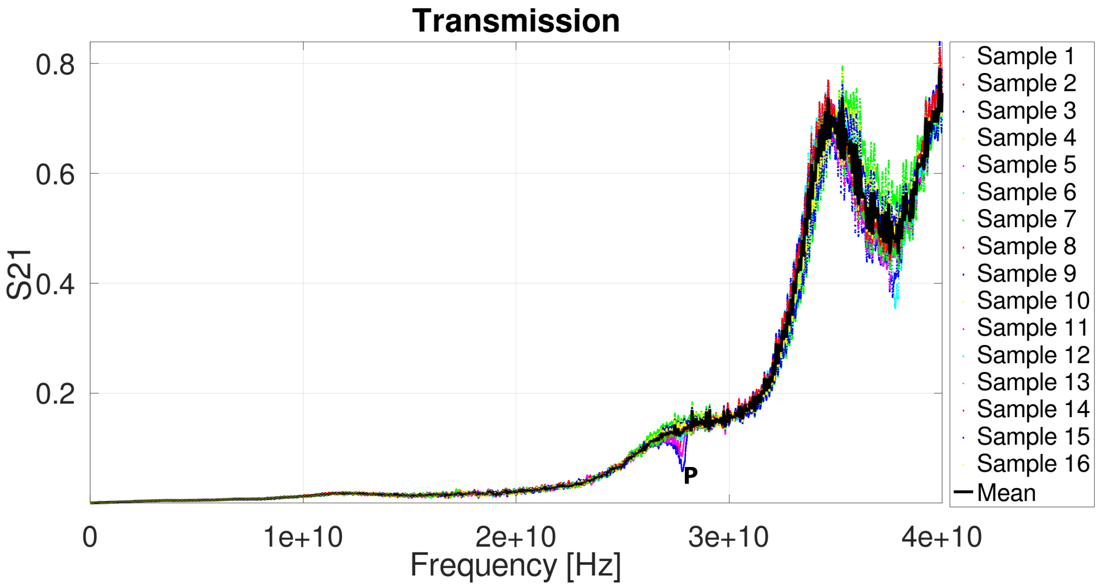

(a) S_{21} frequency response.

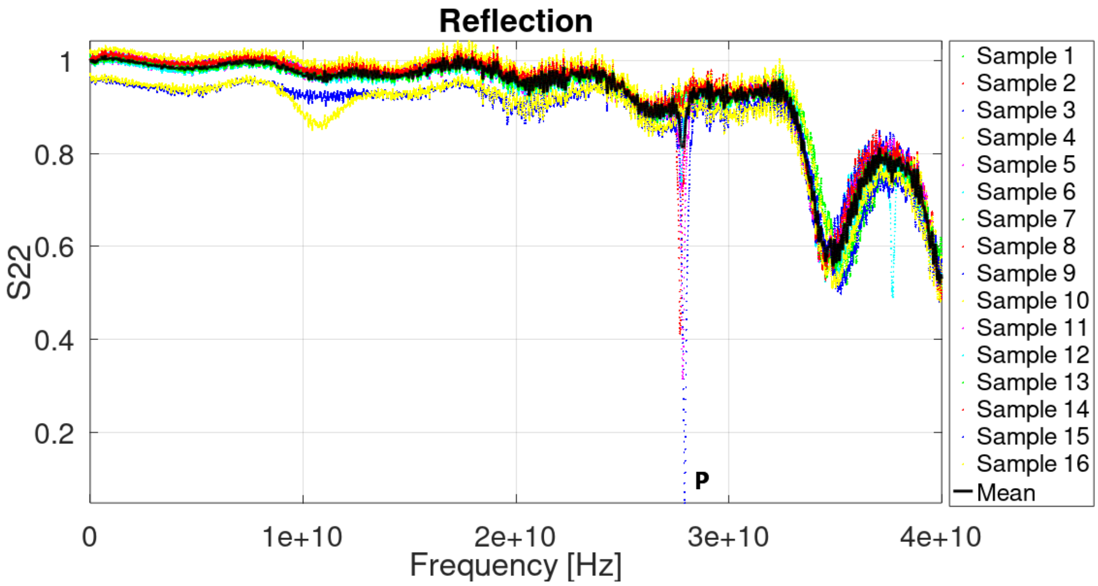

(b) S_{22} frequency response.

Fig. 6.13 2PTF TDR/TDR measured S_{21} and S_{22} frequency responses up to 40 GHz.

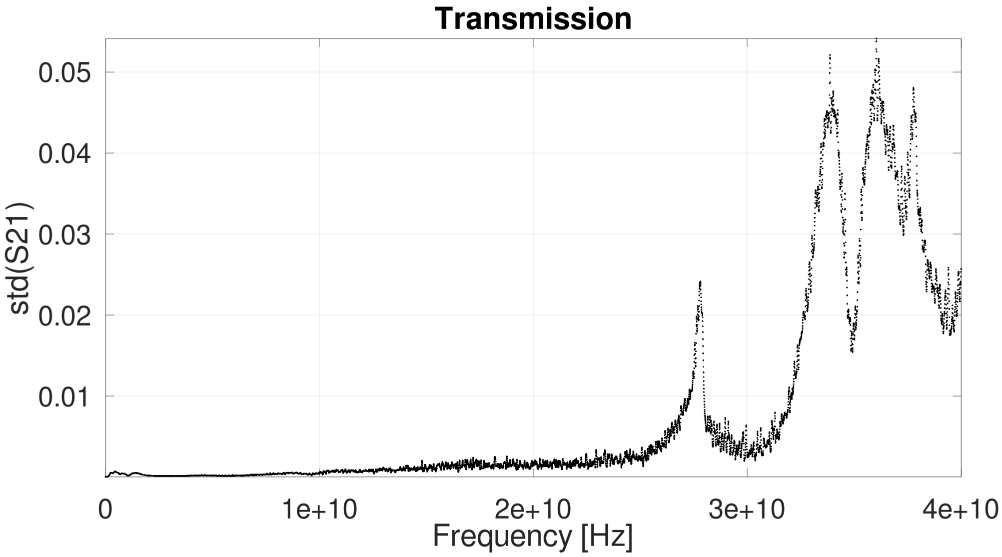

(a) S_{21} standard deviation.

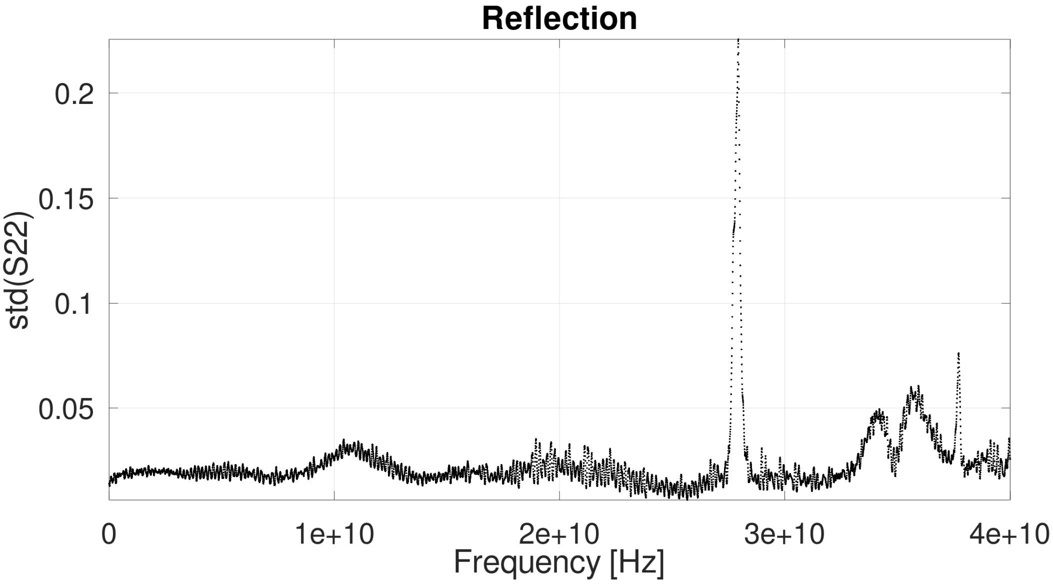

(b) S_{22} standard deviation.

Fig. 6.14 2PTF TDR/TDT standard deviation of S21 and S22 up to 40 GHz.

6.6 Comparison between measured and simulated data

The final step in the prototype validation process involved a direct comparison between simulated and measured data. Owing to the low dispersion observed in the experimental results, the mean values of the transmission and reflection scattering parameters were adopted as reference quantities for the comparison with the simulations. Numerical simulations were carried out using both the HFSS frequency-domain solver and the CST time-domain solver. The electromagnetic models employed in the simulations were derived directly from the mechanical drawings of the pickup prototypes and of the 2PTF and 3PTF fixtures; consequently, the nominal design dimensions were used in the construction of the models. To evaluate the effect of the glass, three different values of ε_R were used in the simulations. This parametric scan was perform because the exact value of the dielectric permittivity was not known.

6.6.1 3PTF data comparison

Figure 6.15 shows the frequency dependence of the measured (mean value - VNA) and simulated S_{21} and S_{22} scattering parameters as obtained using the 3PTF. The simulated S_{21} curves exhibit the same overall trend as the measured data. By increasing the relative permittivity from 4.1 to 4.6, the agreement between simulation and measurement improves. About S_{11}, the comparison between measured and simulated data is less significant because the signal is nearly completely reflected.

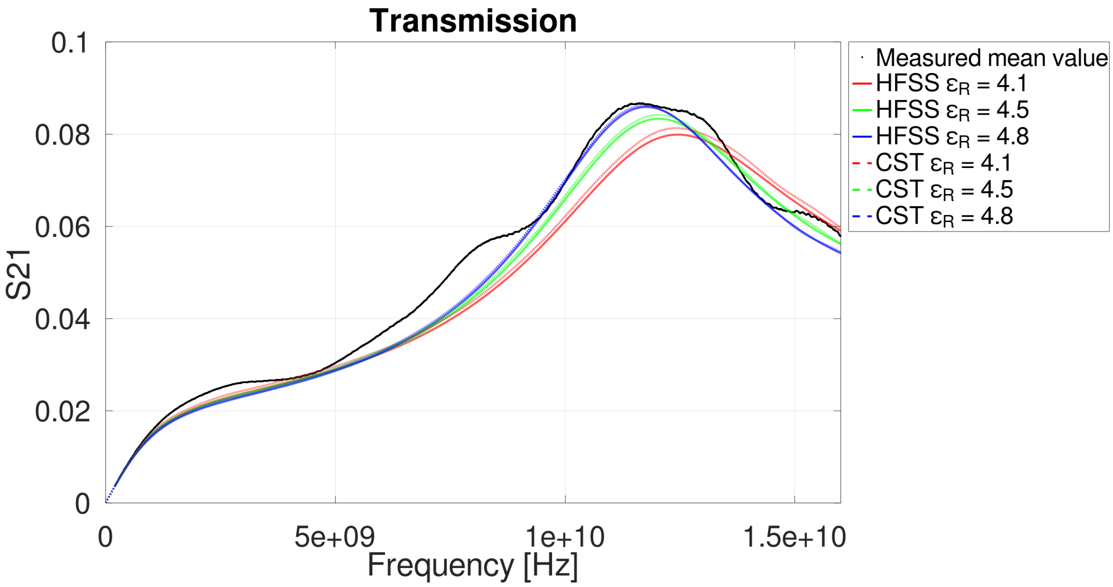

(a) S_{21} frequency response.

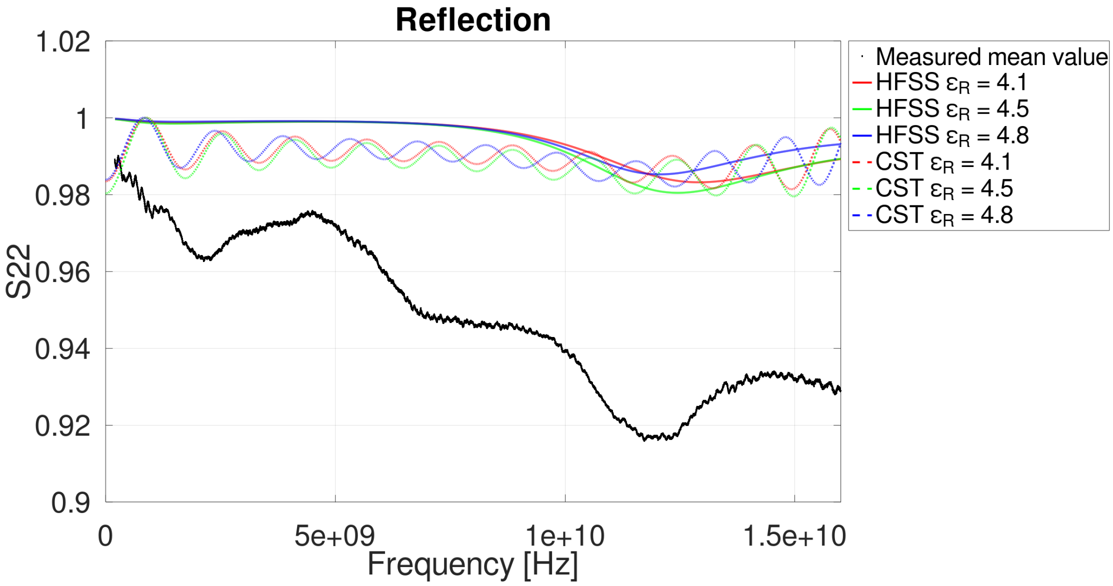

(b) S_{22} frequency response.

Fig. 6.15 3PTF VNA measured S_{21} and S_{22} frequency responses up to 16 GHz.

6.6.2 2PTF data comparison

Figure 6.16 shows the frequency dependence of the measured (mean value - TDR/TDT) and simulated S_{21} and S_{22} scattering parameters as obtained using the 2PTF. The simulated curves follow the same general behavior as the measured one, although they display a frequency shift whose magnitude decreases with increasing relative permittivity. A possible explanation lies in the frequency dependence of the dielectric permittivity.

6.6.3 Conclusions on data comparison

The comparison between measured and simulated data show that the pickup prototypes behaves very close as predicted by simulation. Consistent with previous findings obtained during the development of the in-house pickups, the discrepancies between the results of the two numerical solvers are practically negligible. A more accurate evaluation of the simulation accuracy would require knowing the exact value of the relative permittivity, but this information was not released by the manufacturer of the pickups.

6.7 Conclusions

This chapter presented the measurements carried out during the SAT. The most notable outcome is the exceptionally low dispersion observed in the scattering parameters of the prototypes measured using 2PTF and 3PTF, which clearly reflects the high quality of the manufacturing process implemented by the manufacturer. The 3PTF enabled the characterization of the pickup prototypes up to 16 GHz, whereas the 2PTF extended the measurement range to 40 GHz. Despite the exact value of ε_R is unknown, simulations performed with permittivity values consistent with glass show very good agreement with the measured scattering parameters.

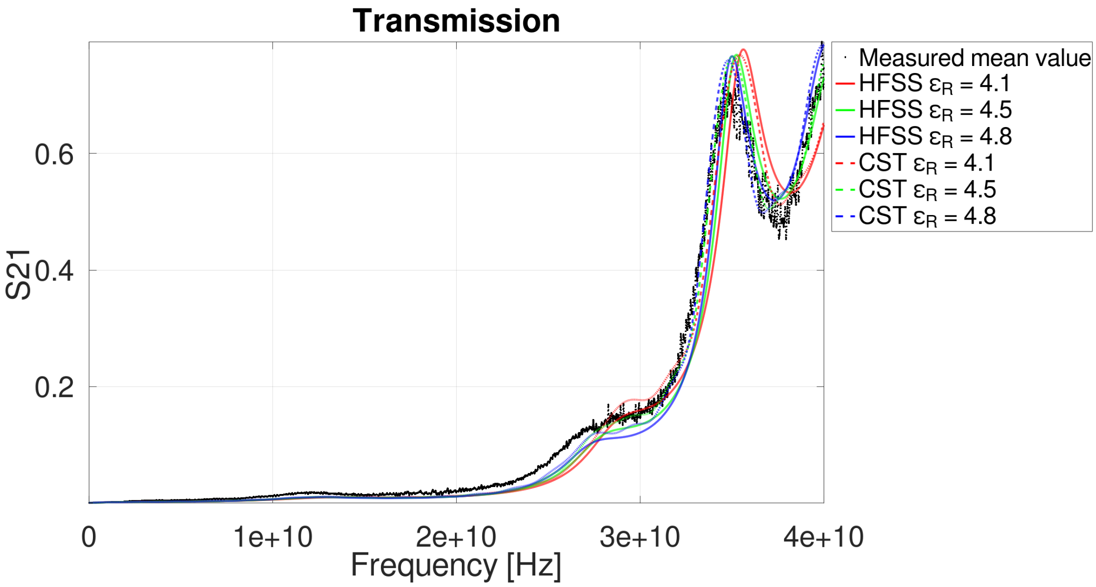

(a) S_{21} frequency response.

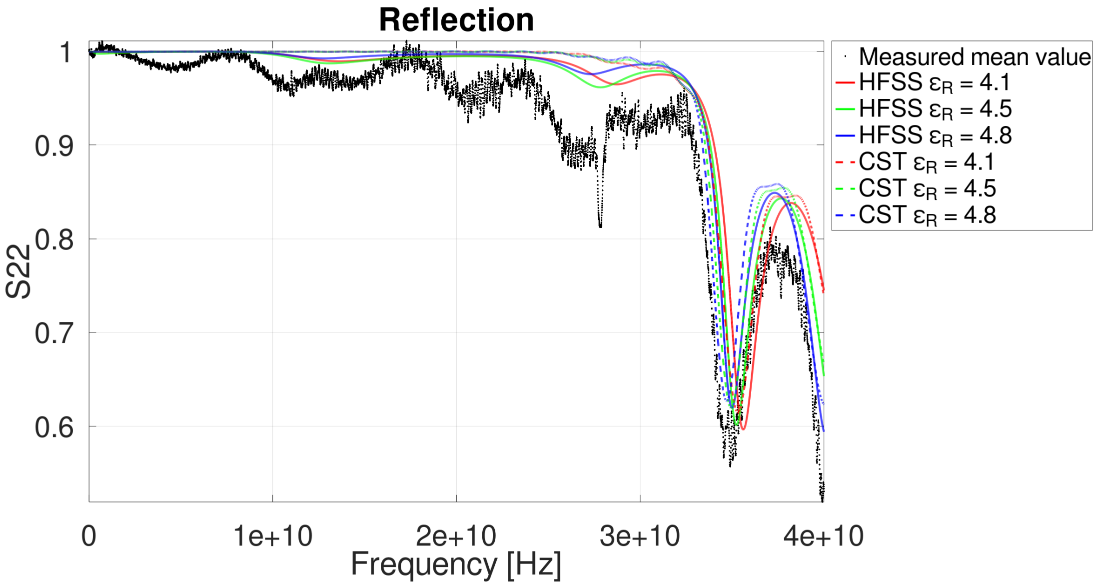

(b) S_{22} frequency response.

Fig. 6.16 2PTF TDR/TDR measured S_{21} and S_{22} frequency responses up to 40 GHz.

Conclusion

This thesis was conceived with the primary objective of contributing to the development of advanced accelerator components for Elettra 2.0, a fourth-generation synchrotron light source designed to deliver ultra-low emittance and unprecedented beam brilliance. In such a machine, the control of collective effects and the availability of reliable, high-performance beam diagnostics are fundamental requirements for achieving the targeted beam stability and operational flexibility. Within this context, the work focused on two complementary yet closely related aspects: the study and minimization of beam coupling impedance generated by components installed in the vacuum chamber, and the design of optimized button-type Beam Position Monitors (BPMs) tailored to the stringent constraints of the new storage ring.

These efforts aimed to ensure beam stability, reduce undesirable collective effects such as wakefield-induced energy loss and instabilities, and enable precise control and monitoring of the beam trajectory along the ring. Together, these aspects represent essential factors for the overall scientific success of the facility as they directly affect the quality, reproducibility, and reliability of the photon beam delivered to users.

The key objectives and results achieved throughout the thesis are summarized below.

- Design and Prototypical Realization of Beam Position Monitors (BPMs):
  - The main challenge addressed was the significantly reduced dimensions of the vacuum chambers, which imposes strong mechanical constraints on the design and manufacturing of the pick-ups. These constraints not only complicate the mechanical realization of the BPMs, but also impact procurement timelines and industrial feasibility, leading to critically long delivery times if not carefully managed.
  - Numerical analysis confirmed that shorter electron bunch lengths lead to higher wake potential, longer wakefield durations, and greater energy loss by the beam within the BPM structure. These effects become increasingly relevant in a fourth-generation light source, where short bunch operation is required.

  - It was shown that an increase in the dielectric permittivity of the sealing material (e.g., from $\varepsilon_r = 1$ to 9.9) shifts the trapped mode resonances toward lower frequencies and may lead to increased ringing of the BPM output signal, potentially degrading position measurement quality.
  - The BPM design process therefore required a careful balance between maximizing signal extraction through the four pick-ups, minimizing the parasitic electromagnetic effects, and ensuring a sufficiently robust and stable output signal under all foreseen operating conditions, including variations in electron bunch length.
  - The development of three successive generations of "Home Made Pick Up" (HMPU) prototypes enabled a progressive refinement of the design and provided a direct validation of the electromagnetic simulations through measurements performed on dedicated test benches and under real operating conditions with circulating beam.
  - The full signal acquisition chain foreseen for Elettra 2.0, including front-end electronics and data processing, was fully evaluated in the existing Elettra machine, demonstrating that the entire system functions as expected and is ready for integration into the new facility.
  - The experience accumulated with the first three HMPU generations was integrated into the fourth, which served as the reference design for the Elettra 2.0 pickups.
  - The FAT (factory acceptance tests) and SAT (site acceptance tests) tests performed on the first sixteen prototypes demonstrated the outstanding quality of these devices.

The BPM activity represents a concrete example of how electromagnetic design, mechanical constraints, and experimental validation must be addressed simultaneously in modern accelerator projects. The achieved results demonstrate that it is possible to develop compact, low-impedance diagnostic devices without compromising signal quality, even under the demanding conditions imposed by a fourth-generation storage ring.

- Evaluation of Impedance Contribution from Flanges (Vacuum Seals):
  - A detailed comparative numerical analysis was conducted on two types of vacuum sealing flanges, namely the SFL (Spigot Flange Lip) type and the SFP (Spigot Flange Planar) type, selected due to their potential to generate adverse beam interactions.

- The simulations quantitatively demonstrated that the SFP type flange exhibits a normalized longitudinal impedance approximately one hundred times lower than that of the SFL type, highlighting a substantial difference in electromagnetic behavior between the two solutions.
- This result led to the conclusion that SFL flanges are unsuitable for Elettra 2.0, given their high wake loss factor. It was estimated that, when considering a total of 250 flanges installed along the ring, the nominal SFL type would dissipate 3865 W, compared to 1050 W for the nominal SFP configuration.
- The study further highlighted the critical importance of adhering to strict geometric tolerance limits for key parameters such as the flange gap and the gasket radius, as even small deviations were shown to significantly influence impedance and power loss.
- Through the development of a custom rhomboidal radiofrequency (RF) gasket, the losses associated with both flange types were practically reduced to zero. This design electrically connects the two opposite sides of the flange, almost completely closing the gap and effectively decoupling the vacuum seal from the RF shielding. The small size of the residual apertures renders the coupling between the cavity formed by the flange and the beam negligible.

The flange study clearly demonstrates how components that are primarily mechanical in nature can have a strong impact on beam dynamics if their electromagnetic behavior is not carefully addressed. The solutions developed within this thesis not only satisfy the impedance requirements of Elettra 2.0, but also provide robust and scalable design guidelines applicable to other accelerator facilities.

From a methodological standpoint, the work performed during the thesis made extensive use of three-dimensional numerical simulations with CST Particle Studio to analyze the electromagnetic field, wake potentials, and coupling impedances. These simulations proved to be an essential design tool, allowing quantitative comparisons between different solutions and enabling informed engineering decisions prior to prototyping and experimental validation. The close agreement observed between simulation results and experimental measurements further confirms the reliability of the adopted approach.

In summary, this thesis provides both design tools and concrete, experimentally validated solutions to address the electromagnetic challenges associated with new generations of particle accelerators. The detailed studies on BPMs and vacuum flanges, combined with the systematic application of advanced simulation techniques, contribute significantly to optimizing the performance, stability, and reliability of essential components in complex machines like Elettra 2.0. More broadly, the results of this work underline the importance of an integrated design philosophy, in which electromagnetic, mechanical, and operational aspects are considered together to successfully meet the demanding requirements of fourth-generation synchrotron light sources.

List of publications

- S. Cleva, I. Cudin, E. Karantzoulis, L. Rumiz, M. Comisso, and A. Passarelli, "Beam coupling impedance contribution of flange aperture gaps: A numerical study for Elettra 2.0," J. Phys.: Conf. Ser., Vol. 2687, No. 6 (2024), Article ID 062015, in Int. Particle Accel. Conf. (IPAC), Venice, Italy, pp.1 - 4, 7-12 May 2023. https://hdl.handle.net/11368/3071259
- E. Karantzoulis, S. Di Mitri, F. Barbo, W. Barletta, S. Bassanese, R. Bracco, G. Brajnik, A. Buonanno, D. Caiazza, A. Carniel, D. Castronovo, M. Cautero, S. Cleva, M. Comisso, I. Cudin, S. Dastan, R. De Monte, B. Diviacco, A. Fabris, R. Fabris, G. Gaio, S. Grulja, L. Gregoratti, A. Gubertini, S. Krecic, S. Lizzit, G. Loda, M. Lonza, K. Manukyan, B. Mazzucco, M. Milani, D. Millo, M. Modica, L. Novinec, G. Pangon, C. Pasotti, A. Passarelli, L. Rumiz, S. Sbarra, G. Scrimali, N. Shafqat, G. Simonetti, M. Svandrlik, F. Tripaldi, M. Veronese, R. Visintini, E. Yousefi, and M. Zaccaria, "Design strategies and technology of Elettra 2.0 for a versatile offer to the user community," Nucl. Instrum. Methods Phys. Res., Sect. A: Acceler., Spectrom., Detectors, Assoc. Equip., Vol. 1060, Article ID 169007, 35 pp., Mar. 2024. https://hdl.handle.net/11368/3067618
- S. Cleva, S. Bassanese, M. Comisso, M. El Ajjouri, R. Sergo, C. Morello, and A. Passarelli, "Button-type beam position monitor development for fourth-generation synchrotron light sources: Numerical modeling and test bench measurements," Sensors, Vol. 24, No. 9, Article ID 2726, 15 pp., May 2024. https://hdl.handle.net/11368/3075579

References

[1] (2022). Ieee standard for precision coaxial connectors at rf, microwave, and millimeter-wave frequencies–part 1: General requirements, definitions, and detailed specifications. *IEEE Std 287.1-2021*, pages 1–136.

[2] (2024). DEPARTMENT OF DEFENSE INTERFACE STANDARD. MIL-STD-348B. Issued August 2024. Published by the Defense Logistics Agency, ATTN: VAI, P.O. Box 3990, Columbus, Ohio 43218-3990.

[3] Ajjouri, M. E., Alves, F., Gamelin, A., and Hubert, N. (2021). Preliminary Studies for the SOLEIL Upgrade BPM. In *Proc. IBIC'21*, number 10 in International Beam Instrumentation Conference, pages 128–132. JACoW Publishing, Geneva, Switzerland. https://doi.org/10.18429/JACoW-IBIC2021-MOPP31.

[4] Ajjouri, M. E., Alves, F., Gamelin, A., and Hubert, N. (2022). Design of the Beam Position Monitor for SOLEIL II. In *Proc. IBIC'22*, number 11 in International Beam Instrumentation Conference, pages 233–237. JACoW Publishing, Geneva, Switzerland.

[5] Ansys, Inc. (2025). *Ansys HFSS, Release 2025 R2*. Ansys, Inc., Canonsburg, PA, USA. Software per la simulazione elettromagnetica a onde piene.

[6] Barry, W. C. (1992). Broad-band characteristics of circular button pickups. *AIP Conference Proceedings*, 281(1):175–184.

[7] Bilanishvili, S. and Zobov, M. (2024). Capacitive BPM electromagnetic design optimisation. *J. Phys. Conf. Ser.*, 2687:072004.

[8] Brajnik, G., Bassanese, S., Cautero, G., Cleva, S., and De Monte, R. (2018). Integration of a Pilot-Tone Based BPM System Within the Global Orbit Feedback Environment of Elettra. In *13th International Beam Instrumentation Conference (IBIC 2018)*, pages 190–195, Shanghai, China. JACoW.

[9] Brajnik, G., Gaio, G., De Monte, R., Bassanese, S., and Cleva, S. (2023). Elettra 2.0 eBPM: Complete System Overview. *JACoW*, IPAC2023:THPL077.

[10] Buffat, X. (2024). Collective effects.

[11] Campelo, J. E. (2015). Longitudinal Impedance Characterization of the CERN SPS Vacuum Flanges. In *6th International Particle Accelerator Conference*, page MOPJE036.

[12] Cleva, S. (2024). Home Made Button Type BPMs: demo antennas or real diagnostics tools? [online] https://indico.cells.es/event/1542/contributions/2942/.

[13] Cleva, S., Bassanese, S., Brajnik, G., Cudin, I., De Monte, R., Loda, G., Pangon, G., Comisso, M., Passarelli, A., Maletta, C., and et al. (2023). Button type beam position monitor design for the elettra 2.0 storage ring. In *Int. Part. Accel. Conf. IPAC*, pages 4621–4624.

[14] CST (2025). CST studio suite. https://www.3ds.com/.

[15] CST Computer Simulation Technology (2022). Studio suite. Dassault Systèmes Simulia.

[16] D'Auria, G. et al. (2008). Installation and Commissioning of the 100 MeV Preinjector Linac of the New Elettra Injector. *Conf. Proc. C*, 0806233:WEPC071.

[17] Di Mitri, S. et al. (2023). Transverse deflecting cavities for short X-ray pulses at Elettra 2.0. *JACoW*, IPAC2023:MOPA163.

[18] Duarte, H., Sanfelici, L., and Marques, S. (2013). Design and impedance optimization of the SIRIUS BPM button. In *Int. Beam Instrum. Conf. IBIC*, pages 365–368.

[19] Elettra Sincrotrone Trieste (2025). Tomolab. https://www.elettra.eu/lightsources/labs-and-services/tomolab/tomolab.html. Accessed: 2025-02-12.

[20] Forck, P. (2020). Beam instrumentation and diagnostics.

[21] Goldberg, D. A. and Lambertson, G. R. (1992). Dynamic devices. a primer on pickups and kickers. *AIP Conference Proceedings*, 249(1):537–600.

[22] He, J. et al. (2022). Design and fabrication of button-style beam position monitors for the HEPS synchrotron light facility. *Nucl. Sci. Tech.*, 33(11):141.

[23] He, J., Sui, Y., Li, Y., Ma, H., Du, Y., Wang, X., Yue, J., and Cao, J. (2023). Beam position monitor characterization for the high energy photon source synchrotron. *Symmetry*, 15(3).

[24] International Electrotechnical Commission (2006). IEC 61169-16: Radio-frequency connectors - Part 16: Sectional specification - RF coaxial connectors with inner diameter of outer conductor 7 mm (0,276 in) with screw coupling - Characteristics impedance 50 ohms (75 ohms) (type N). International Electrotechnical Commission. IEC 61169-16:2006.

[25] Kaltenbacher, T. and Vollinger, C. (2017). Characterization of Shielding for the CERN-SPS Vacuum Flanges with Respect to Beam Coupling Impedance. In *8th International Particle Accelerator Conference*.

[26] Karantzoulis, E., Di Mitri, S., Barbo, F., Barletta, W., Bassanese, S., Bracco, R., Brajnik, G., Buonanno, A., Caiazza, D., Carniel, A., Castronovo, D., Cautero, M., Cleva, S., Comisso, M., Cudin, I., Dastan, S., De Monte, R., Diviacco, B., Fabris, A., Fabris, R., Gaio, G., Grulja, S., Gregoratti, L., Gubertini, A., Krecic, S., Lizzit, S., Loda, G., Lonza, M., Manukyan, K., Mazzucco, B., Milani, M., Millo, D., Modica, M., Novinec, L., Pangon, G., Pasotti, C., Passarelli, A., Rumiz, L., Sbarra, S., Scrimali, G., Shafqat, N., Simonetti, G., Svandrlik, M., Tripaldi, F., Veronese, M., Visintini, R., Yousefi, E., and Zaccaria, M. (2024). Design strategies and technology of elettra 2.0 for a versatile offer to the user community. *Nuclear Instruments and Methods in Physics Research Section A: Accelerators, Spectrometers, Detectors and Associated Equipment*, 1060:169007.

[27] Lipka, D. and Vilcins, S. (2014). BPMs From Design to Real Measurement. In *Proc. 5th International Particle Accelerator Conference (IPAC'14), Dresden, Germany, June 15-20, 2014*, number 5 in International Particle Accelerator Conference, pages 2774–2778, Geneva, Switzerland. JACoW. https://doi.org/10.18429/JACoW-IPAC2014-THXA01.

[28] Lorrain, P. and Corson, D. R. (1970). *Electromagnetic Fields and Waves*. W. H. Freeman, San Francisco, 2 edition.

[29] Marcellini, F., Fortunati, R., and Keil, B. (2024). The sls 2.0 button bpm. In *Button BPMs for Synchrotron Light Sources*. Paul Scherrer Institut. Contribution ID: 16.

[30] Marcellini, F., Serio, M., Stella, A., and Zobov, M. (1998). DAΦNE broad-band button electrodes. *Nucl. Instrum. Methods Phys. Res. Sect. A Acceler. Spectrom. Detect. Assoc. Equip.*, 402:27–35.

[31] Meirose, B., Abelin, V., Bertilsson, F., Bolling, B. E., Brandin, M., Holz, M., Høier, R., Johansson, A., Kalbfleisch, S., Lilja, P., Lundquist, J. S., Molloy, S., Persson, F., Petersson, J. E., Serodio, H., Svärd, R., and Winchester, D. (2020). Real-time accelerator diagnostic tools for the max iv storage rings. *Instruments*, 4(3).

[32] Morgan, A. (2019). Technological Review of Beam Position Button Design and Manufacture. In *Proc. IBIC'19*, number 8 in International Beam Instrumentation Conferenc, pages 448–452. JACoW Publishing, Geneva, Switzerland. https://doi.org/10.18429/JACoW-IBIC2019-WEAO01.

[33] Nadji, A., Nadolski, L. S., and and (2023). Upgrade project of the soleil accelerator complex. *Synchrotron Radiation News*, 36(1):10–15.

[34] Niccoli, F., Giovinco, V., Garion, C., Maletta, C., and Chiggiato, P. (2022). Niti shape memory alloy pipe couplers for ultra-high vacuum systems: development and implementation. *Smart Materials and Structures*, 31(6):065014.

[35] Palumbo, L., Vaccaro, V. G., and Zobov, M. (2003). Wake fields and impedance.

[36] Passarelli, A. (2019). *Characterization of impedance and wakefields of accelerator devices in the short bunch limit and beam dynamics effects for the CLIC Damping Rings*. PhD thesis, Darmstadt, Tech. U.

[37] Pino, P. (2007). Intermateability of sma, 3.5 mm and 2.92 mm connectors. *Microwave Journal*, 50:18–28.

[38] Robinson, A. L. (2015). History of synchrotron radiation. *Synchrotron Radiation News*, 28(4):4–9.

[39] Scheinker, A. (2021). Adaptive machine learning for robust diagnostics and control of time-varying particle accelerator components and beams. *Information*, 12(4).

[40] Schlachter, A. S. and Wuilleumier, F. J. (1993). Third-generation synchrotron light sources. Lawrence Berkeley Lab., CA (United States).

[41] Shafer, R. E. (1990). Beam position monitoring. *AIP Conference Proceedings*, 212(1):26–58.

[42] Shafiee, M., Feghhi, S., and Rahighi, J. (2017). Numerical analysis of the beam position monitor pickup for the iranian light source facility. *Nuclear Instruments and Methods in Physics Research Section A: Accelerators, Spectrometers, Detectors and Associated Equipment*, 847:162–170.

[43] Smith, S. R. (1997). Beam position monitor engineering. *AIP Conference Proceedings*, 390(1):50–65.

[44] Stillwell, B. K., Fuerst, J. D., Liu, J., Waldschmidt, G. J., and Wu, G. (2012). Evaluation of VATSEAL Technology to Seal Waveguide Serving High-field Superconducting RF Cavities. In *Proc. IPAC'12*, pages 2298–2299. JACoW Publishing, Geneva, Switzerland.

[45] Svandrlik, M. et al. (2000). The super-3HC project: An idle superconducting harmonic cavity for bunch length manipulation. In *7th European Particle Accelerator Conference (EPAC 2000)*, pages 2052–2054.

[46] Vaccaro, V. G. (1966). Longitudinal instability of a coasting beam above transition, due to the action of lumped discontinuities. Technical report, CERN, Geneva.

[47] Vilcins, S., Bandke, D., and Holz, M. (2018). A New Sealing Technology for High Precision Wide Open UHV Vacuum Flange and Waveguide Connections With Metal Gaskets. In *10th Mechanical Engineering Design of Synchrotron Radiation Equipment and Instrumentation*, page TUPH37.

[48] Wendt, M. (2020). Bpm systems: A brief introduction to beam position monitoring.

[49] Wiedemann, H. (2015). *Particle accelerator physics; 4th ed.* Springer, Berlin.

[50] Willmott, P., Böge, M., Calzolaio, C., Dehler, M., Ganter, R., Marcellini, F., Marinkovic, G., Streun, A., and altri (2021). Sls 2.0 storage ring: Technical design report. Technical Report PSI Bericht 21-10, Paul Scherrer Institut, Villigen, Switzerland.

[51] Winick, H. (1997). Fourth generation light sources. *Conf. Proc. C*, 970512:37–41.